Optimising Terahertz Time-Domain Spectroscopy for III–V Semiconductors

Ford Matthew Wagner

New College

University of Oxford

A thesis submitted for the degree of

Doctor of Philosophy

Trinity 2025

Acknowledgements

This thesis – and my whole academic journey – would not have been possible without the support and encouragement of the people I met along the way.

First, I would like to thank my supervisor, Prof. Michael Johnston, for his endless support. I am incredibly grateful that you always make time to help me understand my research questions and appreciate your patience and understanding of any circumstances beyond the lab. Thank you for sharing your enthusiasm for science and discovery with me. I would also like to thank Prof. Laura Herz for insightful discussions and for helping to foster the friendly, welcoming lab environment that I have been so lucky to be a part of.

Thank you to everyone in the Johnston and Herz research groups for sharing in this experience with me through all the highs and lows. In particular, I would like to thank Vincent Lim, Joshua Lilly, Jiaxing Du, and Karim Elmestekawy, along with my fellow 2021 DPhils – Jae Eun Lee, Snigdha Lal, and Siyu Yan. I am so grateful to have gone through my DPhil journey with you all, and for the board game nights, badminton sessions, and delicious dinners. I am also grateful to all the postdocs who have helped me – Chelsea Xia, Kun Peng, Thomas Siday, Gurpreet Kaur, Marcello Righetto, Jasmin Bürger, and Junn Keat – for your mentorship, postdoc wisdom, and invaluable help bringing my projects to completion. Everyone in the lab played a big role in making my time in Oxford extremely fun and memorable, and I hope that we can all stay in touch.

Thank you to all my collaborators who I have had the pleasure of working with from the Australian National University, the University of Cambridge, the Lithuanian Center for Physical Sciences and Technology, Johannes Gutenberg University, and the Fraunhofer Institute for Telecommunications. Importantly, I would like to thank the University of Canterbury and Universities New Zealand for funding my studies through the generous Lord Rutherford Memorial Research Fellowship and Edward and Isabel Kidson Scholarship – these awards have truly changed my life.

To all my friends – both those I met in Oxford and those who have always been with me – thank you for everything. In particular, thanks to the Bay Boys, Daniel and Harry, for the fun catch-ups despite any time zone difficulties; to the THS boys – Daniel, Matt, David, and Logan – for being true lifelong friends; and to everyone from UC – Rebecca, Rick, Cory, Lauren, Sherry, Felix, Wilson, Phoebe, Logan, and Nick – for your constant support. Thank you to my good friends from New College – Ben, Alison, Anna,

Charlie, and Mikhail – for being such a friendly and welcoming group and for helping me through my homesickness so that I could embrace life in Oxford. Special thanks to Petra for your constant love, support, and care – this journey would not be possible without you.

Last, but certainly not least, I would like to thank my family – Mum, Dad, Camille, Yvette, Felicity and Jak – for being my biggest supporters and encouraging me to pursue all my dreams, even the ones on the other side of the world. Your love and support mean the world to me, and I cannot wait for the next time I am back home.

Abstract

Terahertz (THz) time-domain spectroscopy and optical-pump THz-probe (OPTP) spectroscopy are powerful, non-contact methods for probing charge transport in semiconductors with sub-picosecond time resolution. This thesis advances both the instrumentation and analysis of THz spectroscopy, enabling accurate evaluation of material parameters. These refined tools are then applied to the characterisation and optimisation of technologically important III–V semiconductors.

First, I develop spintronic THz emitters with specially designed dielectric coatings: a high-reflectivity stack that suppresses residual transmission of the 800 nm pump by over 99.9%, and an anti-reflective coating that increases the excitation pump intensity inside the emitter. The coated emitters block transmission of the excitation pump, preventing undesirable photoexcitation of the sample and protecting sensitive detection optics. Furthermore, the emitted THz electric field is increased by roughly 40% compared to uncoated emitters, improving the measurement's signal-to-noise ratio.

Next, using the coated emitters, I investigate the relationship between geometric resonances in THz photoconductivity spectra and the size of features in micro/nanostructured GaAs. An inverse relationship between resonant frequency and feature size is established through measurements of nanowire ensembles and well-defined microsquare arrays. The surface plasmon model is validated as a method to separate the resonance from the intrinsic material properties, thus enabling precise measurement of the intrinsic charge-transport parameters.

Finally, OPTP spectroscopy is utilised to characterise and optimise $In_{0.53}Ga_{0.47}As$ via two different tuning mechanisms: incorporation of Fe during growth and application of uniaxial strain. Fe doping reduces electron lifetimes to less than a picosecond while maintaining high mobility, whereas uniaxial strain has little impact on the electronic properties of $In_{0.53}Ga_{0.47}As$. These results inform practical device design of high-speed optoelectronics operating at telecommunication wavelengths.

Contents

List of Publications viii

List of Conference Presentations ix

1 Introduction 1
- 1.1 Thesis Overview . . . 2

2 Terahertz Spectroscopy 4
- 2.1 Terahertz Time-Domain Spectroscopy . . . 5
- 2.2 Optical-Pump THz-Probe Spectroscopy . . . 7
- 2.3 Beam Size and Effective Areal Overlap . . . 11
  - 2.3.1 Razor Blade Measurement . . . 12
  - 2.3.2 Determining Spatial Overlap of Pump and THz Beams . . . 13
- 2.4 THz Generation . . . 15
  - 2.4.1 Photoconductive Antennas . . . 16
  - 2.4.2 Spintronic THz Emitters . . . 18
- 2.5 THz Detection . . . 21
  - 2.5.1 Photoconductive Antennas . . . 21
  - 2.5.2 Electro-Optic Sampling . . . 23
- 2.6 Data Analysis . . . 26
  - 2.6.1 Complex Conductivity . . . 26
  - 2.6.2 Extracting Conductivity of Thin-films . . . 27
  - 2.6.3 Photoconductivity of Nanowire Ensembles . . . 30
  - 2.6.4 Equilibrium Conductivity of Optically Thick Materials . . . 34
- 2.7 Conductivity Models . . . 35
  - 2.7.1 Drude Model . . . 36
  - 2.7.2 Surface Plasmon Model . . . 37

3 Optimised Spintronic Terahertz Emitters for Time-Domain Spectroscopy 42
- 3.1 Introduction . . . 42
- 3.2 Coating Design and Fabrication . . . 44
- 3.3 Experimental Methods . . . 47
  - 3.3.1 THz Time-Domain Spectroscopy . . . 47
  - 3.3.2 Fourier-Transform Infrared Spectroscopy . . . 47

3.4 Results and Discussion . . . 48
3.4.1 Optical Properties . . . 48
3.4.2 Enhancement of THz Emission . . . 49
3.4.3 STE Spatial Dependence on THz Emission . . . 52
3.4.4 THz Time-Domain Spectroscopy of GaAs . . . 54
3.4.5 Effect of Cellulose Nitrate . . . 58
3.5 Conclusion . . . 59

4 Influence of Subwavelength Geometry on Extracting the Electrical Properties of Semiconductors by Terahertz Spectroscopy 61
4.1 Introduction . . . 61
4.2 III–V Semiconductor Nanowires . . . 63
4.2.1 Electronic and Optical Properties . . . 65
4.2.2 GaAs Nanowires . . . 66
4.3 Experimental Methods . . . 69
4.4 Results and Discussion . . . 70
4.4.1 Length Dependence of Nanowires on THz Photoconductivity Spectra 70
4.4.2 GaAs Microsquare Arrays . . . 75
4.4.3 Plasmonic Nature of the Resonance . . . 80
4.5 Conclusion . . . 83

5 Controlling and Characterising the Properties of $In_{0.53}Ga_{0.47}As$ with Terahertz Spectroscopy 86
5.1 Introduction . . . 86
5.2 $In_xGa_{1-x}As$ Material Properties and Literature Review . . . 88
5.2.1 Optimising InGaAs Electron Lifetime, Mobility, and Resistivity . 90
5.3 Experimental Methods: OPTP Setup . . . 96
5.4 Study 1: Characterisation of InGaAs:Fe . . . 98
5.4.1 Material Fabrication . . . 99
5.4.2 Evaluating Electron Lifetime . . . 100
5.5 Study 2: Effect of Mechanical Strain on InGaAs . . . 109
5.5.1 Straining InGaAs on PET . . . 111
5.5.2 X-ray Diffraction . . . 113
5.5.3 THz Spectroscopy . . . 117
5.6 Conclusions . . . 122

6 Conclusion 123
6.1 Outlook . . . 125

Appendices

A Appendix **128**
A.1 Detailed Microsquare Fabrication 128
A.2 InGaAs:Fe Reflection Artefact 129
A.3 Comparison of Excitation Spot Sizes 130
A.4 Calculation of Photoinjected Charge-Carrier Density 131
A.5 Detailed Fabrication of Strained InGaAs on PET samples 134
A.6 Strain Sample Holder Schematics 136
A.7 Converting Strain Axes 137
A.8 Analysis of Substrate Etalon Oscillations 140

References **143**

List of Publications

- **F.M. Wagner**, S. Melnikas, J. Cramer, D.A. Damry, C.Q. Xia, K. Peng, G. Jakob, M. Kläui, S. Kičas, and M.B. Johnston, "Optimised spintronic emitters of terahertz radiation for time-domain spectroscopy", *J. Infrared Millim. Terahertz Waves*, **44**, 52–65 (2023).
- **F.M. Wagner**, T. Haggren, J-C. Bürger, T.J. Keat, K. Peng, C. Uswachoke, D.A. Damry, H. Kraus, H.J. Joyce, H.H. Tan, C. Jagadish, T. Siday, and M.B. Johnston, "The influence of subwavelength geometry on extracting the electrical properties of semiconductors by terahertz spectroscopy", *APL Photonics*, **10**, 076123 (2025).
- **F.M. Wagner**, A. Dohms, T.J. Keat, J.E. Lee, L. Liebermeister, R. Kohlhaas, and M.B. Johnston, "Tailoring electron mobility and ultrashort charge lifetime values in Fe-doped $In_{0.53}Ga_{0.47}As$", manuscript in preparation (2025).
- **F.M. Wagner**, T. Haggren, T.J. Keat, J.R.S. Lilly, J.E. Lee, H.H. Tan, C. Jagadish, and M.B. Johnston, "Effect of (110) uniaxial strain on the electronic properties of $In_{0.53}Ga_{0.47}As$ studied by optical-pump terahertz-probe spectroscopy", manuscript in preparation (2025).
- K. Peng, N.P. Morgan, **F.M. Wagner**, T. Siday, C.Q. Xia, D. Dede, V. Boureau, V. Piazza, A. Fontcuberta i Morral, and M.B. Johnston, "Direct and integrating sampling in terahertz receivers from wafer-scalable InAs nanowires", *Nat. Commun.*, **15**, 103 (2024).
- Q. Yuan, W. Li, **F.M. Wagner**, V. J-Y. Lim, L.M. Herz, J. Etheridge, and M. B. Johnston, "Control over the microstructure of vapor-deposited $CsPbBr_3$ enhances amplified spontaneous emission", *Adv. Opt. Mater.*, accepted (2025).
- L. Wang, K. Peng, T. Haggren, **F.M. Wagner**, H.H. Tan, C. Jagadish, I. Shadrivov, and M.B. Johnston, "All-optical active terahertz metasurfaces for ultrafast polarisation control", manuscript in preparation.

List of Conference Presentations

- **F.M. Wagner**, T. Haggren, J-C. Bürger, T.J. Keat, K. Peng, C. Uswachoke, D. A. Damry, H. Kraus, H.J. Joyce, H.H. Tan, C. Jagadish, T. Siday, and M.B. Johnston, "Exploring the influence of subwavelength geometry on terahertz spectroscopy", *Optical Terahertz Science and Technology (OTST 2024)*, Marburg, Germany, (2024).

- **F.M. Wagner**, S. Melnikas, J. Cramer, D. A. Damry, C.Q. Xia, K. Peng, G. Jakob, M. Kläui, S. Kičas, and M.B. Johnston, "Coated spintronic emitters for improved THz time-domain spectroscopy", *The 48th International Conference on Infrared, Millimeter, and Terahertz Waves*, Montreal, Canada, (2023).

- **F.M. Wagner**, S. Melnikas, J. Cramer, D.A. Damry, C.Q. Xia, K. Peng, G. Jakob, M. Kläui, S. Kičas, and M.B. Johnston, "Optimised spintronic emitters for THz spectroscopy of semiconductor nanowires", *Rank Prize Symposium on Nanowire Photonics*, Grasmere, United Kingdom, (2022).

List of Abbreviations

AR	Anti-reflective (coating)
CMOS	Complementary metal-oxide-semiconductor
CN	Cellulose nitrate
DT	Differential transmission
EM	Electromagnetic
EMT	Effective medium theory
EO	Electro-optic
FDTD	Finite-difference time-domain (simulation)
FM	Ferromagnetic
FTIR	Fourier-transform infrared (spectroscopy)
FWHM	Full width at half maximum
HR	High-reflection/high-reflectivity (coating)
ICP-RIE	Inductively coupled reactive ion etching
IR	Infrared
ISHE	Inverse spin Hall effect
LT	Low-temperature (gallium arsenide)
MBE	Molecular beam epitaxy
MOCVD	Metal-organic chemical vapour deposition
NA	Neutral axis
NM	Non-ferromagnetic
OAP	Off-axis parabolic mirror
OPTP	Optical-pump THz-probe (spectroscopy)
PCA	Photoconductive antenna
SEM	Scanning electron microscope
SIMS	Secondary ion mass spectroscopy
SNR	Signal-to-noise ratio
SRH	Shockley-Read-Hall (recombination)
STE	Spintronic THz emitter
THz	Terahertz
TDS	Time-domain spectroscopy
TO	Transverse optical (phonon)
VLS	Vapour-liquid-solid (growth)
WP	Waveplate
XRD	X-ray diffraction

1

Introduction

Spectroscopy is a widely used technique for understanding materials. By probing how matter absorbs, transmits, scatters, and emits electromagnetic (EM) radiation, we learn about its composition, structure, and electronic transport – all without requiring electrical contacts that can damage the sample or alter its properties. The use of spectroscopy is commonplace in both research and industry, with applications ranging from studying individual atoms to observing distant galaxies.

The information that can be learnt from spectroscopy depends on the region of the EM spectrum used to interrogate the system under study. Among the many spectral regions, the terahertz (THz) frequency range stands out for the richness of information that it can provide. Typically defined as frequencies between 0.1 and 30 THz [1], the THz band sits between the microwave and infrared (IR) regions of the EM spectrum. In semiconductors, the THz band overlaps with free-carrier transport processes, phonon modes, and other low-energy excitations, making THz radiation an excellent probe of the charge-carrier dynamics of semiconductors. Beyond material characterisation, THz radiation plays a crucial role in astronomy, security imaging, pharmaceutical quality control, and next-generation wireless communications – demonstrating the extensive

range of applications that can be exploited with THz waves.

While the THz band offers a wealth of information, it also poses many technical challenges that have slowed THz research and adoption compared to other spectral regions. The foremost challenge is the generation and detection of THz radiation: its frequency is too high to be easily generated by electronics, as microwaves typically are, but also too low frequency to easily generate via optical processes, like how IR light often is. Early work by pioneers of the field (e.g. Auston, Grischkowsky) leveraged ultrafast lasers to produce and detect single-cycle THz pulses using compact emitters and receivers, helping to close the "THz gap" [2, 3]. Today, an assortment of different THz sources exist, including photoconductive antennas [4, 5], electro-optic crystals [6], and spintronic THz emitters [7, 8], all of which can generate broadband, single-cycle pulses of THz radiation. Optical gating methods allow for direct detection of the amplitude and phase information of the THz electric field, enabling direct analysis of pulses without requiring the Kramers–Kronig relations [9, 10]. These advances have made THz spectroscopy widely accessible, stimulating rapid progress over the last few decades.

1.1 Thesis Overview

This thesis advances THz spectroscopy by improving the experimental tools and analysis methods, and applying them to III–V semiconductors. **Chapter 2** introduces THz time-domain and optical-pump THz-probe spectroscopy (THz-TDS and OPTP) in the context of III–V semiconductors. It outlines the components of a THz spectrometer, variations of the technique, and how to analyse the raw data to extract the charge-transport parameters. **Chapter 3** develops coated spintronic THz emitters that suppress 800-nm pump leakage and boost the emitted THz field strength, thereby reducing experimental artefacts and improving the signal-to-noise ratio (SNR). **Chapter 4** explores how subwavelength geometry in GaAs nanowires and microsquare arrays introduces geometric resonances in

THz photoconductivity. The surface plasmon model is validated as a method to separate the geometric effects from the intrinsic response of the material. **Chapter 5** applies the refined tools of the prior chapters to $In_{0.53}Ga_{0.47}As$. Two methods for tuning the electronic properties are explored: introducing Fe dopants during crystal growth, and applying uniaxial strain. OPTP spectroscopy reveals how these mechanisms modify the electron lifetime and mobility of $In_{0.53}Ga_{0.47}As$. The material parameters are mapped, outlining the optimal material for different high-speed applications. Finally, **Chapter 6** summarises the findings of the experimental chapters, frames the results in the broader field, and provides an outlook for future research to build upon this work.

2

Terahertz Spectroscopy

THz spectroscopy is highly suited to studying the charge-carrier dynamics of III–V semiconductors. THz wavelengths correspond to photon energies in the range of 0.4–40 meV, spanning the same energy range as quasiparticles and collective excitations. Furthermore, typical charge-carrier scattering times in inorganic semiconductors are of a similar order of magnitude as THz radiation ($\sim 10^{-13}$ s). As a result, THz spectroscopy can couple to low-energy excitations – such as free carriers, phonon modes, and excitons – and probe the electrical conductivity of inorganic semiconductors [11, 12]. Key material properties such as carrier lifetime, mobility, and recombination dynamics can all be measured in a non-contact manner with sub-picosecond time resolution. These features make THz spectroscopy an ideal tool for the study of optoelectronic materials and devices.

This chapter establishes the methods of terahertz time-domain spectroscopy (THz-TDS) and optical-pump THz-probe (OPTP) spectroscopy used throughout this thesis. It begins with an overview of each technique and the critical components, including THz sources and detectors. The remaining sections describe the data analysis process to extract the charge-transport parameters in bulk and nanostructured III–V semiconductors.

2.1 Terahertz Time-Domain Spectroscopy

TDS differs from other spectroscopic techniques, which typically measure the intensity of light as a function of frequency, and instead measures the electric field amplitude as a function of time. Critically, this means TDS retains both the amplitude and phase information of the light, whereas measurement of the intensity ($I(\omega) \propto |E(\omega)|^2$) loses the phase information. Thus, TDS can simultaneously measure the real and imaginary components of the complex refractive index, $\tilde{n}(\omega) = n(\omega) + i\kappa(\omega)$, without undertaking a Kramers–Kronig analysis [13, 14].

THz-TDS is the most widely used THz spectroscopy technique owing to its flexibility and excellent SNR. The working principle is to measure the amplitude of THz radiation that transmits (or reflects) through a sample as a function of time. In practice, this is achieved by splitting an ultrashort IR laser pulse into two beams: one to excite a THz emitter (THz-generation beam) and one to optically gate a THz detector (gate beam). Once excited, the emitter generates THz radiation into the far-field where it is transmitted through (or reflected off) the sample before being focused onto the detector. The detector is only active when the gate beam excites it. Furthermore, the gate pulse duration ($< 100\,\text{fs}$) is much shorter than THz pulses (picosecond timescale). Therefore, by controlling the relative timing of the gate and THz pulses, usually with precision translation stages, one can measure each point of the THz electric field with resolution determined by the gate pulse duration, as shown schematically in Figure 2.1.

The time-domain signal can be Fourier-transformed to obtain the electric field as a function of frequency. The measured THz electric field through the sample, $E_{\text{sample}}(\omega)$ must be corrected for the spectrometer response to get the THz transmission, $T(\omega)$. This is usually achieved by measuring the THz electric field through a reference, $E_{\text{ref}}(\omega)$, and dividing the sample response by this reference, $T(\omega) = E_{\text{sample}}/E_{\text{ref}}$. The THz

transmission can be related to the complex conductivity of the sample, and different conductivity models can be used to extract key material properties such as the charge-carrier mobility and density [15].

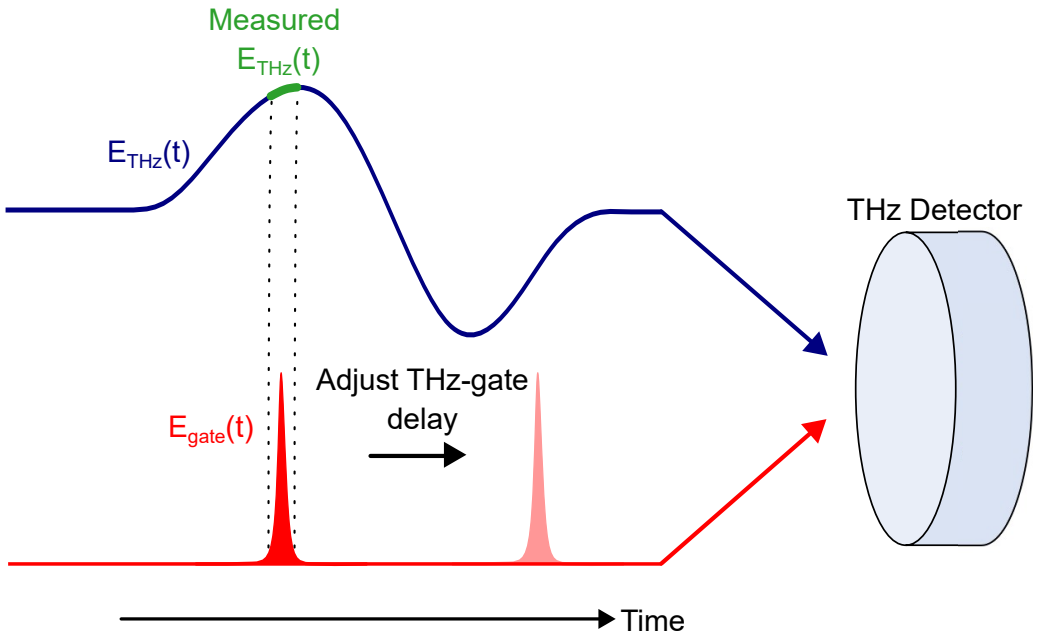

Figure 2.1: Schematic diagram of optical gating to detect THz pulses. Adjusting the relative arrival time of the gate and THz pulses at the THz detector allows for different parts of the THz pulse to be measured.

A schematic of the THz spectrometer used in this thesis is shown in Figure 2.2. A beam block prevents propagation of the optical pump, which is used for OPTP spectroscopy and discussed in Section 2.2. The remaining beam paths form the THz-TDS setup. The amplified Ti:sapphire laser emits ultrafast pulses (35 fs) with 800 nm central wavelength. A beam splitter separates the laser into a gate and a THz-generation beam. Both beams traverse delay lines, with a translation stage in the THz-generation beam controlling the relative timing of the two beams. The THz-generation beam passes through a mechanical chopper that removes every second optical pulse and allows for the THz signal to be separated from the background. A concave lens defocuses the THz-generation beam to reduce its fluence before it excites the THz emitter. Upon excitation, the emitter generates

a THz pulse into the far-field. Off-axis parabolic mirrors (OAPs) collect the THz light and focus it onto the sample. The THz radiation interacts with the sample as it transmits through. A second pair of OAPs collect the transmitted THz and focus it onto the detector. A small hole in the centre of the final OAP allows the gate beam to propagate collinearly with the THz radiation. The detector measures the part of the THz pulse that spatially and temporally overlaps with the gate beam. This spectrometer detects THz radiation through electro-optic sampling (detailed in Section 2.5.2) which encodes the THz signal as a change in the polarisation state of the gate beam that transmits through the detector. Detection of the gate polarisation is completed using a quarter waveplate ($\lambda/4$ WP) to elliptically polarise the light, and then a Wollaston prism spatially separates the polarisation components. A pair of balanced photodiodes measure the intensity of these polarisation components and custom software records the results for later data analysis.

Water vapour has many strong absorption features in the THz frequency range [16]. These features reduce the available THz signal and obscure features originating from the measured sample. Thus, THz spectrometers ideally operate under vacuum or a nitrogen purge. In this thesis, all parts of the spectrometer between the THz emitter and detector are maintained at a vacuum of 1×10^{-3} mbar inside the vacuum box in Figure 2.2.

2.2 Optical-Pump THz-Probe Spectroscopy

OPTP extends THz-TDS by introducing a third beam of light – referred to as the optical-pump beam – that photoexcites the sample before the THz pulse arrives. The THz pulse now interrogates the photoexcited carrier dynamics of the sample, instead of the equilibrium state that is probed in THz-TDS. The ultrafast evolution of the photoexcited sample can be studied by controlling the arrival time of the THz pulse relative to the optical pump. For this reason, OPTP is sometimes known as time-resolved THz spectroscopy [17].

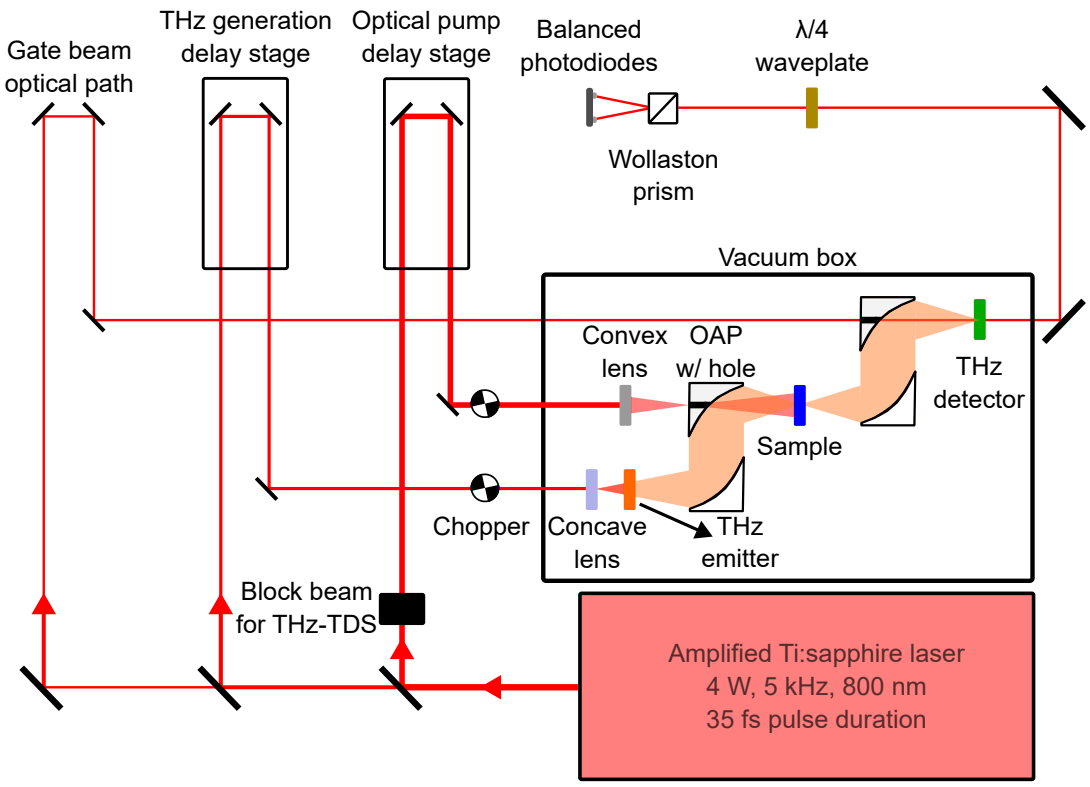

Figure 2.2: Schematic diagram of the THz spectrometer used throughout this thesis. The laser emission is split into three beams: optical-pump, THz-generation, and gate. Arrows indicate the direction of the laser beams along each optical path. The pump beam path is blocked for THz-TDS. Precision translation stages control the relative timing of each beam. Choppers block selected light pulses. OAPs collect the THz light and focus it on the sample and onto the THz detector. Small holes in the OAPs allow the pump (when the beam block is removed for OPTP) and gate beams to travel collinearly with the THz light. THz generation and detection all occur within a vacuum box.

OPTP allows for two different kinds of measurement: measurement of photoconductivity spectra, and measurement of photoconductivity decays [11]. Photoconductivity spectra are obtained by measuring the THz pulse in the time domain some constant time after photoexcitation (THz-generation delay stage moves, optical-pump delay stage stationary). This measurement provides the THz electric field through the photoexcited sample, $E^{\mathrm{on}}_{\mathrm{THz}}(t)$. Photoexcitation modifies the sample's conductivity, resulting in a change in the transmitted THz pulse. The relative change in THz transmission due to the photoexcitation is given by

$$\frac{\Delta T(\omega)}{T(\omega)} = \frac{E^{\text{on}}_{\text{THz}}(\omega) - E^{\text{off}}_{\text{THz}}(\omega)}{E^{\text{off}}_{\text{THz}}(\omega)}, \tag{2.1}$$

where $E^{\text{off}}_{\text{THz}}(\omega)$ is the Fourier transform of the THz electric field transmitted through the unexcited sample (as measured in THz-TDS). This relative change in THz transmission is proportional to the photoconductivity, $\Delta\sigma(\omega)$ [18]. Using OPTP, the photoconductivity spectrum can be measured at different times after excitation, providing insight into the evolution of the photogenerated charge carriers. Figure 2.3 (a) shows example time-domain THz pulses through a sample with and without photoexcitation. These data can be used to extract the photoconductivity spectra (details in Section 2.6).

Photoconductivity decay measurements swap the behaviour of the delay stages; the THz-generation delay stage is stationary while the optical-pump delay stage moves. This reversal means a single point of the THz pulse is probed (typically the pulse peak) while the time after photoexcitation changes. Upon photoexcitation, the peak THz signal will change because of the modified sample conductivity. The peak signal will recover to its equilibrium value as charge-carriers are trapped and recombine. Typically, the relative change in THz transmission due to photoexcitation is recorded, and this value will decrease with time, tracking the decrease in sample photoconductivity. Careful analysis of this decay can reveal the recombination dynamics of the sample and the charge-carrier lifetimes. Figure 2.3 (b) shows an example of a photoconductivity decay measurement.

Removing the beam block in Figure 2.2 converts the THz-TDS system into an OPTP setup. The optical-pump beam timing is controlled by a translation delay stage, and the beam passes through a mechanical chopper. This chopper is synchronised to the chopper the THz-generation beam passes through, except it allows two pulses of the pump beam through before blocking the next two pulses by operating at half the frequency of the THz-generation chopper (here, the THz-generation chopper modulates the beam to 2.5 kHz, optical-pump chopper modulates the beam to 1.25 kHz). Figure 2.4 shows the

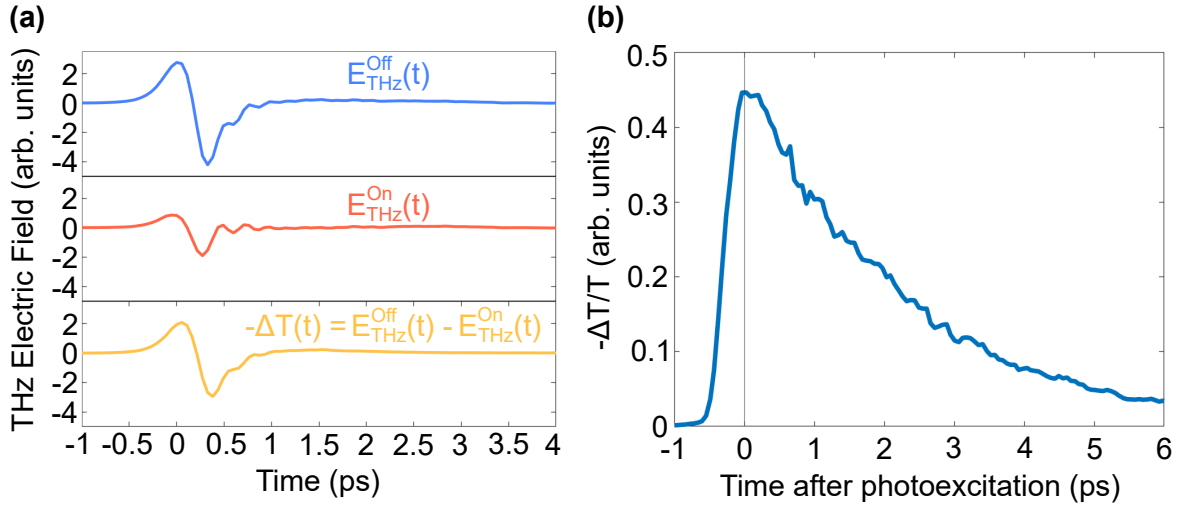

Figure 2.3: Example OPTP measurements. (a) THz electric field through the sample ($In_{0.53}Ga_{0.47}As$) without excitation (top panel), after excitation (middle panel), and the difference between the excited and non-excited cases (bottom panel) in the time domain. The photoconductivity spectrum can be extracted from these data using the methods in Section 2.6. (b) Example photoconductivity decay measurement. $\Delta T/T$ is the relative change in THz signal due to photoexcitation, which is proportional to the photoconductivity. In photoconductivity decay measurements, only the peak value of the THz electric field is measured as a function of time after photoexcitation.

relative timings of the choppers and the resulting train of four pulse combinations. Pulse combinations A and B determine E^{on}_{THz} = A−B, while C and D determine E^{off}_{THz} = C−D. In this way, the THz pulse through the sample at equilibrium and after photoexcitation is measured, and any background signal (chopper phases B and D) removed. All the information necessary to calculate $\Delta T/T$ is acquired simultaneously using this chopper configuration. After the chopper, the optical pump is focussed through a hole in the back of the second OAP and expanded onto the sample. The THz pulse then probes the photoexcited region of the sample and is detected as it was in THz-TDS. Note that the pump beam can partially clip the edges of the hole in the OAP as it passes through, which may introduce non-uniformity to the beam's spatial profile. To minimise the effect of any beam shaping on the charge-carrier distribution, the photoexcited sample was probed at least 1 ps after excitation to allow for initial charge-carrier diffusion.

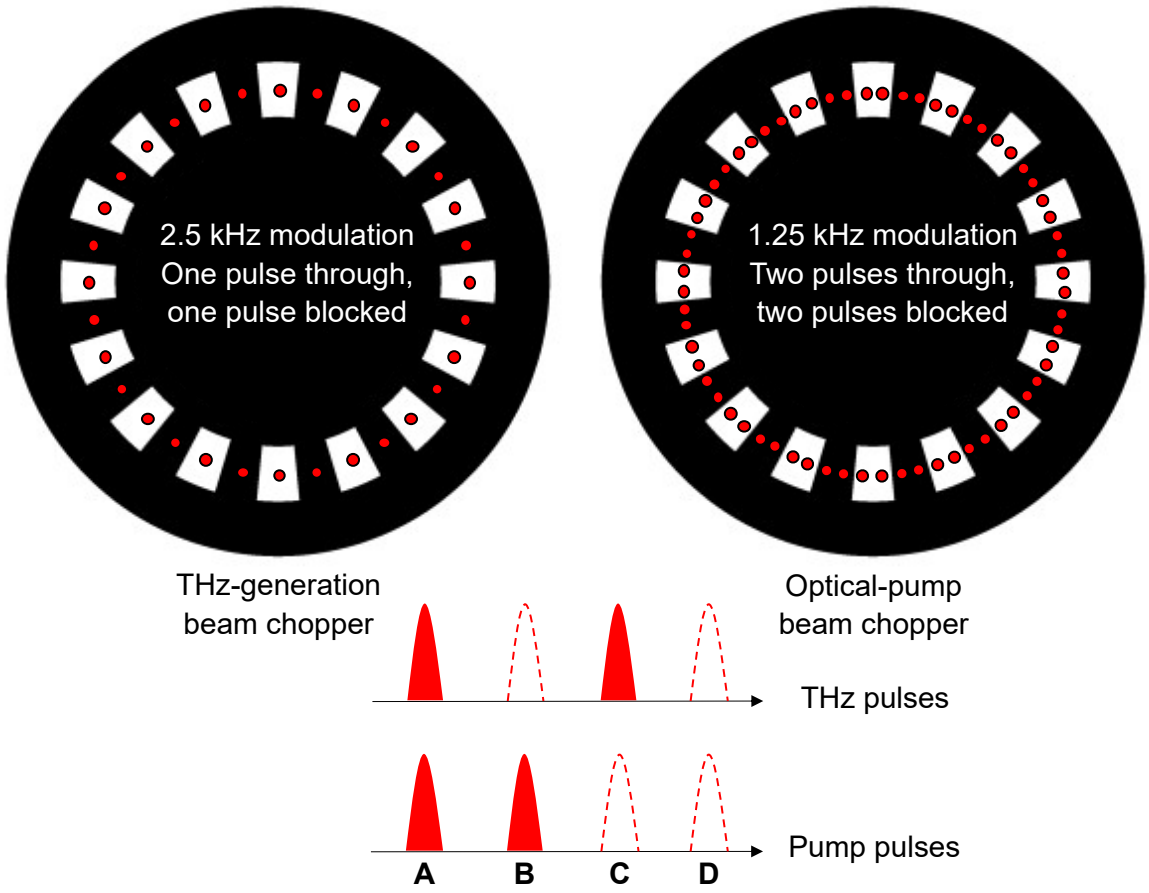

Figure 2.4: Relative timings of the THz-generation and optical-pump beam choppers. The THz-generation chopper modulates the beam at 2.5 kHz (one pulse pass, one pulse block), while the optical-pump chopper modulates at 1.25 kHz (two pulses pass, two pulses block). This synchronization yields a repeating sequence of four distinct states: (A) THz and pump, (B) pump only, (C) THz only, and (D) no signal (gate only).

2.3 Beam Size and Effective Areal Overlap

The optical-pump beam and THz pulse have Gaussian energy distributions, which causes the photoexcited section of the sample to have a spatially varying charge-carrier density. It is important that the THz radiation probes a highly uniform charge-carrier density, otherwise artefacts can arise in the data and extracted parameters lose their physical meaning [19]. Therefore, it is critical that the pump and THz beam sizes and locations are accurately measured. This section describes the procedure used to measure the beam diameters and the method used to calculate the effective areal overlap between

the optical pump and THz probe.

2.3.1 Razor Blade Measurement

The power distribution in one dimension of the pump and THz beams was determined by a razor blade measurement. In this technique, a razor blade mounted on a translation stage moves across the beam in small steps, while the transmitted power is measured at each blade position. The transmitted power will decrease as the blade covers more of the beam, and the size can be determined by fitting the transmitted power as a function of blade position.

Figure 2.5 (a) and (b) show a schematic of the razor blade measurement with the blade moving in the x-direction and blocking all light at $x < x'$, where x' represents the position of the razor edge in the x-plane. The beam is assumed to have a radially symmetric 2D Gaussian profile in the xy-plane. The transmitted power, P, is calculated by integrating the intensity over the unblocked region of the beam

$$P = \frac{P_0}{2\pi\sigma_g^2} \int_{x'}^{\infty} \exp\left(\frac{-x^2}{2\sigma_g^2}\right) dx \int_{-\infty}^{\infty} \exp\left(\frac{-y^2}{2\sigma_g^2}\right) dy, \tag{2.2}$$

where P_0 is the total power and σ_g is the standard deviation of the Gaussian beam profile. The integral in y can be simplified by substituting $a = y/\sqrt{2}\sigma_g$ and evaluating

$$\sqrt{2}\sigma_g \int_{-\infty}^{\infty} \exp(-a^2) da = \sqrt{2\pi}\sigma_g, \tag{2.3}$$

resulting in

$$P = \frac{P_0}{\sqrt{2\pi}\sigma_g} \int_{x'}^{\infty} \exp\left(\frac{-x^2}{2\sigma_g^2}\right) dx. \tag{2.4}$$

This expression can be simplified further by splitting the integral into negative and positive segments

$$P = \frac{P_0}{\sqrt{2\pi}\sigma_g}\left[\int_{x'}^{0} \exp\left(\frac{-x^2}{2\sigma_g^2}\right) dx + \int_{0}^{\infty} \exp\left(\frac{-x^2}{2\sigma_g^2}\right) dx\right]. \tag{2.5}$$

The second term can be simplified by making a similar substitution to the earlier integral in y to obtain

$$P = \frac{P_0}{\sqrt{2\pi}\sigma_g}\left[\int_{x'}^{0} \exp\left(\frac{-x^2}{2\sigma_g^2}\right) dx + \sqrt{\frac{\pi}{2}}\sigma_g\right] = \frac{P_0}{2} - \frac{P_0}{\sqrt{2\pi}\sigma_g}\int_{0}^{x'} \exp\left(\frac{-x^2}{2\sigma_g^2}\right) dx. \tag{2.6}$$

Again, a substitution of the form $b = x'/\sqrt{2}\sigma_g$ can be made to get the integral in the form of an error function

$$P = \frac{P_0}{2} - \frac{P_0}{2}\frac{2}{\sqrt{\pi}}\int_{0}^{x'/\sqrt{2}\sigma_g} \exp(-b^2)db = \frac{P_0}{2}\left(1 - \mathrm{erf}\left(\frac{x'}{\sqrt{2}\sigma_g}\right)\right). \tag{2.7}$$

Thus, the power as a function of blade position can be fitted to Equation 2.7 to extract the Gaussian beam width. Figure 2.5 (c) shows example razor blade measurements for the THz and pump beam. The fits allow the beam widths to be determined and the Gaussian profiles to be reconstructed.

2.3.2 Determining Spatial Overlap of Pump and THz Beams

In OPTP spectroscopy, the THz beam probes the local charge-carrier density of the sample. Therefore, the relevant excitation fluence is not the pump beam fluence, but rather the effective photon fluence, Φ_{eff}, which takes into account the overlapping area between the pump and THz beams [20]. It is the photo-injected carrier density weighted by the THz electric field strength at each spatial position [21]. It is calculated by

$$\Phi_{\mathrm{eff}} = \frac{N}{A_{\mathrm{eff}}} = \int_{0}^{\infty}\int_{0}^{2\pi} \hat{n}_{\mathrm{pump}} f_{\mathrm{THz}} r dr d\theta, \tag{2.8}$$

where N is the total number of photo-injected charge-carriers, A_{eff} is the effective areal overlap of the THz and pump beams, and r and θ are the radial and azimuthal

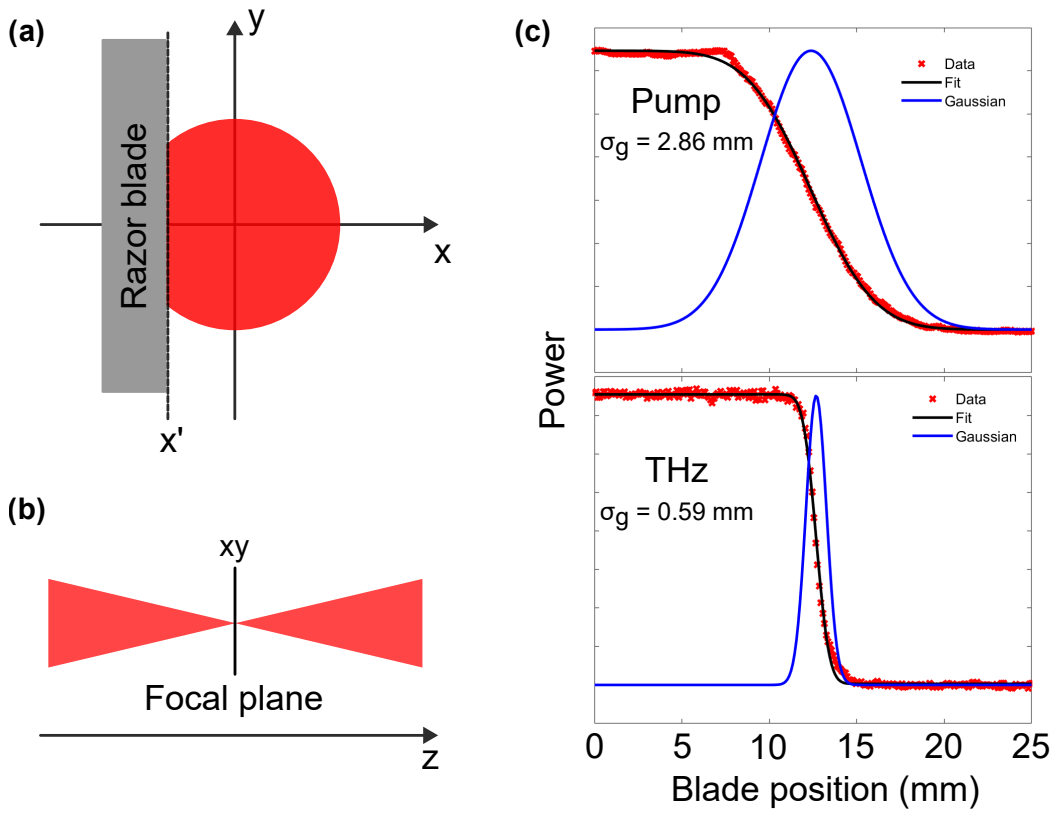

Figure 2.5: Measurement of beam widths. (a) Schematic diagram of the razor blade measurement of beam size. (b) The beam is propagating in the z-direction and the razor blade is positioned in the focal plane – where the sample is usually placed. (c) Pump and THz beam measurements using the razor blade technique. The black line is a fit to the data using Equation 2.7. The Gaussian profile is calculated using the extracted σ_g and beam centre point.

components of the spherical coordinate system. The pump and THz beam 2D spatial distributions are $\hat{n}_{\text{pump}}$ and f_{THz} respectively, which both take the form of Gaussians

$$f_{\text{THz}} = \frac{1}{2\pi\sigma_{\text{THz}}^2} \exp\left(\frac{-r^2}{2\sigma_{\text{THz}}^2}\right), \tag{2.9}$$

$$\hat{n}_{\text{pump}} = N\frac{1}{2\pi\sigma_{\text{pump}}^2} \exp\left(\frac{-r^2}{2\sigma_{\text{pump}}^2}\right). \tag{2.10}$$

Note that $\hat{n}_{\text{pump}}$ is the areal charge density distribution while f_{THz} is the normalized THz areal distribution. Substituting Equations 2.9 and 2.10 into Equation 2.8 results in

$$\frac{N}{A_{\text{eff}}} = \frac{N}{(2\pi)^2\sigma_{\text{THz}}^2\sigma_{\text{pump}}^2}\int_0^{\infty}\int_0^{2\pi}\exp\left(\frac{-r^2}{2}\left(\frac{1}{\sigma_{\text{THz}}^2}+\frac{1}{\sigma_{\text{pump}}^2}\right)\right)rdrd\theta. \tag{2.11}$$

Evaluating the integral gives

$$\frac{N}{A_{\text{eff}}} = \frac{N}{2\pi}\frac{1}{\sigma_{\text{THz}}^2+\sigma_{\text{pump}}^2}. \tag{2.12}$$

Therefore, the effective areal overlap of the pump and THz beams is

$$A_{\text{eff}} = 2\pi(\sigma_{\text{THz}}^2+\sigma_{\text{pump}}^2). \tag{2.13}$$

The beam standard deviations (σ_{THz} and σ_{pump}) are extracted from the razor blade measurements using Equation 2.7. This allows for direct calculation of A_{eff}, which is the area used in this thesis to calculate the effective photon fluences after photoexcitation. Note that the beam widths are often expressed in terms of the beam full-width at half-maximum (FWHM) throughout this thesis. The standard deviations are related to the FWHM by

$$\sigma = \frac{\text{FWHM}}{2\sqrt{2\ln 2}}. \tag{2.14}$$

2.4 THz Generation

Many methods have been developed to generate THz radiation since the development of the Auston switch [2, 22–25]. An overview of different THz emitters can be found in references [26, 27]. This thesis focuses on emitters of broadband, single-cycle THz pulses that require a femtosecond laser pulse to drive a transient charge current. These include, among other techniques, photoconductive antennas (PCAs) [5] and spintronic THz emitters (STEs) [8]. This section discusses these two approaches to generating THz radiation.

2.4.1 Photoconductive Antennas

PCAs are widely used to generate broadband THz pulses into the far-field [4, 5, 28, 29]. Their design is compact and robust, making them compatible with many spectrometer setups. A PCA consists of a pair of biased electrodes on a semiconductor substrate. Their mode of operation can be described by the current surge model [4]: when the gap between the electrodes is illuminated by a femtosecond laser pulse with above-bandgap photon energy, electron-hole pairs are generated in the semiconductor. These charges are accelerated by the electric field between the electrodes. Over time, the photogenerated charges will recombine until the system returns to equilibrium. Thus, the femtosecond laser pulse causes a transient photocurrent between the electrodes that can be described as a Hertzian dipole. The emitted electric field is proportional to the change in current [30, 31]

$$E(t) \propto dI_{\mathrm{PC}}(t)/dt, \tag{2.15}$$

where I_{PC} is the transient photocurrent.

Figure 2.6 (a) illustrates a basic PCA design and how it emits a THz pulse after excitation by a femtosecond laser pulse [5]. Figure 2.6 (b-e) show the relationship between charge carriers generated by the femtosecond pulse and the photocurrent. The carrier generation is proportional to the pump pulse and the photocurrent depends on how many photogenerated carriers exist. The rise time of the photocurrent is approximately the rise time of the pump pulse [5] – this determines the first half-cycle of the THz electric field. The second half-cycle depends on how long the excited carriers take to recombine. Figure 2.6 (e) shows the photocurrent decay for semiconductors with two different lifetimes – the longer lifetime semiconductor supports the photocurrent for longer, which causes the THz pulse to extend in time.

A broadband THz pulse corresponds to a narrow pulse in the time-domain, hence semiconductors with short lifetimes are highly sought for PCAs [32, 33]. Moreover, it is important the semiconductor has a high carrier mobility to increase the photocurrent amplitude, and a high resistivity in its equilibrium state to support high electric fields that further increase the photocurrent and emitted THz electric field amplitude [4, 34]. Low-temperature-grown GaAs (LT-GaAs) is an excellent material for PCAs driven by 800 nm Ti:sapphire lasers owing to its high electron mobility, high dark resistivity, and sub-picosecond charge-carrier lifetime. However, the wide bandgap of LT-GaAs (∼1.42 eV) is not compatible with cost-effective fiber lasers operating at 1550 nm (0.8 eV). Alternative materials such as $In_{0.53}Ga_{0.47}As$ are better suited to these systems because their narrow bandgap (∼0.75 eV) is well-aligned with the telecommunications wavelength. However, the high intrinsic charge-carrier concentration (which leads to low resistivity) and relatively long lifetime (hundreds of picoseconds [35]) of $In_{0.53}Ga_{0.47}As$ limit its performance in PCAs. Modifications to the material, such as introducing deep-level traps via Fe doping, can reduce the carrier lifetime to sub-picosecond levels while increasing the resistivity. Chapter 5 discusses and characterises such Fe-doped $In_{0.53}Ga_{0.47}As$.

Modern PCAs can produce relatively strong and broadband THz radiation (>6 THz bandwidth), achieving an SNR over 110 dB [5, 36]. Careful design of the electrodes and semiconductor substrate can allow for emission of complex modes, such as radially polarised light [37, 38], and for an in-built electric field to replace the need for an externally applied bias between the electrodes [39]. An appropriate semiconductor can be selected to match the central wavelength of common femtosecond lasers, making PCAs accessible in many different lab and industry environments. For example LT-GaAs is well-suited for Ti:sapphire lasers that output 800 nm light, while $In_{0.53}Ga_{0.47}As$ is compatible with fibre lasers operating at 1550 nm [35]. Overall, PCAs are excellent, versatile sources of THz radiation for spectroscopy.

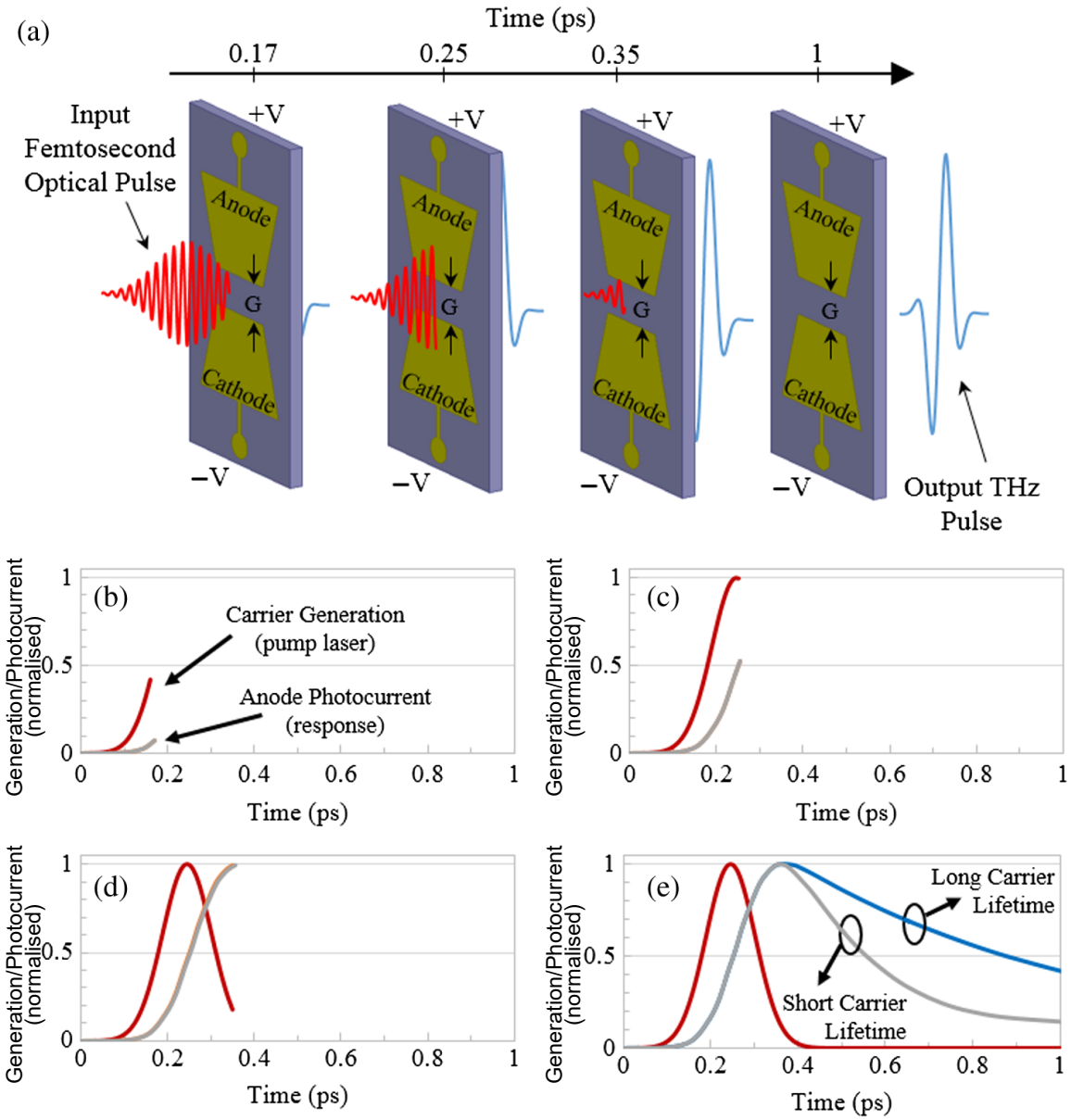

Figure 2.6: Generating THz radiation with a PCA. (a) Illustration of generating a THz pulse using a PCA. (b–e) Relationship between charge carriers generated in the gap (red) and the photocurrent between the electrodes for a short carrier lifetime (grey) and long carrier lifetime (blue) semiconductor. Figure reproduced from [5] with permission.

2.4.2 Spintronic THz Emitters

STEs are a relatively new class of THz emitter, with the first realisations reported in 2013 [40]. They have attracted significant research attention and are increasingly utilised in THz spectrometers thanks to their extremely broadband THz output and compatibility

with existing THz systems [8]. The basic STE design consists of a bilayer of a thin non-ferromagnetic (NM) layer and ferromagnetic (FM) layer. The STE is held in an external magnetic field that controls the spin alignment of electrons in the FM layer. When the femtosecond laser pulse illuminates the STE, it excites electrons in the FM layer to states above the Fermi energy. The excited spin majority and minority electrons have different transport properties (scattering rates, velocities) which causes the diffusion of excited electrons to also drive a net spin current. This spin current travels into the NM layer and is subject to spin-orbit coupling effects. As a result, the spin majority and minority electrons are deflected in different directions, creating a transient charge current that radiates a broadband, single-cycle THz pulse into the far-field [41, 42]. This conversion of a spin current into a charge current is known as the inverse spin Hall effect (ISHE). The deflection of electrons is perpendicular to the spin orientation, which is aligned to the magnetic field direction. As a result, the charge current is perpendicular to the magnetic field and thus the emitted THz pulse is linearly polarised perpendicular to the magnetic field. Figure 2.7 (a–c) show a schematic diagram of STE operation.

Much of the research on STEs has focussed on optimising their properties by tuning the materials and structure [43]. STE bilayers fabricated with different NM layers were found to emit THz radiation with vastly different electric field amplitudes [7, 44]. Heavy metals with strong spin-orbit coupling, like Pt and Pd, resulted in the strongest THz emission. Interestingly, W was found to generate similar amplitude THz electric fields to Pt, except with opposite polarity. This polarity difference is because Pt and W have spin Hall angles of opposite sign, thus they convert spin currents into charge currents moving in opposite directions [45]. Different FM materials have also been investigated, including Fe, Ni, Co and their alloys. Most of these materials resulted in STEs with reasonably similar performance, with $Co_{20}Fe_{60}B_{20}$ producing the largest amplitude THz electric field [7, 46]. Additionally, the effect of thickness of the NM and FM materials

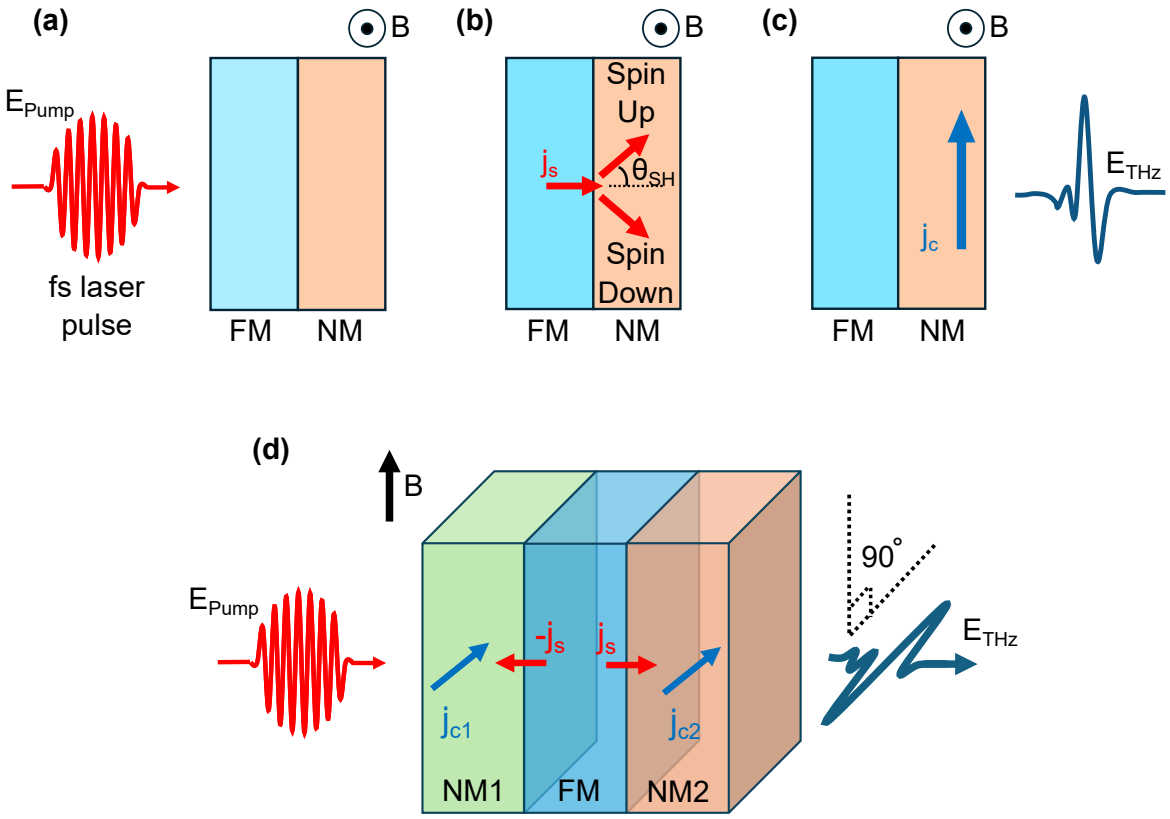

Figure 2.7: Working principles of STEs. (a–c) Illustration of THz generation in a bilayer STE. B is the magnetic field direction. (a) A femtosecond laser pulse excites electrons in the FM layer. (b) A net spin-current (j_s) is injected into the NM layer. Spin-orbit coupling deflects the spin-up and spin-down electron in opposite directions. Angle of deflection is the spin Hall angle θ_{SH}. (c) There is a majority spin population (here, spin-up) and so the deflection causes a net charge current j_c that radiates a THz pulse. (d) Schematic of a trilayer STE. The THz electric field is polarised perpendicular to the magnetic field direction.

on the STE performance has been explored. The results show, somewhat surprisingly, that the THz electric field amplitude decreases as the layer thicknesses increase. Layer thicknesses of 2–4 nm were found to optimise the THz emission from STEs [7, 44, 47].

Many studies have investigated changing the structure of the STE to improve the THz emission. Notably, trilayer structures of a FM layer sandwiched between two different NM layers (NM1/FM/NM2) produce much stronger THz fields than the original bilayer structures [7, 48]. The trilayer requires NM layers with opposite spin Hall angles, such as Pt and W, such that both NM layers produce THz radiation with the same polarity that constructively interfere. Figure 2.7 (d) illustrates such a trilayer STE

design. The trilayer can be further enhanced through dielectric cavities and photonic crystal structures that increase the absorption of the femtosecond laser pulse [49–51]. Chapter 3 discusses the development of anti-reflective and high-reflective coatings for a trilayer STE to enhance THz emission and eliminate harmful transmission of the femtosecond laser through the STE [52].

2.5 THz Detection

Accurate detection of THz radiation is critical to THz spectroscopy. However, its position in the EM spectrum between microwave and IR radiation has made THz detection technically challenging. To bridge the "THz gap", several specialised detection methods have been developed. A comprehensive review of these approaches can be found in Ref [53]. This thesis focuses on detectors used in THz-TDS that utilise optical gating to resolve the THz electric field amplitude and phase with ultrafast time resolution. This section discusses two of the most widely employed detection techniques for THz-TDS: PCAs and electro-optic (EO) sampling.

2.5.1 Photoconductive Antennas

Photoconductive antennas are among the most common technologies for generation (Section 2.4.1) and detection of THz radiation [5, 54]. The PCA design is mostly the same whether it is used for detection or emission, except no external bias is applied between the electrodes for detection. Instead, the optical gate pulse generates free carriers in the gap between the electrodes. When the THz electric field is incident upon the PCA, it accelerates the photogenerated carriers, producing a transient photocurrent between the electrodes. The photocurrent is proportional to the amplitude of the THz electric field. The PCA is activated by the gate pulse and can only detect the THz pulse until the

charge carriers recombine. This allows for measurement of the temporal profile of the THz electric field by adjusting the relative timing of the gate and THz pulses.

PCA THz detectors have many advantages, including their compatibility with different laser systems by selecting appropriate semiconductor materials, direct detection of the electric field phase and amplitude, and high SNR. The similarity between PCA emitters and detectors makes it possible to design all-in-one THz transceivers [55, 56]. Interesting research has also been conducted to develop PCAs where the electrodes are separated by semiconductor nanowires, instead of a bulk semiconductor substrate [57–60]. The nanowire design significantly reduces the detector size and raw material cost while taking advantage of the beneficial charge-carrier dynamics of nanowires (high mobility, short lifetimes, advantageous surface effects) [11, 61, 62]. Furthermore, nanowires are highly polarisation sensitive [63], and PCAs made from nanowire cross-structures can fully resolve the polarisation state of THz radiation [64].

A critical parameter of PCA detectors is the carrier lifetime of the semiconductor [60, 65]. When the lifetime is short ($< 1\,\mathrm{ps}$), such as in LT-GaAs, Fe-doped $In_{0.53}Ga_{0.47}As$, ErAs:GaAs superlattices, and ion-implanted semiconductors [32, 33, 35, 36], the THz electric field is directly measured at the time it overlaps with the optical gate pulse – this regime is called direct detection and is the simplest as it requires no extra processing to recover the THz pulse. When the lifetime is more than $\sim 1\,\mathrm{ps}$ charges remain in the semiconductor after the gate pulse has been absorbed. The THz electric field continues to drive a photocurrent as long as the photoexcited carriers remain. The detector effectively integrates the THz electric field over time, and the photocurrent is proportional to the convolution of the THz electric field and the charge-carrier response function. This regime is called integrating detection, and requires additional processing to recover the true THz electric field. For this reason, it is highly desirable to use semiconductors with sub-ps carrier lifetimes to ensure the PCA detector operates in the direct detection mode.

2.5.2 Electro-Optic Sampling

EO sampling is a widely used THz detection method that leverages the Pockels (linear electro-optic) effect – a nonlinear optical process in which an applied electric field induces a change in the refractive index of non-centrosymmetric crystals (EO crystals) [9, 66, 67]. In EO sampling, an optical pulse (the gate) co-propagates with a THz pulse through an EO crystal, such as ZnTe, GaP, or GaSe. The THz pulse induces a birefringence in the crystal that is linearly proportional to the THz electric field amplitude. Consequently, the polarisation state of the gate pulse is altered by the birefringence, and the amount of polarisation change is related to the THz electric field that spatially and temporally overlaps with the gate in the EO crystal. Therefore, measurement of the gate's polarisation change as a function of THz pulse arrival time allows for reconstruction of the full THz electric field.

The polarisation change is typically detected using a balanced detection scheme involving a $\lambda/4$ WP, Wollaston prism, and pair of balanced photodiodes. In the absence of a THz field (for example, when it is blocked by the mechanical choppers), the linear polarisation of the gate pulse is converted to circular polarisation by the $\lambda/4$ WP. The Wollaston prism then splits the gate into its orthogonal polarisation components. Since the gate is circularly polarised, the orthogonal components have equal intensities, which results in a balanced signal at the photodiodes and no net voltage measurement. When the THz pulse is present, the gate's polarisation changes in the EO crystal due to the induced birefringence. Now, the $\lambda/4$ WP elliptically polarises the gate and the two polarisation components split by the Wollaston prism have different intensities, resulting in a voltage difference across the balanced photodiodes. This voltage signal is proportional to the THz electric field at the moment it overlaps with the gate within the EO crystal. A schematic of the EO detection system is shown in Figure 2.8, with its implementation in the THz spectrometer also visible in Figure 2.2.

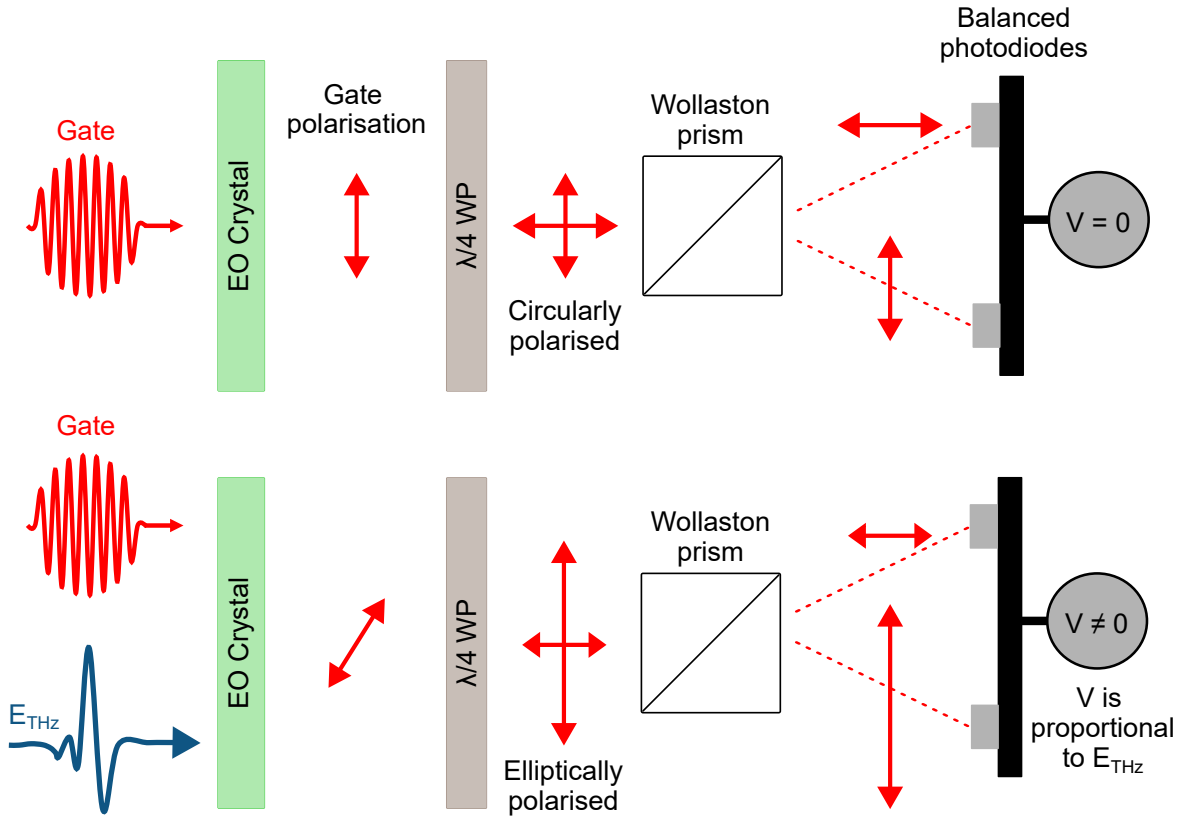

Figure 2.8: Schematic diagram of THz detection via EO sampling. (Top) the gate pulse is linearly polarised after transmission through the EO crystal such that the $\lambda/4$ WP circularly polarises it. The balanced photodiodes measure no voltage difference as the orthogonal polarisation components are equal. (Bottom) the THz electric field induces a birefringence in the EO crystal that changes the polarisation state of the gate. Now, the $\lambda/4$ WP elliptically polarises the gate and a non-zero voltage difference is measured across the photodiodes that is proportional to the THz electric field amplitude. Note the schematic is not to scale as the THz electric field is much longer in duration than the gate pulse (several picoseconds compared to < 100 fs).

THz detection via EO sampling has several advantages. Most notably, EO sampling does not depend on carrier dynamics that can smear sharp features in PCAs. Therefore, the temporal resolution of EO sampling is primarily limited by the gate pulse duration. Moreover, the detection bandwidth is mainly limited by the phonon modes of the EO crystal, which allows EO sampling to often reach bandwidths of 5–10 THz [7]. Additionally, EO sampling requires no contacts or electrodes, simplifying its implementation, and it can be used to directly measure individual THz polarisation components by carefully selecting the EO crystal and detection optics [68, 69].

The choice of EO crystal is very important for extracting the most information possible. The amount of polarisation change in the gate, and hence the signal strength, depends on the electro-optic coefficient, while the bandwidth depends on the phonon modes. For example, (110) ZnTe is an excellent EO crystal owing to its large electro-optic coefficient, however it exhibits strong phonon absorption above $\sim 3.7\,\mathrm{THz}$ that restricts its detection bandwidth [10]. In contrast, (110) GaP can reliably detect up to $\sim$8 THz because of its higher phonon resonance frequency, however it has a lower electro-optic coefficient than ZnTe, which reduces the measurement sensitivity.

For accurate reconstruction of the THz pulse, EO sampling requires phase matching between the gate and THz pulses as they propagate through the EO crystal. The refractive index is often very different at optical and THz frequencies, hence thin crystals are necessary for maintaining the phase matching condition and resolving the high frequency THz components. However, the gate accumulates less polarisation change after propagating through a thin crystal compared to a thick one, hence there is a trade-off between signal strength and detection bandwidth. Another consequence of using a thin EO crystal is interference from reflections of the THz pulse within the crystal (etalon echoes). These reflections are typically eliminated by time-windowing the measured signal, but short time windows cut off the high-frequency THz components. To solve this problem, the EO crystal can be optically contacted to a non-EO crystal, such as a symmetric cut of the same crystal, to extend the time window before reflections occur, allowing high-frequency signals to be cleanly obtained. In this thesis, THz detection is typically achieved by EO sampling with a 200 μm (110) GaP crystal that is optically contacted to several millimetres of (100) GaP, enabling a THz detection bandwidth of $\sim$8 THz without etalon interference from the EO crystal.

2.6 Data Analysis

THz-TDS measures the amplitude and phase of the THz electric field after transmission through a sample. Comparison of the THz pulse transmitted through the sample to the THz pulse through the reference (typically air/vacuum or a bare substrate) allows for the complex conductivity of the sample to be determined. Careful fitting of the conductivity to a physical model allows for the charge-carrier dynamics of the sample to be extracted. This section details what complex conductivity is and how it relates to the complex permittivity and complex refractive index before explaining the analysis process for thin-films, optically thick samples, and for composite materials such as nanowire ensembles. The final section discusses the conductivity models used in the experimental chapters of this thesis.

2.6.1 Complex Conductivity

There are several ways to quantify how a material responds to electromagnetic radiation. A common quantity is the complex refractive index, $\tilde{n}(\omega) = n(\omega) + i\kappa(\omega)$, which is often used to determine transmission and reflection coefficients [70]. Alternatively, the material response can be described by the complex permittivity (dielectric), $\tilde{\epsilon}(\omega) = \epsilon_1(\omega) + i\epsilon_2(\omega)$. The permittivity describes the polarisability of a material in response to an electric field and is related to the complex refractive index by $\tilde{n}^2(\omega) = \tilde{\epsilon}(\omega)$. The lattice contributions to the permittivity, such as phonon modes, can be separated from the free charge contribution:

$$\tilde{\epsilon}(\omega) = \epsilon_L + \frac{i\tilde{\sigma}(\omega)}{\epsilon_0 \omega}, \tag{2.16}$$

where ϵ_L is the lattice contribution to the permittivity, $\tilde{\sigma} = \sigma_1(\omega) + i\sigma_2(\omega)$ is the complex conductivity of the free carriers, and ϵ_0 is the permittivity of free space ($8.854 \times 10^{-12}\,\mathrm{Fm}^{-1}$) [11, 15, 18]. In THz-TDS, the lattice contribution arises from

transverse optical (TO) phonons. A polar semiconductor with one TO phonon has a lattice contribution to the permittivity of

$$\epsilon_L(\omega) = \epsilon_\infty + (\epsilon_\mathrm{s} - \epsilon_\infty)\frac{\omega_\mathrm{TO}^2}{\omega_\mathrm{TO}^2 - \omega^2 - i\omega\Gamma}, \tag{2.17}$$

where ϵ_∞ and ϵ_s are the high-frequency and static dielectric constants for the material, ω_TO is the resonant frequency of the TO phonon, and Γ is the phonon damping rate. These numbers are well-known for many materials.

Thus, the complex refractive index, permittivity, and conductivity are all equivalent ways to describe the material response to light. In this thesis, the focus is primarily on extracting the complex conductivity using THz spectroscopy.

2.6.2 Extracting Conductivity of Thin-films

Consider a thin-film sample of thickness L and refractive index $\tilde{n}_\mathrm{sam}$ on top of a substrate of thickness D and refractive index $\tilde{n}_\mathrm{sub}$ inside a vacuum ($\tilde{n}_\mathrm{vac} = 1$). The THz pulse (a plane wave) travels through vacuum until it hits the sample at normal incidence. Some of the light is transmitted, some reflected, and some absorbed. There are also internal reflections within the sample and the substrate to consider. A common assumption is that the substrate is thick enough to temporally window out internal reflections within the substrate [71]. The transmitted light through the sample, T_sam, depends on the properties of the sample and substrate. To isolate the sample properties, it is essential to also measure the THz transmission through the bare substrate (or through vacuum if the sample is free standing), T_sub. Figure 2.9 (a) and (b) show the experiment geometry for these measurements.

The THz transmission through the sample, T_sam, can be explicitly written by considering the propagation of the THz wave as it goes from vacuum to the sample and then into the substrate and finally to the detector:

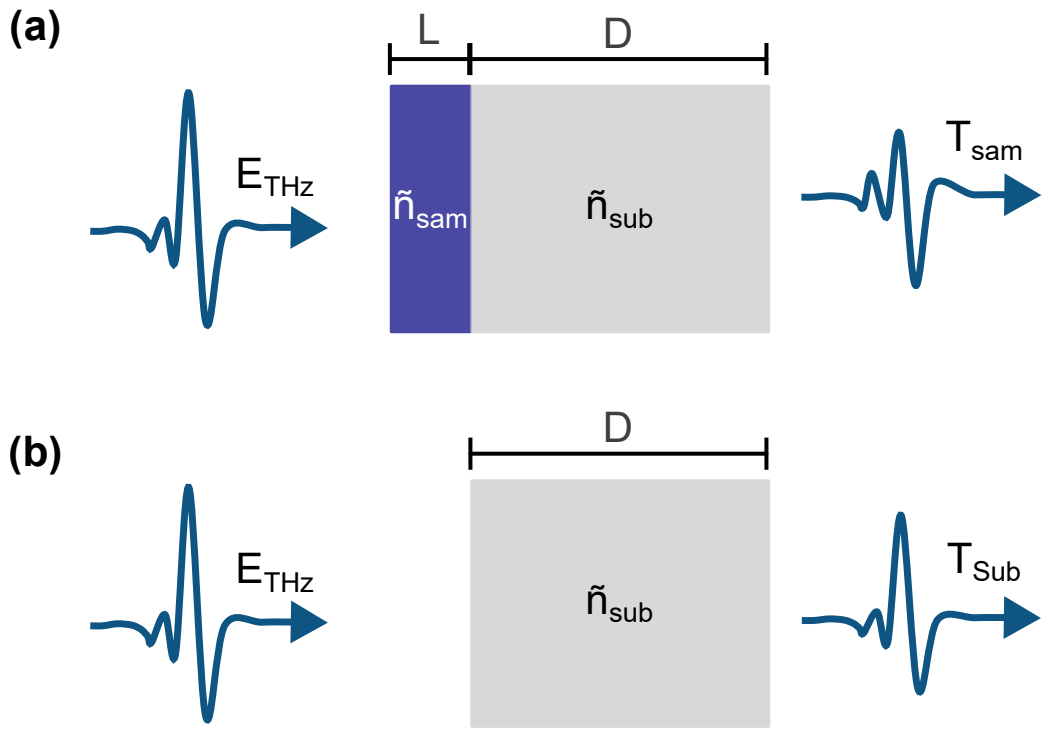

Figure 2.9: Schematic of the difference between sample and reference THz measurements. Transmission of the THz pulse through the sample (a) and through the bare substrate (reference) (b).

$$T_{\text{sam}} = t_{\text{vac|sam}} t_{\text{sam|sub}} \exp(i\tilde{n}_{\text{sam}} L\omega/c) \times \text{FP} \times \psi. \tag{2.18}$$

Here, $t_{i|j} = 2\tilde{n}_i/(\tilde{n}_i + \tilde{n}_j)$ is the Fresnel coefficient for transmission through medium i into medium j at normal incidence, the exponential term describes propagation of the wave (assumed to be a plane wave at normal incidence) through the *sample*, FP is the Fabry-Pérot term that accounts for multiple internal reflections in the *sample*, and ψ is the propagation through the substrate. Note that the Fabry-Pérot term for the *substrate* is 1, as the internal reflections of the relatively thick substrate can be windowed out and thus do not impact the detected transmitted THz electric field. In the thin-film limit, the FP term becomes

$$\mathrm{FP} = \sum_{p=0}^{\infty} (r_{\mathrm{vac|sam}} r_{\mathrm{sam|sub}} \exp(2i\tilde{n}_{\mathrm{sam}} L\omega/c))^p = \frac{1}{1 - r_{\mathrm{vac|sam}} r_{\mathrm{sam|sub}} \exp(2i\tilde{n}_{\mathrm{sam}} L\omega/c)}, \tag{2.19}$$

where p is the number of internal reflections (∞ in the thin-film limit) and $r_{i|j} = (\tilde{n}_i - \tilde{n}_j)/(\tilde{n}_i + \tilde{n}_j)$ is the Fresnel reflection coefficient between media i and j. The transmission of light through the bare substrate, T_{sub}, can be written in a similar way

$$T_{\mathrm{sub}} = t_{\mathrm{vac|sub}} \exp(i\tilde{n}_{\mathrm{vac}} L\omega/c) \times \psi. \tag{2.20}$$

Note that ψ contains all propagation terms within the substrate. The relative transmission function through the sample is then given by

$$\frac{T_{\mathrm{sam}}}{T_{\mathrm{sub}}} = \frac{t_{\mathrm{vac|sam}} t_{\mathrm{sam|sub}} \exp(i(\tilde{n}_{\mathrm{sam}} - \tilde{n}_{\mathrm{vac}})L\omega/c)}{t_{\mathrm{vac|sub}}(1 - r_{\mathrm{vac|sam}} r_{\mathrm{sam|sub}} \exp(2i\tilde{n}_{\mathrm{sam}} L\omega/c))}. \tag{2.21}$$

Equation 2.21 can be simplified using the thin-film approximation: $\tilde{n}_{\mathrm{sam}}\omega L/c << 1$. Satisfying this condition, we can use the approximation $\exp(i\theta) = \cos(\theta) + i\sin(\theta) \sim 1 + i\theta$, where θ is small. Applying these approximations and using $\tilde{n}_{\mathrm{vac}} = 1$ results in the expression [11, 15, 72]

$$\frac{T_{\mathrm{sam}}}{T_{\mathrm{sub}}} = \frac{1 + \tilde{n}_{\mathrm{sub}}}{(1 + \tilde{n}_{\mathrm{sub}}) - i(\tilde{n}_{\mathrm{sam}}^2 + \tilde{n}_{\mathrm{sub}})\omega L/c}. \tag{2.22}$$

This equation can be rearranged to solve for $\tilde{n}_{\mathrm{sam}}^2 = \tilde{\epsilon}_{\mathrm{sam}}$

$$\tilde{\epsilon}_{\mathrm{sam}} = \frac{ic}{\omega L}(1 + \tilde{n}_{\mathrm{sub}}) \left(\frac{T_{\mathrm{sub}}(\omega)}{T_{\mathrm{sam}}(\omega)} - 1 \right) - \tilde{n}_{\mathrm{sub}}. \tag{2.23}$$

The permittivity is related to conductivity by Equation 2.16. Making this substitution and rearranging gives the complex conductivity of the sample

$$\tilde{\sigma}_{\mathrm{sam}} = \frac{\epsilon_0 c}{L}(1 + \tilde{n}_{\mathrm{sub}}) \left(\frac{T_{\mathrm{sub}}(\omega)}{T_{\mathrm{sam}}(\omega)} - 1 \right) + i\omega\epsilon_0(\epsilon_L + \tilde{n}_{\mathrm{sub}}). \tag{2.24}$$

For highly conductive samples, the conductivity can be further approximated as

$$\tilde{\sigma}_{\text{sam}} = \frac{\epsilon_0 c}{L}(1 + \tilde{n}_{\text{sub}}) \left(\frac{T_{\text{sub}}(\omega) - T_{\text{sam}}}{T_{\text{sam}}(\omega)} \right). \tag{2.25}$$

Equation 2.25 is the common approximation for relating the conductivity to the THz transmission when the sample is at equilibrium.

When the sample is photoexcited, we are interested in extracting the complex photoconductivity. We assume that the photoexcitation is uniform throughout the sample, which is a reasonable assumption for thin-films excited by above-bandgap light. The complex photoconductivity, $\Delta\tilde{\sigma}$, is related to the relative change in THz transmission due to the photoexcitation, $\Delta T/T$, where $\Delta T = T_{\text{on}} - T_{\text{off}}$ is the difference is transmission when the sample is photoexcited and at equilibrium, and $T = T_{\text{off}}$. The relationship between photoconductivity and $\Delta T/T$ can be derived in a similar way to Equation 2.25, with T_{sam} and T_{sub} replaced by T_{on} and T_{off} respectively. The resulting equation for photoconductivity is ([18])

$$\Delta\tilde{\sigma} = -\frac{\epsilon_0 c(1 + \tilde{n}_{\text{sub}})}{L} \frac{\Delta T}{T_{\text{on}}}. \tag{2.26}$$

Therefore, the equilibrium conductivity of a thin-film sample can be determined by measuring the THz transmission through the sample and a bare substrate (or vacuum for a free standing sample), while the photoconductivity can be calculated from the THz transmission through the sample with and without photoexcitation.

2.6.3 Photoconductivity of Nanowire Ensembles

Nanowire ensembles form an important part of the experimental work in Chapter 4 and their analysis requires special consideration. They can be considered as a composite layer consisting of the nanowires and their surrounding medium – typically vacuum or polymer – on a substrate [73–75]. Figure 2.10 shows a schematic diagram of this sample

structure. The effective conductivity and photoconductivity of the composite layer can be calculated using the thin-film equations (Equations 2.25 and 2.26 respectively) [11].

To extract the conductivity of the nanowires, it is necessary to separate the nanowire response from that of the surrounding medium. One widely used approach is to apply an effective medium theory (EMT). Common EMTs for this task are the Maxwell-Garnett and Bruggeman EMTs [76, 77]. However these models require assumptions about the nanowire geometry and are not suitable when nanowires bundle together [11, 73].

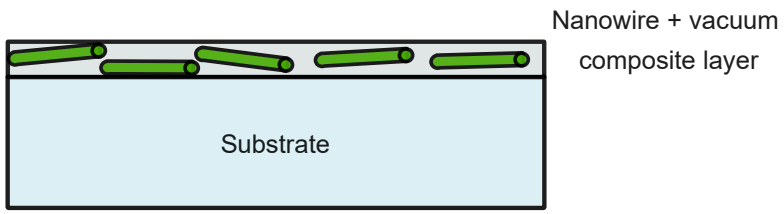

Figure 2.10: Schematic diagram of a nanowire ensemble forming a composite layer with the surrounding dielectric (vacuum).

Alternatively, the nanowire photoconductivity can be extracted by explicitly considering the nanowire geometry – particularly the length, diameter, and surface density – in a thin-film approximation [74, 78]. This approach assumes that the nanowires act as discrete, subwavelength conductive elements in a transparent medium with some thickness, L. The nanowire collective response is assumed to be proportional to the density of nanowires and their individual responses. In this model, the nanowire photoconductivity is related to the THz transmission by measuring the transmission through the nanowire ensemble with and without photoexcitation. Assuming the nanowires are embedded in vacuum, the transmitted THz electric fields before and after photoexcitation are

$$T_{\text{off}} = f_{\text{nw}} T_{\text{nw}} + (1 - f_{\text{nw}}) T_{\text{vac}} \tag{2.27}$$

$$T_{\text{on}} = f_{\text{nw}} T_{\text{nw}^*} + (1 - f_{\text{nw}}) T_{\text{vac}}, \tag{2.28}$$

where f_{nw} is the nanowire areal fill factor, T_{nw} and T_{vac} are the transmitted THz electric fields through the nanowire and vacuum sections of the composite layer respectively, and T_{nw^*} indicates that the nanowires are photoexcited. Each of the electric field terms can be expressed in terms of the incident THz electric field, E_i:

$$T_{\text{vac}} = \exp(i\omega L/c) E_i \tag{2.29}$$

$$T_{\text{nw}} = t_{\text{vac|nw}} t_{\text{nw|vac}} \text{FP}_{\text{vwv}} \exp(i\tilde{n}\omega L/c) E_i \tag{2.30}$$

$$T_{\text{nw}^*} = t_{\text{vac|nw}^*} t_{\text{nw}^*\text{|vac}} \text{FP}_{\text{vw}^*\text{v}} \exp(i\tilde{n}^*\omega L/c) E_i. \tag{2.31}$$

The Fabry Pérot terms, FP_{ijk}, have subscripts that indicate the interfaces the light reflects between, and $\tilde{n}$ and $\tilde{n}^*$ are the nanowire refractive indices at equilibrium and after photoexcitation respectively. Note that the vacuum refractive index equals 1 and does not change with photoexcitation. The relative change in transmitted THz electric field is given by

$$\frac{\Delta T}{T} = \frac{T_{\text{on}} - T_{\text{off}}}{T_{\text{off}}} = \frac{f_{\text{nw}} T_{\text{nw}^*} + (1 - f_{\text{nw}}) T_{\text{vac}}}{f_{\text{nw}} T_{\text{nw}} + (1 - f_{\text{nw}}) T_{\text{vac}}} - 1. \tag{2.32}$$

This equation can be rearranged to isolate the nanowire transmission terms

$$\frac{T_{\text{nw}^*}}{T_{\text{nw}}} = \frac{\Delta T}{T} \left[1 + \frac{(1 - f_{\text{nw}})}{f_{\text{nw}}} \frac{T_{\text{vac}}}{T_{\text{nw}}} \right] + 1. \tag{2.33}$$

The composite layer is very thin as the nanowire diameter is small (often on the scale of tens to hundreds of nanometres). Therefore, the thin-film approximation is valid and the simplification $T_{\text{vac}}/T_{\text{nw}} \approx 1$ can be made. Equation 2.33 becomes

$$\frac{T_{\text{nw}^*}}{T_{\text{nw}}} = \frac{\Delta T}{T} \frac{1}{f_{\text{nw}}} + 1. \tag{2.34}$$

We can define the parameter $A = T_{\mathrm{nw}}/T_{\mathrm{nw}^*}$ that will be used later. We can use Equations 2.30 and 2.31 with thin-film approximations made to simplify the t_{ij} and FP_{ijk} terms to get

$$\frac{1}{A} = \frac{T_{\mathrm{nw}^*}}{T_{\mathrm{nw}}} = \frac{2 - i(\tilde{n}^2 + 1)\omega L/c}{2 - i(\tilde{n^*}^2 + 1)\omega L/c}. \tag{2.35}$$

Substituting in the permittivity for refractive index, $\tilde{n}^2 = \epsilon$, and rearranging results in

$$\epsilon^* = \frac{T_{\mathrm{nw}}}{T_{\mathrm{nw}^*}}\left((1+\epsilon) - \frac{2c}{i\omega L}\right) + \frac{2c}{i\omega L} - 1, \tag{2.36}$$

where ϵ^* is the permittivity of the photoexcited nanowires. The photoconductivity is given by

$$\epsilon^* - \epsilon = \frac{i\Delta\sigma}{\omega\epsilon_0}. \tag{2.37}$$

Substituting Equation 2.37 into Equation 2.36 and solving for photoconductivity gives

$$\Delta\sigma = \frac{\omega\epsilon_0}{i}\left(\frac{T_{\mathrm{nw}}}{T_{\mathrm{nw}^*}}\left((1+\epsilon) - \frac{2c}{i\omega L}\right) + \frac{2c}{i\omega L} - 1 - \epsilon\right). \tag{2.38}$$

Finally, we can simplify the above and substitute the parameter A to get the nanowire photoconductivity

$$\Delta\sigma = (A-1)\left[\frac{2c}{L} - i\omega(1+\epsilon)\right]\epsilon_0. \tag{2.39}$$

Using Equation 2.39 to extract the nanowire photoconductivity requires few assumptions about the nanowire geometry while providing insight into the carrier dynamics of the individual nanowires. These traits are highly relevant to the work in Chapter 4, hence Equation 2.39 is used in this thesis over alternative EMT approaches.

2.6.4 Equilibrium Conductivity of Optically Thick Materials

In the case of thick samples, the thin-film approximation ($\tilde{n}\omega L/c << 1$) is no longer valid. Therefore, we must alter the approach to calculate the material conductivity. The relevant case in this thesis is a free-standing sample of thickness L (where L is large relative to the wavelength) at equilibrium. The transmitted THz electric field through the sample is a modified form of Equation 2.18

$$T_{\text{sam}} = t_{\text{vac|sam}} t_{\text{sam|vac}} \exp(i\tilde{n}_{\text{sam}} L\omega/c) E_i, \tag{2.40}$$

where E_i is the incident THz electric field that replaces the substrate propagation term, ψ from Equation 2.18. Note that Equation 2.40 has no Fabry-Pérot term because the internal reflections in the thick sample can be temporally windowed out. The reference transmission through vacuum is given by

$$T_{\text{vac}} = \exp(i\tilde{n}_{\text{vac}} L\omega/c) E_i. \tag{2.41}$$

The relative transmission then equals

$$\frac{T_{\text{sam}}}{T_{\text{vac}}} = \frac{4\tilde{n}_{\text{sam}}}{(1+\tilde{n}_{\text{sam}})^2} \exp(i(\tilde{n}_{\text{sam}} - 1) L\omega/c), \tag{2.42}$$

where the Fresnel transmission coefficients have been expanded and the vacuum refractive index is set to 1 [71]. Equation 2.42 has no analytic solution for the refractive index; instead numerical methods are required. However, the roots of the transmission function oscillate as a function of $\tilde{n}_{\text{sam}}$, which prevents convergence with standard numerical techniques such as the Newton-Raphson method [79]. An alternative error function should be used

$$\xi(n,\kappa) = \xi^2_{\text{mod}}(n,\kappa) + \xi^2_{\text{arg}}(n,\kappa), \tag{2.43}$$

where $\tilde{n}_{\text{sam}} = n + i\kappa$,

$$\xi_{\text{mod}} = \ln(|T(\omega)|) - \ln(|T_{\text{meas}}(\omega)|), \tag{2.44}$$

and

$$\xi_{\text{arg}} = \arg(T(\omega)) - \arg(T_{\text{meas}}(\omega)). \tag{2.45}$$

T_{calc} and T_{meas} are the calculated (with Equation 2.42) and measured values of the THz transmission function. The two functions, ξ_{mod} and ξ_{arg}, are smooth and monotonous, ensuring the overall error function, ξ will converge [71, 79]. Therefore, the complex refractive index of a thick, free-standing sample can be determined by finding the roots of the error function ξ. The permittivity and conductivity can then be determined, as described in Section 2.6.1.

2.7 Conductivity Models

THz-TDS and OPTP spectroscopy yield the dark (equilibrium) conductivity and photoconductivity spectra respectively. Fitting these spectra to physical models provides key insights into the charge-carrier dynamics of the sample and allows for important material parameters – such as the carrier density, relaxation time, and mobility – to be extracted. This section presents the relevant conductivity models for the material systems investigated in this thesis: the Drude model and the surface plasmon model. Note that, unless otherwise stated, all fitting of conductivity models or polynomials to experimental data in this thesis is done by a nonlinear least squares algorithm with the data weighted by the inverse of the measurement error.

2.7.1 Drude Model

The Drude model is a simple, classical model to describe the motion of free carriers in metals and semiconductors [11, 80]. It treats electrons as a classical, non-interacting gas that scatter off the immobile ions in the lattice with a characteristic scattering time, τ. Each scattering event randomises the electron momentum and the electrons respond to the external electric and magnetic fields between scattering events. The equation of motion for the electrons is

$$\frac{d\mathbf{p}}{dt} = \mathbf{F} - \frac{\mathbf{p}}{\tau}, \tag{2.46}$$

where $\mathbf{p}$ is the momentum and $\mathbf{F}$ is the electromagnetic force. For charges driven by a THz electric field, the force is $\mathbf{F} = q\mathbf{E}_0 \exp(-i\omega t)$, where $q = 1.602 \times 10^{-19}$ C is the elementary charge and $\mathbf{E}_0$ is the incident electric field amplitude. Rewriting the momentum in terms of mass m and velocity $\mathbf{v}$ allows Equation 2.46 to be written as

$$m\frac{d\mathbf{v}}{dt} + \frac{m\mathbf{v}}{\tau} = q\mathbf{E}_0 \exp(-i\omega t). \tag{2.47}$$

We assume the electrons follow the oscillatory motion of the applied electric field

$$\mathbf{v} = \mathbf{v}_0 \exp(-i\omega t). \tag{2.48}$$

Substituting Equation 2.48 into Equation 2.47 and rearranging results in

$$\mathbf{v}_0 = \frac{q\mathbf{E}_0}{m\left(\frac{1}{\tau} - i\omega\right)}. \tag{2.49}$$

If the material has a density N of electrons, each moving with velocity $\mathbf{v}_0$ then the current density, $\mathbf{j}$ in the material is

$$\mathbf{j} = Nq\mathbf{v}_0 = \frac{Nq^2\mathbf{E}_0}{m\left(\frac{1}{\tau} - i\omega\right)}. \tag{2.50}$$

Conductivity is defined as $\mathbf{j} = \sigma\mathbf{E}$. Therefore, the Drude model conductivity, σ_D, is given by

$$\sigma_{\mathrm{D}}(\omega) = \frac{Nq^2\tau}{m^*(1 - i\omega\tau)}. \tag{2.51}$$

In a semiconductor, the free electrons are in the conduction band and have an effective mass, m^* determined by the band structure. Hence, the mass in Equation 2.51 uses the effective mass as this thesis is focussed on semiconductors. The scattering rate, γ, is the inverse of the scattering time τ. The mobility is another important material property that is defined as

$$\mu = \frac{q}{m^*\gamma}. \tag{2.52}$$

Figure 2.11 shows example Drude conductivity spectra for a range of scattering times. At low frequencies ($\omega\tau << 1$), the Drude conductivity is fully real and equals the DC conductivity, $\sigma_{\mathrm{DC}} = Nq^2\tau/m^*$. As the frequency increases, the real part decreases while the imaginary component increases until its peak at $\omega = \gamma$. At high frequencies ($\omega\tau >> 1$) the Drude conductivity is dominated by the imaginary component and the material behaves more like an insulator.

The Drude model has been highly successful at describing conductivity in bulk semiconductors, such as Si and GaAs [11]. However, many nanoscale materials, including nanowires and nanoparticles, exhibit a negative imaginary conductivity at low frequencies that the Drude model cannot explain. To properly describe charge transport in such materials, additional factors must be implemented into the Drude model.

2.7.2 Surface Plasmon Model

The surface plasmon model was developed by Nienhuys and Sündstrom to describe how small-scale structure impacts the conductivity spectrum of materials [81]. This model

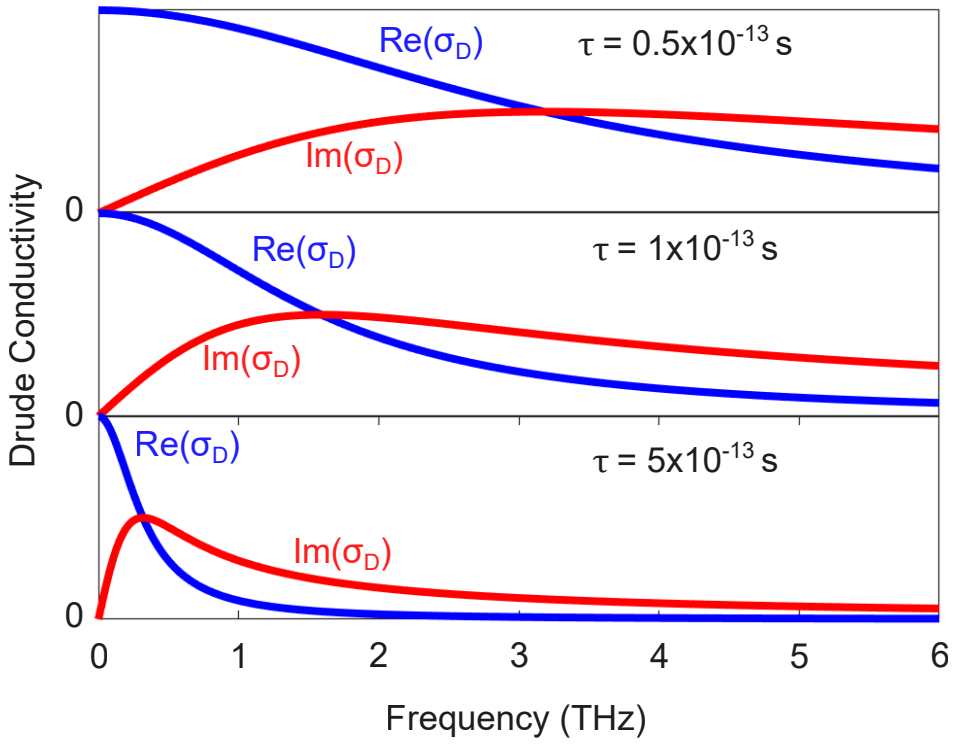

Figure 2.11: Example Drude conductivity spectra with different scattering times.

introduces an electrostatic restoring force to the Drude equation of motion. When an electric field is applied to the sample, such as the field from a THz pulse, the free electrons and holes are accelerated in opposite directions. When the dimensions of the sample are comparable to the THz wavelength, the charges accumulate at opposite ends of the sample structure, creating an electric dipole [78]. The electric field of this dipole opposes the external electric field, thus it is often referred to as a depolarisation field [82]. The depolarisation field acts as a restoring force on the charge carriers and causes them to undergo harmonic oscillations. Figure 2.12 depicts how a depolarisation field forms inside semiconductor nanowires when a THz electric field is applied.

Introducing the electrostatic restoring force means the charge-carrier equation of motion is that of a damped harmonic oscillator [81]

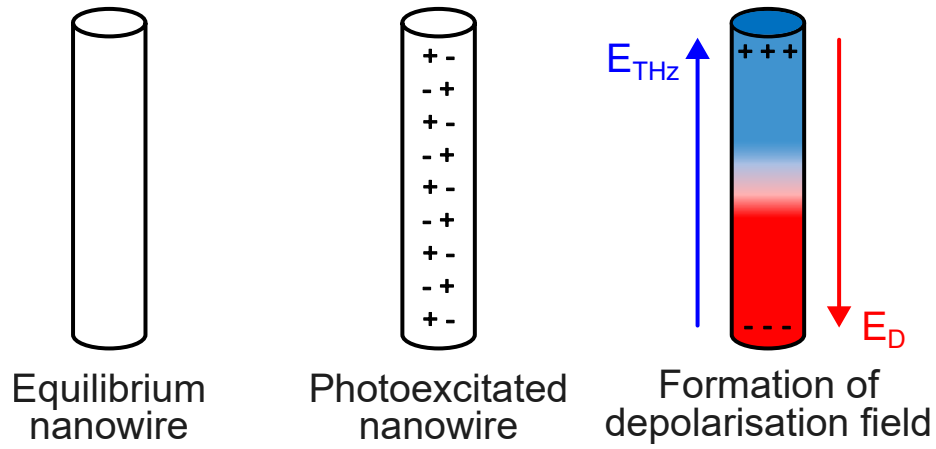

Figure 2.12: Schematic diagram of the formation of a depolarisation field in a semiconductor nanowire. At equilibrium there are no free carriers. After photoexcitation, electron-hole pairs (- and + symbols) are excited and available for conduction. The applied THz electric field, E_{THz}, accelerates the electrons and holes to opposite ends of the nanowire, forming a transient dipole that creates an opposing electric field – the depolarisation field, E_{D}.

$$m\frac{d^2\mathbf{x}}{dx^2} + m\frac{d\mathbf{x}}{dt} + m\omega_0^2\mathbf{x} = q\mathbf{E}_0\exp(-i\omega t), \tag{2.53}$$

where $\mathbf{x}$ is the carrier displacement from equilibrium and ω_0 is the resonant frequency of the oscillator. As in the previous section, the surface plasmon model conductivity, σ_{SD}, can be derived from the equation of motion

$$\sigma_{\mathrm{SP}}(\omega) = \frac{Nq^2}{m^*}\frac{i\omega}{\omega^2 - \omega_0^2 + i\omega\gamma}. \tag{2.54}$$

Equation 2.54 has the form of a Lorentzian. Figure 2.13 shows some example surface-plasmon conductivity spectra with different scattering times and resonant frequencies. In contrast to the Drude spectra, the surface plasmon model exhibits a resonance at $\omega = \omega_0$. The imaginary component of the conductivity is negative below the resonant frequency and both the real and imaginary components are zero at frequency zero. At frequencies higher than the resonance, the spectra follow the same lineshape as the Drude model. These features align very well with the conductivity spectra of nanowires and other nanostructures [83–88].

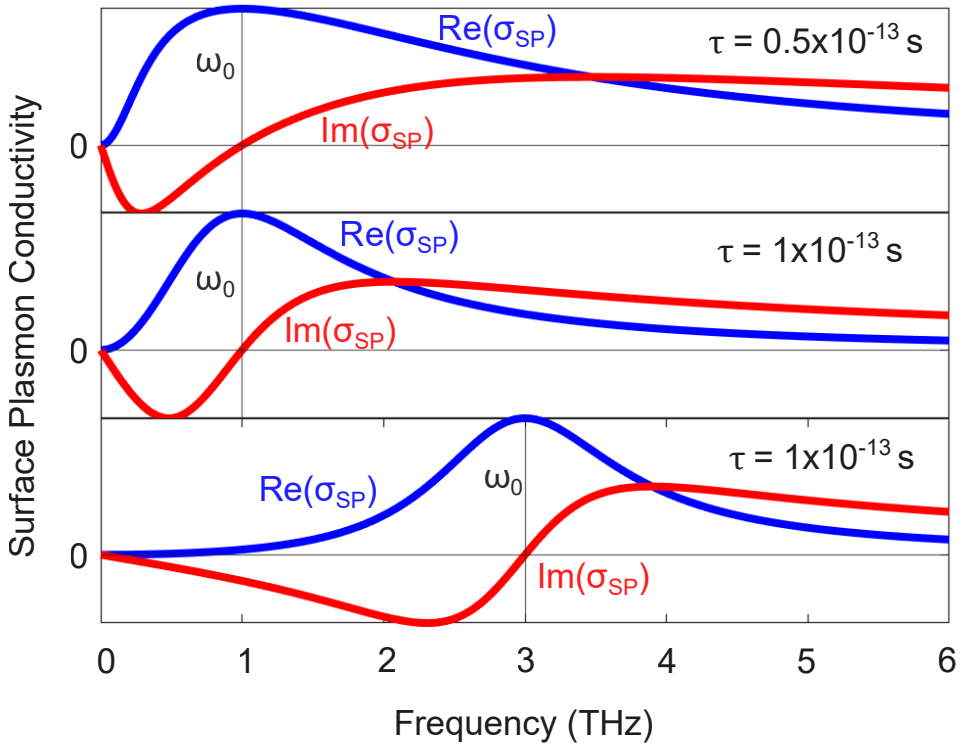

Figure 2.13: Example surface-plasmon conductivity spectra with different scattering times and resonant frequencies.

The charge-carrier mobility is related to the scattering time by Equation 2.52. The resonant frequency is related to the carrier density by

$$\omega_0^2 = g\frac{Nq^2}{m^*\epsilon_0} = g\omega_p^2, \tag{2.55}$$

where g is a factor dependent on the sample geometry and dielectric properties, and ω_p is the plasma frequency. Equation 2.55 states that the resonant frequency scales as the square root of the carrier density – a key signature of plasmons.

Aside: Drude-Smith Model

Other models exist that can replicate the negative imaginary conductivity observed in nanostructures. One commonly used approach is the Drude-Smith model, which is a phenomenological extension of the Drude model [89, 90]. This model accounts

for preferential scattering by introducing a parameter, c_p, that is the fraction of the initial carrier velocity that is retained after scattering event p. For $c_p > 0$, the carriers preferentially scatter forwards, $c_p = 0$ indicates isotropic scattering and simplifies to the Drude model, and $c_p < 0$ means carriers are preferentially scattered backwards – for example from the boundary of a nanoparticle or grain. The conductivity is expressed as

$$\sigma_{\mathrm{DS}}(\omega) = \frac{Nq^2}{m^*} \frac{\tau}{1 - i\omega\tau} \left[1 + \sum_{p=1}^{\infty} \frac{c_p}{(1 - i\omega\tau)^p} \right]. \tag{2.56}$$

The infinite summation in Equation 2.56 is typically simplified to only include the first scattering term $p = 1$. The Drude-Smith model can replicate the negative imaginary conductivity in nanostructures, and is equivalent to the surface plasmon model when $c_1 = -1$, $\gamma_{\mathrm{DS}} = \gamma_{\mathrm{SP}}/2$, and $\omega_0 = \gamma_{\mathrm{DS}}$, where the subscripts $_{\mathrm{DS}}$ and $_{\mathrm{SP}}$ specify the Drude-Smith and surface plasmon parameters respectively [11]. However, unlike the surface plasmon model, the Drude-Smith model cannot explain the changing resonant frequency with increasing carrier density that is observed in nanowires [85] (Equation 2.55). Furthermore, the physical reasoning for ignoring scattering events beyond the first term is not well justified. Therefore, this thesis employs the surface plasmon model to describe carrier dynamics of nanostructured materials instead of Drude-Smith.

3

Optimised Spintronic Terahertz Emitters for Time-Domain Spectroscopy

3.1 Introduction

Spintronic THz emitters (STEs) have emerged as high-power, broadband sources of THz radiation for time-domain spectroscopy [7, 8, 40, 48, 51, 91]. One of the most efficient STE designs is the trilayer structure of a ferromagnetic material sandwiched between two different non-ferromagnetic materials: NM1|FM|NM2. Notably, W|$Co_{40}Fe_{40}B_{20}$|Pt STEs have demonstrated broadband emission from 0.1 to 30 THz with similar or greater electric field amplitudes than conventional THz sources, such as biased photoconductive antennas and electro-optic crystals [7]. The compact geometry and ability to drive the STE with wavelengths between 800 and 1550 nm [50, 92] make STEs highly versatile and compatible with many existing THz-TDS systems.

Optimal THz emission occurs when the STE layers are extremely thin ($\lesssim$ 2 nm each), which restricts how much of the THz-generation pulse is absorbed by the STE. As a result, a significant proportion (>20%) of the femtosecond laser pulse transmits through the

STE [50, 52]. This transmitted light can introduce artefacts by photoexciting the sample under investigation or damaging the detection elements of the spectrometer. Therefore, it is essential to sufficiently attenuate the transmitted beam. One approach to mitigating this problem is to place thin polymer films, such as cellulose nitrate (CN), behind the STE to scatter the transmitted THz-generation beam while allowing the THz radiation to transmit. While effective, this method adds complexity to the experimental setup and can also attenuate or distort the THz radiation.

An alternative method of controlling the transmitted excitation beam is to utilise the light to enhance the THz emission. For example, Feng *et al.* [49] developed an STE with a photonic crystal structure, such that the excitation pulse traverses multiple NM1|FM|NM2 trilayers, reducing the transmission through the full STE structure and enhancing the emitted THz electric field strength. Herapath *et al.* [50] demonstrated a different approach by constructing a dielectric cavity adjacent to the STE that increased absorption of the excitation pulse, leading to an increase in THz emission. This approach was recently extended by Rouzegar *et al.* [51] by coupling the dielectric cavity with a Si substrate that removes heat more efficiently from the STE and enables a greater proportion of the THz radiation to be emitted in the forward direction. However, these approaches are designed to focus on enhancing the emitted THz electric field strength, instead of minimising transmission of the excitation beam.

In this chapter, the issue of transmitted light is addressed by integrating an STE with a broadband high-reflectivity (HR) coating optimised for 800 nm excitation. Both the design and characterisation of the HR coating are presented to demonstrate that it suppresses over 99.9% of the THz-generation beam. This level of attenuation is comparable to placing 0.1 mm of CN behind the STE, thus the HR coating effectively removes the need for additional attenuators. Moreover, the presence of the HR coating significantly enhances the emitted THZ electric field strength by increasing the intensity

of the THz-generation beam inside the STE layers. The field enhancement is improved further by combining the HR coating with an anti-reflective (AR) coating on the opposite side of the STE. These AR+HR-coated STEs are optimised for THz spectroscopy and form an essential part of the experiments in the remaining chapters of this thesis. This chapter is an adaptation of my work published in Ref. [52].

3.2 Coating Design and Fabrication

A schematic diagram of the AR+HR-coated emitter along with the coating structures is presented in Figure 3.1 (a). This chapter characterises the performance of the AR+HR-coated emitter and compares it to an HR-coated emitter and an uncoated emitter, all of which are illustrated in Figure 3.1 (b). The STE consists of W (1.9 nm)|$Co_{40}Fe_{40}B_{20}$ (2.0 nm)|Pt (1.9 nm), and matches the optimised structures reported in [7]. The STE materials were DC-sputtered in Ar background gas onto a 1-mm-thick, 25-mm-diameter c-cut sapphire substrate using a sputter tool (Rotaris, Singulus Technologies, Germany). Sapphire was selected for the substrate material owing to its relatively high thermal conductivity ($\sim$30 $Wm^{-1}K^{-1}$) [93]. The substrate helps dissipate heat away from the metallic STE layers after laser excitation. Thus, the greater the thermal conductivity of the substrate, the greater laser power that can be applied, leading to increased THz generation before the STE reaches its damage threshold. STE fabrication was done by Joel Cramer at Johannes Gutenberg University in Germany.

The AR and HR coatings were fabricated from alternating layers of Ta_2O_5 and SiO_2 deposited by ion-beam sputtering (Navigator, Cutting Edge Coatings, Germany). Specifically, the AR coating consisted of a 155.5-nm-thick layer of SiO_2 on a 44.5-nm-thick layer of Ta_2O_5 deposited directly on the sapphire substrate. The HR coating was deposited onto the Pt layer of the STE and consisted of 22 layers to sufficiently reduce the THz-generation beam transmission. A 30-nm layer of Ta_2O_5 was in contact with

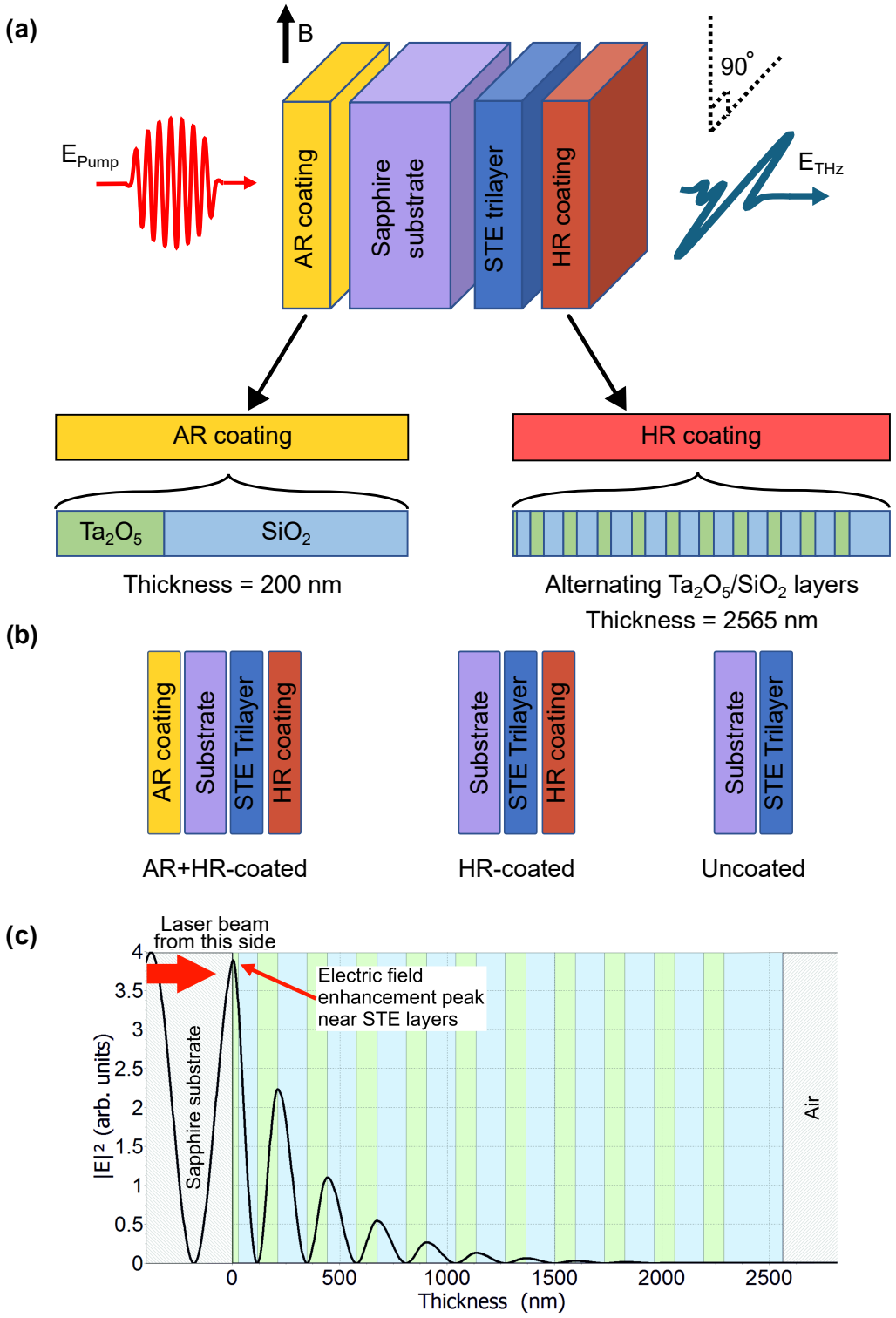

Figure 3.1: (a) Schematic diagram of the STE with AR and HR coatings along with the layer structure of both coatings. (b) Schematic diagrams of the three emitter structures investigated in this work. (c) [Figure produced by Dr. Simas Melnikas] Electric field profile of the excitation pulse (E_{Pump}) through the HR coating. The peak electric field is at the boundary between the substrate and HR coating – exactly the position of the STE trilayer. Hence, the coating design maximises the absorption of the THz-generation pulse by the STE. Almost none of the incident field transmits through the HR coating into air.

the Pt, with 88 nm of SiO_2 on top, followed by nine pairs of 95-nm-thick Ta_2O_5 and 136-nm-thick SiO_2. The coating was completed with a 95-nm-thick layer of Ta_2O_5 and 272-nm-thick layer of SiO_2. Figure 3.1 (c) shows the simulated electric field profile of the excitation laser in the HR coating. The peak electric field is near the STE metallic layers, which allowed for maximum absorption of the laser energy into the STE. Both the AR and HR coatings were optimised for 800-nm wavelength light at normal incidence, making them well-suited for operation with Ti:sapphire lasers. The coating layer thicknesses can be adjusted to optimise for different excitation wavelengths [94]. Dr. Simas Melnikas designed and deposited the HR and AR coatings to the STEs and simulated the electric field enhancement (Figure 3.1 (c)) at the Center for Physical Sciences and Technology in Lithuania.

The AR and HR coatings operate using the principle of interference between their different layers. Greater reflection/transmission is achieved by choosing materials with a large contrast in their refractive index [95]. SiO_2 is the material with the lowest refractive index ($\sim$ 1.45 at 800 nm [96]) that can be deposited in a standard configuration ion-beam sputtering coating plant. Hence, SiO_2 was selected as the low-refractive-index material in the coatings to ensure the highest contrast between the refractive indices of the deposited layers. Ta_2O_5 was chosen as the high-refractive-index material because it has a relatively large refractive index in the visible to near-IR spectral range ($\sim$ 2.1 at 800 nm), and features a higher laser induced damage threshold than alternative materials like Nb_2O_5 or TiO_2 [97]. Furthermore, Ta_2O_5 was found to adhere well to the Pt layer of the STE during development, making it highly compatible with the emitters.

3.3 Experimental Methods

3.3.1 THz Time-Domain Spectroscopy

THz-TDS was employed to characterise the THz emission from the coated STEs, and to demonstrate their suitability for dark conductivity (i.e. at equilibrium without photoexcitation) measurements. A diagram of the THz spectrometer is presented in Figure 2.2. In this study, only THz-TDS was needed and so the optical-pump beam was blocked. The THz-generation beam was directed at normal incidence onto the STE. The beam had a Gaussian profile with a FWHM (full-width half-maximum) of ∼0.9 mm and excited the emitter with a fluence of ∼15 mJcm^{-2}. An external pair of neodymium magnets provided an effective magnetic field of ∼ 20 mT at the centre of the STE, with the magnetic field direction parallel to the STE surface, as shown in Figure 3.1 (a). The emitted pulses of THz radiation were detected by electro-optic sampling using a 200-μm-thick (110) GaP crystal optically contacted to a 4-mm-thick (100) GaP crystal. THz generation and detection occurred under a vacuum of 10^{-2} mbar.

3.3.2 Fourier-Transform Infrared Spectroscopy

Fourier-transform infrared (FTIR) spectroscopy with a Bruker Vertex 80v spectrometer was used to characterise the optical transmission of the AR and HR coatings around the target wavelength of 800 nm. In FTIR spectroscopy, light from a broadband source (here, a tungsten–halogen lamp) is first directed into a Michelson interferometer, where the beam is split into two arms with different optical path lengths, recombined, and sent to the sample. The recombined beam carries a modulated interferogram that encodes information from all wavelengths of the source. This light is transmitted through the sample at a small angle of incidence (∼11°) to suppress any back-reflection artefacts. The transmitted beam is collected by a detector (silicon diode). By Fourier-transforming the detected interferogram, the transmission intensity as a function of wavelength can be extracted.

3.4 Results and Discussion

3.4.1 Optical Properties

Figure 3.2 (a) shows the optical transmission spectra through the STE with different coating arrangements, along with the transmission through a 0.1-mm-thick CN film. Without coatings, the STE transmitted roughly 31% of the light between 600 and 1000 nm, which is consistent with the relatively flat transmission reported previously in this wavelength range [7, 50]. The HR-coated and AR+HR-coated emitters exhibited very similar transmission spectra, with both coating arrangements allowing less than 1% of light through between 720 and 880 nm. As highlighted in the inset, emitters with the HR coating transmit $\sim 0.05\%$ of light at 800 nm, which is nearly identical to the transmission through the 0.1-mm-thick CN. Hence, the HR coating sufficiently suppresses the transmission of 800 nm light for use in THz spectroscopy.

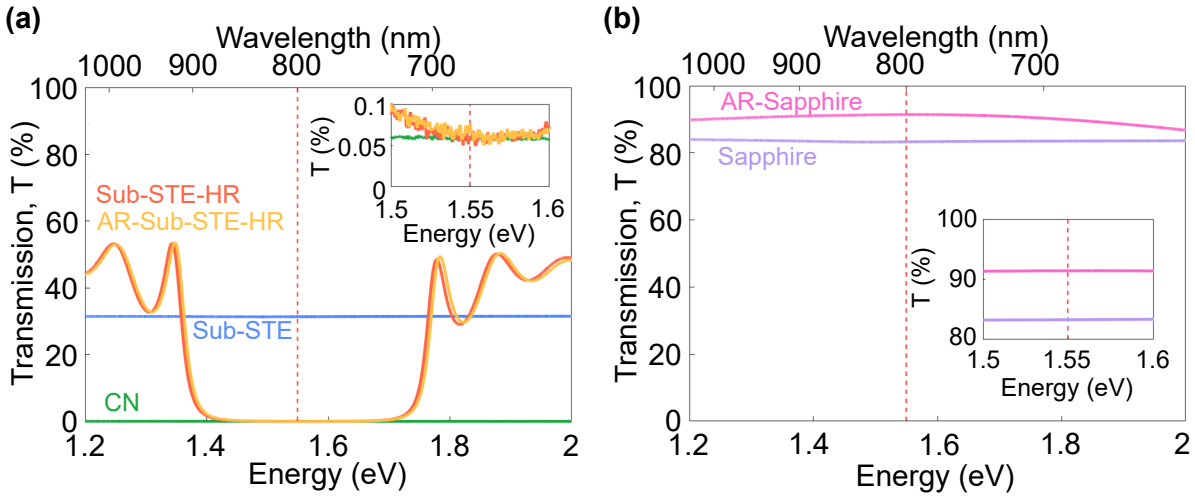

Figure 3.2: Optical transmission spectra of coated spintronic THz emitters measured by FTIR spectroscopy. (a) Transmission through a 0.1-mm-thick cellulose nitrate (CN) film and through an uncoated, HR-coated, and AR+HR-coated W|$Co_{40}Fe_{40}B_{20}$|Pt STE. The labels on the figure describe the sample structure, with the light entering the left-most material and exiting the right-most. (b) Transmission through a bare, 1-mm-thick c-sapphire substrate and an AR-coated sapphire substrate. The red-dashed line highlights the target wavelength of 800 nm. The insets zoom on the spectra near the target wavelength.

Figure 3.2 (b) shows the transmission through the 1-mm-thick c-sapphire substrate

with and without an AR coating. The AR-coated sapphire allowed approximately 8% more 800-nm wavelength light through than the bare sapphire. This value is very similar to the ∼7.5% Fresnel reflection of unpolarised light at normal incidence upon a single vacuum-sapphire interface ($R = |(n-1)/(n+1)|^2, n \sim 1.75$ [98]). This result indicates that the AR coating succeeds in allowing the maximum amount of the target wavelength to enter the substrate, and thus enhances the fraction of the THz-generation beam that reaches the metallic STE layers for conversion to THz radiation.

To confirm that the 800-nm laser light is effectively blocked by the HR coating, the average power of 800-nm femtosecond laser pulses was measured directly before and after STEs with different coating arrangements using a power meter (Coherent LM2 VIS). Table 3.1 summarises the power measurements and calculated transmission. Note that for these measurements, the incident laser power on the emitters was attenuated by a factor of 100 using neutral density filters placed directly before the STE. The attenuation was necessary to ensure the excitation beam power was within a highly linear range of the power meter. The power transmission values in Table 3.1 are very similar to the 800 nm transmission values in Figure 3.2 (a), which emphasises the effectiveness of the HR coating to block the transmission of 800-nm light.

	Sub-STE	Sub-STE-HR	AR-Sub-STE-HR
Power before emitter	10.5 ± 0.2 mW	10.5 ± 0.2 mW	10.5 ± 0.2 mW
Power after emitter	3.7 ± 0.2 mW	6.8 ± 0.4 μW	7.6 ± 0.4 μW
Transmission	35 ± 3%	0.065 ± 0.005%	0.072 ± 0.005%

Table 3.1: Average power measurements of 35-fs laser pulses (800-nm centre wavelength, 5-kHz repetition rate) before and after STEs with different coatings. The laser power was attenuated by a factor of 100 by neutral density filters before reaching the STEs to ensure the incident power was within a highly linear range of the power meter.

3.4.2 Enhancement of THz Emission

The emission of THz radiation from an uncoated, HR-coated, and AR+HR-coated STE was measured by THz-TDS. As discussed in Section 3.4.1, the uncoated emitter transmits

over 30% of incident light. Therefore, to prevent damage to the detection optics, it was necessary to attenuate the transmitted beam with a 0.1-mm-thick CN film placed directly behind the STE. The same CN film was also positioned behind the HR and AR+HR-coated emitters to ensure the experimental conditions were identical for all STEs. The effect of the CN film on the THz emission is discussed further in Section 3.4.5.

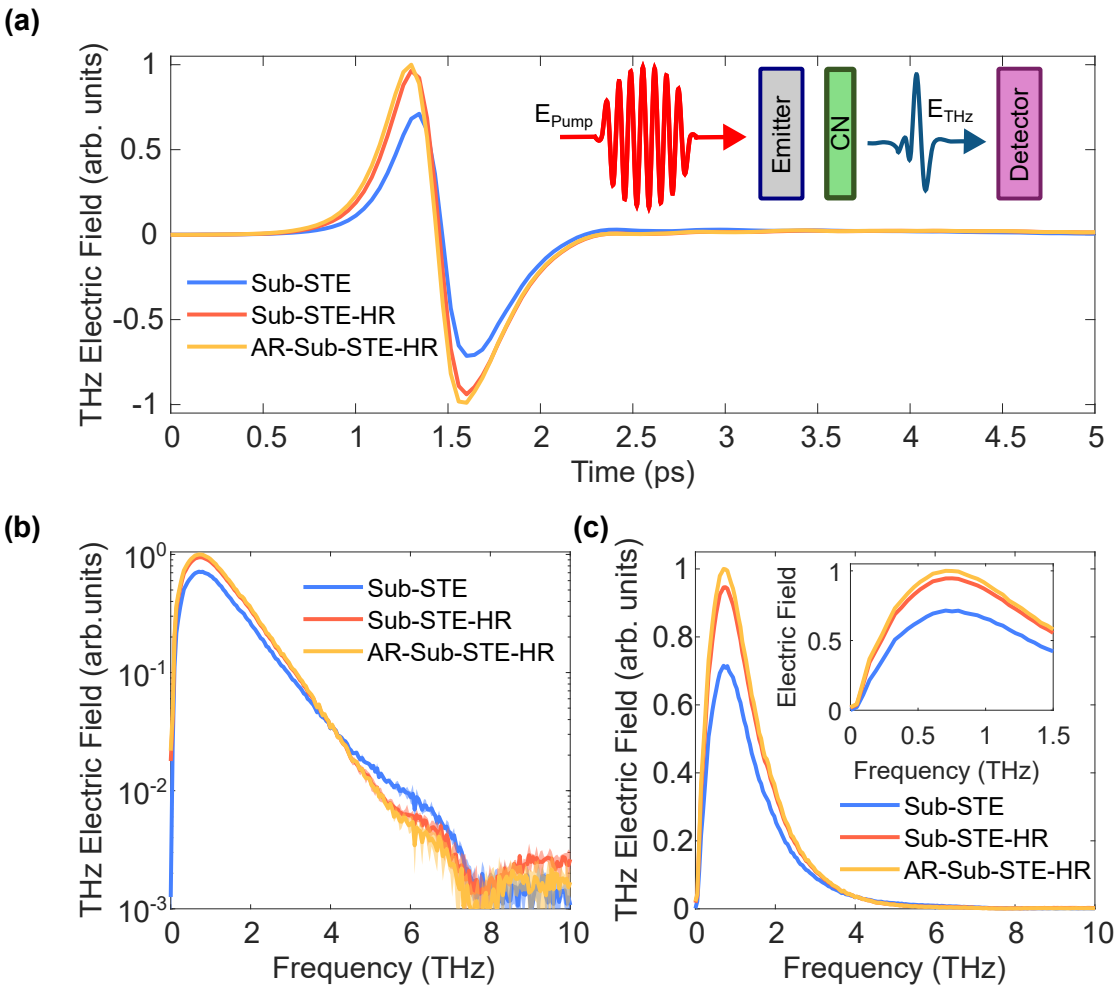

Figure 3.3: THz emission from W|$Co_{40}Fe_{40}B_{20}$|Pt STEs with different coatings measured using a 200-μm-thick GaP detector via electro-optic sampling. (a) THz electric field in the time domain. The inset shows a schematic of the experiment geometry, with a 0.1-mm-thick CN film used to attenuate the transmitted laser beam (E_{pump}). (b,c) Emitted THz electric field in the frequency domain (Fourier transform of (a)) on a logarithmic and linear scale respectively. The inset in (c) highlights the peak amplitude of the THz emission. Solid lines are the average of three repeated scans, while the semi-transparent surrounding regions show the standard deviation between measurements. Note that the standard deviation was very small and is mainly observed at frequencies above ~6 THz at this scale. Additionally, the spectral intensity of the emitters is convolved with the GaP detector response in the spectra of (b) and (c).

Figure 3.3 (a) shows the THz electric field generated by each emitter in the time domain. The HR coating increased the electric field amplitude by 35% compared to the uncoated emitter. This enhancement of the THz electric field arises from the design of the HR coating, which maximises the electric field of the THz-generation pulse at the STE metallic trilayer (see Figure 3.1 (b)), thereby maximising absorption of the laser pulse and increasing the intensity of the THz emission [49, 50, 52]. A further 4% enhancement (net 40% increase compared to the uncoated emitter) in field amplitude was observed for emission from the AR+HR-coated emitter compared to the HR-coated emitter. This additional field amplitude is a result of the AR coating allowing greater transmission of the THz-generation pulse into the substrate, and thus more of the excitation light reaches the STE layers for absorption, increasing THz generation. This 40% increase in emitted field strength is less than reported for other methods [49, 50], however the design of the HR coating is focussed on eliminating the need for further attenuation of the transmitted excitation beam, whereas other studies aimed to maximise THz generation.

Figure 3.3 (b) and (c) show the emitted THz electric field in the frequency domain on a logarithmic and linear scale respectively. The emitted spectra have approximately the same shape from 0–2 THz, with an average 35% (42%) greater signal from the HR-coated (AR+HR-coated) emitter compared to the uncoated emitter. Interestingly, the uncoated emitter generated similar or slightly more THz field strength from 4–7 THz compared to the coated emitters. This effect can also be seen in the time-domain figure, with the coated emitters generating THz pulses that are slightly broader than pulses from the uncoated emitter. It is important to note that the presented spectra are a convolution of the emitted THz electric field and the GaP detector response function [99]. As a result, the detected THz electric field drops sharply near 8 THz as the GaP response function dips near 8 THz [99, 100]. A different detection crystal with a larger response

function at higher frequencies, such as organic polymers [101], would reveal that the emitted THz bandwidth is limited by the excitation pulse duration [7].

The drop in the high-frequency performance of the coated emitters compared to uncoated emitters likely arises from the absorption coefficient of Ta_2O_5 increasing at higher THz frequencies [102]. Further improvement in the high-frequency emitter performance is expected if an alternative material with less THz absorption than Ta_2O_5 is utilised. Another potential cause of the reduced bandwidth from coated emitters is the extra layers of the coatings introducing some dispersion to the THz pulse, broadening it in the time domain and thus slightly reducing the bandwidth [103]. Despite the slight loss of high-frequency signal, the HR coating significantly increases the emitted THz electric field strength below 4 THz, which is often where the most interesting features in the AC conductivity spectra of inorganic semiconductors occur.

3.4.3 STE Spatial Dependence on THz Emission

To further probe the STEs and their coatings, additional measurements were performed in which the THz-generation beam was deliberately positioned at different locations across the emitter surface. The aim was to determine whether local excitation of specific regions yielded variation in the THz emission, which would indicate defects in the trilayers or coatings.

Figure 3.4 (a) show the time-domain THz electric field emitted by an HR-coated STE when the femtosecond laser illuminated different positions on the emitter. The pulse shape was nearly identical for all excitation positions, and the peak amplitude was constant within ∼3%. The THz frequency spectra in Figure 3.4 (b) and (c) are also nearly identical for all excitation spot positions, with the amplitudes varying by less than 3%. The negligible variation strongly suggests that the deposition process has created a highly uniform coating on the STE with no hot spots. This uniformity is promising for

applying the coatings to larger area devices. Furthermore, it enables a large excitation spot size to be used on the STE, spreading out any heat accumulation and allowing higher input power to be used, resulting in greater THz generation [48].

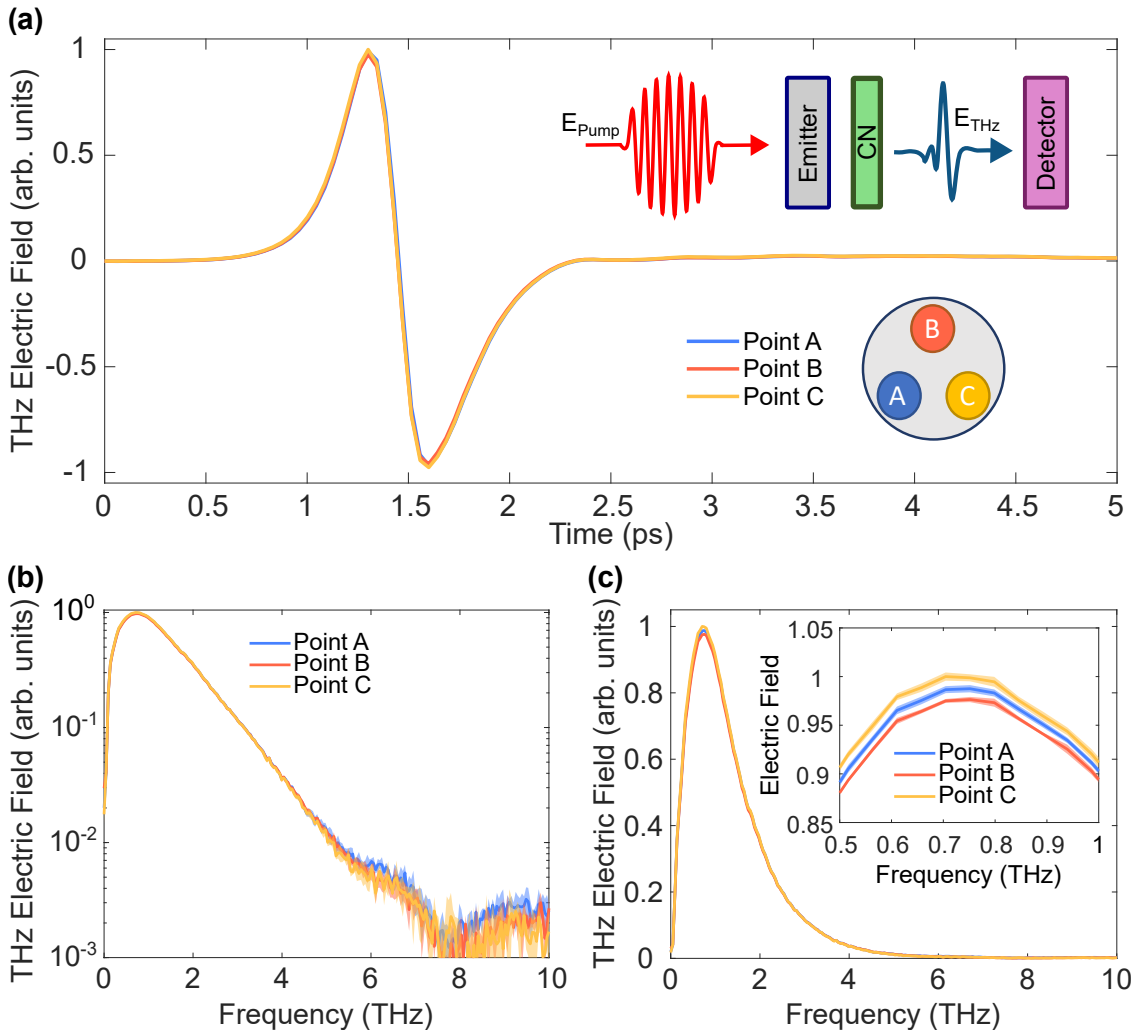

Figure 3.4: THz emission an HR-coated STE when different locations on the emitter surface are excited. (a) THz electric field in the time domain. The top inset shows a schematic of the experiment geometry. The bottom inset shows the relative positions of the THz-generation beam on the emitter. (b,c) Emitted THz electric field in the frequency domain (Fourier transform of (a)) on a logarithmic and linear scale respectively. The inset in (c) highlights the peak amplitude of the THz emission. Solid lines are the average of three repeated scans, while the semi-transparent surrounding regions show the standard deviation between measurements. Note that the spectral intensity of the emitters is convolved with the GaP detector response in the spectra of (b) and (c).

3.4.4 THz Time-Domain Spectroscopy of GaAs

A powerful application of THz-TDS is to measure the intrinsic properties of a material, such as the complex refractive index. It is important that the sample is not photoexcited during such measurements, as any photoexcitation can significantly alter the dielectric response of the sample. Therefore, careful control of the light transmitted through the THz emitter is essential for accurate THz-TDS measurements. To demonstrate the effectiveness of the HR coating for eliminating this transmitted light, the refractive index and equilibrium conductivity of a 2.96 ± 0.01-mm-thick, semi-insulating GaAs wafer was measured by THz-TDS using coated and uncoated STEs. Unlike the measurements in Sections 3.4.2 and 3.4.3, no CN film was placed behind the emitters unless explicitly stated.

The GaAs is too thick to apply thin-film approximations, so the method described in Section 2.6.4 was required to extract the complex refractive of the GaAs. Briefly, the THz transmission function takes the form of Equation 2.42, and the refractive index can be solved numerically by minimising the error function between the experimentally determined transmission and Equation 2.42 [71, 79]. Figure 3.5 (a) shows the error function surface over a range of different complex refractive index values for GaAs (measured with an HR-coated STE). The surface has a minimum near $\tilde{n} = 3.6 + 0.0015i$, as shown clearly in the contours in Figure 3.5 (b), agreeing well with literature values of the refractive index of GaAs [104]. Note that the surface must be calculated for each frequency in the THz spectrum to extract the full frequency dependent refractive index.

After extracting the complex refractive index from THz-TDS, it was converted to the complex conductivity using Equation 2.16, with $\tilde{\epsilon} = \tilde{n}^2$ and $\epsilon_L = \epsilon_s = 13$ [105]. Figure 3.6 (a) and (b) show the real and imaginary components of the conductivity respectively. For all emitters, the real conductivity exhibited a small feature near 0.7 THz and a much larger peak near 2.4 THz. Both of these features have been previously reported and are attributed to multiphonon processes [104, 106, 107]. The real conductivity tends

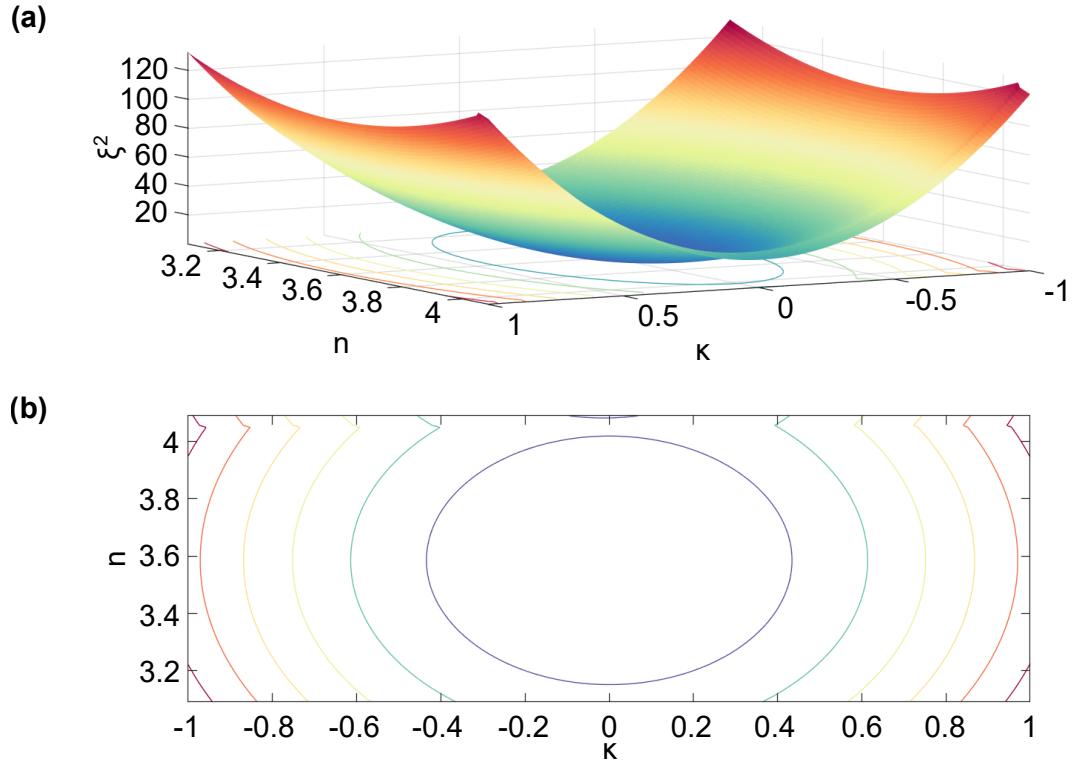

Figure 3.5: Error Function, ξ^2, Equation 2.43, of the theoretical THz transmission against the experimentally determined transmission. (a) Surface of error function values at different refractive index values. (b) Contours of the error function showing the minimum near $\tilde{n} = 3.6 + 0.0015i$.

to increase with frequency, whereas the imaginary component tends to decrease. These observations are consistent with the background conductivity arising from the TO phonon mode of GaAs near 8 THz [108]. Equation 2.17 describes the effect of the TO phonon on the permittivity, which can be converted to conductivity using Equation 2.16. Figure 3.6 (a) and (b) show the real and imaginary conductivity contributions from the TO phonon, and the inset of (b) displays the full TO phonon conductivity.

The measured real conductivity of GaAs is nearly identical when measured with the HR, AR+HR, and uncoated+CN STE configurations. In contrast, the uncoated emitter without CN resulted in a significantly higher real conductivity from 0.5–2.2 THz. This higher conductivity can be explained as follows: the bandgap of GaAs (1.41 eV [109]) is

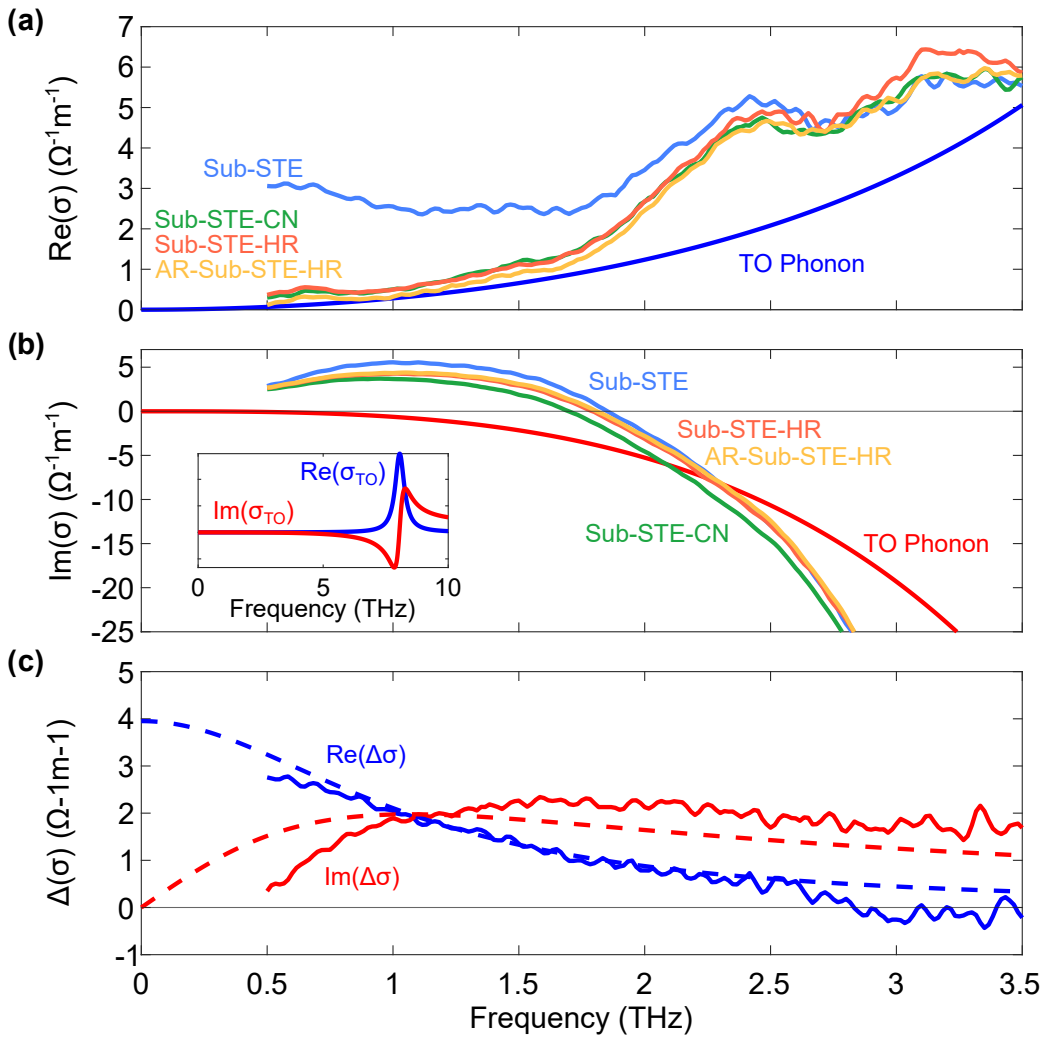

Figure 3.6: (a,b) Real and imaginary components of the conductivity of GaAs extracted from THz-TDS using W|$Co_{40}Fe_{40}B_{20}$|Pt STEs with different coatings. The background conductivity from the TO phonon was calculated using Equation 2.17 and scaled by a factor of 20 for comparison to the experimental data. The inset in (b) shows the real and imaginary components of the TO phonon conductivity. (c) Photoconductivity of GaAs resulting from transmission of 800-nm light through the uncoated STE. The photoconductivity was calculated as the difference in conductivity when using the uncoated emitter with and without a CN film behind it. The dashed lines are a fit to the Drude model (Equation 2.51).

less than the energy of the 800-nm excitation laser (1.55 eV), hence any 800-nm light transmitted through the emitter will photoexcite electron-hole pairs in the GaAs. As roughly 30% of the THz-generation pulse transmits through the uncoated emitter, the GaAs will be photoexcited by this transmitted light and the conductivity will rise. On the other hand, less than 0.1% of the 800-nm laser transmits through the HR-coated

emitters and the CN, hence the GaAs experiences negligible photoexcitation with these emitter configurations and the true equilibrium conductivity is recovered.

To further demonstrate the photoexcitation resulting from the excess transmitted 800-nm light, Figure 3.6 (c) shows the difference in conductivity measured when the uncoated emitter does and does not have CN behind it. The dashed lines in the figure show a simple Drude model fit (Equation 2.51) to the data, which agrees reasonably well with the experimental data across the mid-to-high frequency range. Previous studies have shown that the Drude model is an excellent fit to the photoconductivity of bulk GaAs [110], hence the observed difference in conductivity between the uncoated emitter without CN and the other emitters can be attributed to photoexcitation of the GaAs by the transmitted 800-nm laser pulse. However, a significant deviation between the model and experimental data at frequencies below ∼1 THz. This deviation arises because the various frequency components of the THz beam focus on the sample to different, diffraction-limited sizes, whereas the transmitted 800-nm light has a fixed FWHM of ∼0.9 mm (assuming a similar size at the emitter and sample positions). Consequently, at lower THz frequencies where the THz spot is larger than the transmitted beam, the THz beam probes both the photoexcited region and the surrounding dark GaAs. This spatial averaging over a non-uniform charge-carrier distribution causes the observed breakdown of the Drude model fit at the low-frequency end of the spectrum [19].

These conductivity results demonstrate the importance of controlling the transmission of the THz-generation beam through the STE for THz-TDS. Furthermore, it shows that the HR coating effectively blocks the 800-nm light and prevents sample photoexcitation, allowing for accurate determination of the intrinsic material properties.

3.4.5 Effect of Cellulose Nitrate

The HR coating makes the CN film redundant, so it is useful to understand the effect of removing this film on the THz signal. Figure 3.7 (a) shows the detected THz electric field from an HR-coated emitter with and without a 0.1-mm-thick CN film directly behind the emitter. The THz pulse has a slightly greater amplitude when no CN is behind the emitter. The corresponding emitted THz spectra are shown in Figure 3.7 (b). The spectral profile is very similar with and without CN, however the electric field is ∼10% weaker on average from 0–6 THz when the CN is present. These results indicate that the CN weakly absorbs in the THz frequency range. To quantify this absorption, the absorption coefficient, α, was calculated by

$$\alpha(\omega) = -\frac{1}{l_{\mathrm{CN}}} \ln\left(\frac{I_{\mathrm{CN}}(\omega)}{I_{\mathrm{vac}}(\omega)}\right), \tag{3.1}$$

where $I_{\mathrm{CN}}(\omega)$ and $I_{\mathrm{vac}}(\omega)$ are the THz electric field intensities through vacuum and CN respectively, and l_{CN} is the thickness of the CN film.

The absorption coefficient is plotted in Figure 3.7 (c). At frequencies below 1 THz, the absorption coefficient is relatively small, but increases with frequency. Upon comparison of the CN results in Figure 3.7 and the coated emitter results in Figure 3.3, it is clear that the HR coating is preferable to CN, as the HR coating enhances the THz electric field while attenuating transmission of the THz-generation pulse to the same degree that the CN does, whereas the CN weakly absorbs and reduces the THz electric field intensity. Additionally, the HR coating acts as a robust protective layer on the STE that should make the emitter more resistant to chemical and mechanical damage while being easy to clean. In the case of surface scratches on the coating, only a small fraction of the incident laser pulse should be scattered and the THz conversion efficiency should remain unchanged.

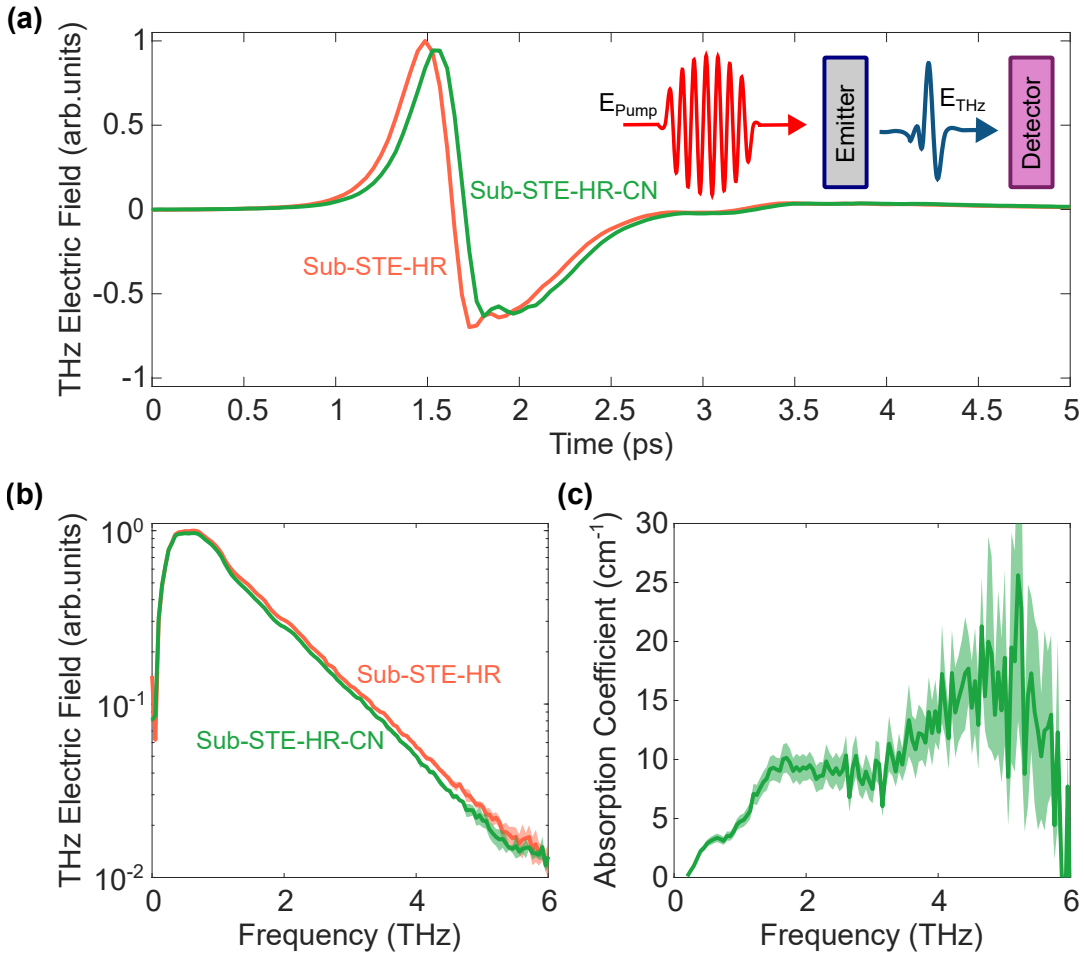

Figure 3.7: THz emission from an HR-coated W|$Co_{40}Fe_{40}B_{20}$|Pt STE with and without 0.1 mm of CN behind it. (a) THz electric field in the time domain. The inset shows a schematic diagram of the experiment geometry. (b) Corresponding THz electric field in the frequency domain on a logarithmic scale. (c) Absorption coefficient of CN as calculated by Equation 3.1 The solid lines are the average of three scans, while the semi-transparent surrounding regions show the standard deviation between measurements. Note that the spectral intensity of the emitters is convolved with the GaP detector response in the spectra of (b).

3.5 Conclusion

In this chapter, the performance of W|$Co_{40}Fe_{40}Co_{20}$|Pt trilayer STEs with AR and HR coatings optimised for 800-nm light has been studied. The inclusion of the HR coating reduces transmission of 800-nm light through the STE to less than 0.1%, matching the attenuation achieved by a 0.1-mm-thick cellulose nitrate film. Hence, the HR coating removes the need for additional attenuating elements and eliminates their associated

drawbacks, such as absorption of the emitted THz radiation. Moreover, the HR-coated emitters generated THz electric field amplitudes that were approximately 35% greater than from an uncoated emitter. The addition of an AR coating further enhanced the emitted THz electric field strength, resulting in a net ∼40% increase compared to an uncoated STE.

The coated emitter performance was slightly diminished above ∼4 THz, likely owing to absorption in the Ta_2O_5 layers of the HR coating. Future emitter designs could be improved at these higher frequencies by replacing the Ta_2O_5 with an alternative high-index dielectric with less absorption in the THz frequency range. Additionally, further thought could be given to the substrate material to improve the thermal conductivity and promote forward-propagation of the emitted THz radiation, as explored in Ref. [51].

Beyond technical performance, the coated STEs prove highly practical: by markedly reducing laser transmission through the STE, they prevent unwanted photoexcitation of the sample, enabling accurate determination of intrinsic material properties – such as dark conductivity and refractive index – in THz-TDS measurements. Additionally, while the AR and HR coatings were optimised for the 800-nm light from Ti:sapphire lasers, the coatings can be tuned for other excitation wavelengths, making them ideal for a range of THz systems and applications.

The AR+HR-coated emitters developed and characterised in this chapter form an essential part of experiments in the upcoming experimental chapters. The emitters prevent unwanted photoexcitation while enhancing the THz electric field strength. These improvements strengthen the reliability and sensitivity of THz spectroscopy results throughout the rest of the dissertation. In particular, the following chapter leverages the increased THz SNR to investigate semiconductor nanostructures, which typically have significantly weaker responses than their bulk counterparts. Thus, the emitter advancements introduced here enable the subsequent experimental results.

4

Influence of Subwavelength Geometry on Extracting the Electrical Properties of Semiconductors by Terahertz Spectroscopy

4.1 Introduction

The miniaturisation of semiconductors has driven improvements in technology and enabled access to new phenomena at the micro- and nanoscales. For example, semiconductor nanowires pair excellent charge transport properties with nanoscale dimensions, making them promising candidates as the building blocks of future optoelectronics [11, 62, 74, 111, 112], while semiconductor metasurfaces utilise nanostructures for the tunable manipulation of light [113–116]. Other emerging material systems – such as metal-halide perovskite semiconductors – form nanoscale grains, with studies showing that larger grains lead to improved charge transport owing to reduced charge-carrier scattering at grain boundaries [117–119].

Optimisation of structured semiconductor devices requires a robust understanding of

their intrinsic charge-carrier dynamics. However, the micro/nanoscale of such structures make conventional characterisation techniques difficult and impractical to conduct. For example, Hall effect measurements, a foundational technique for characterisation of electrical properties in the semiconductor industry [120], require electrical contacts to be fabricated on the sample [121]. The fabrication process is extremely difficult and time-consuming at the nanoscale, although it is still possible, as shown by Storm *et al.* [122]. However, even if contacts are successfully fabricated on the sample, the deposition process can cause local damage to the crystal, introduce strain, and alter the surface chemistry [123, 124]. Nanostructures have exceptionally large surface-to-volume ratios, hence any changes to their surface state can significantly impact their properties [11, 125, 126]. Therefore, it is necessary to use alternative, non-contact characterisation tools to avoid the complications of contacts and measure the intrinsic properties of micro/nanoscale semiconductors.

THz spectroscopy is an ideal tool to study micro- and nanostructured semiconductors with ultrafast time resolution. As a contact-free technique, THz spectroscopy can measure the pristine semiconductor with high throughput. Additionally, the timescale of charge transport processes in nanoscale materials is similar to their bulk forms, which THz radiation is sensitive to [11].

THz spectroscopy has been employed to investigate a range of different structured semiconductors, including nanoparticles [127, 128], nanowires [62, 74, 75, 85, 86, 111], and nanobars [129]. The conductivity spectrum for these materials includes a resonance – a large deviation from the free-electron response (Drude) of the corresponding bulk semiconductors [73, 104, 130, 131]. This resonance is a result of the sample geometry and is not part of the intrinsic carrier response [81]. Such structural resonances must be carefully treated in the analysis to ensure that the spectra are correctly interpreted and any extracted properties are representative of the material.

In this chapter, the influence of micro- and nanoscale structure on the photoconductivity spectra of semiconductors is explored and a method for separating this influence from the intrinsic THz carrier dynamics is verified. Initial experiments focus on GaAs nanowires of different lengths in order to establish a microscopic (physical) mechanism behind the resonances and to gain insight about the influence of structure size. Next, a well-defined system of microsquare arrays, ranging in size from 500 × 500 to 7 × 7 μm^2, fabricated from GaAs thin film is studied. An increase in the THz resonant frequency is observed as the size of the microsquares decreases, which mirrors the result observed in the length-dependent nanowires. The surface plasmon model [81] is verified as a method to separate the geometric resonance from the intrinsic GaAs response. Charge-carrier density dependent experiments and finite-difference time-domain (FDTD) simulations are employed to confirm the plasmonic nature of the resonances in the conductivity spectra.

GaAs nanowires play an essential role in this chapter – as both motivation for the study and as a material to analyse – and so the following section provides a condensed review of the relevant III–V semiconductor nanowire literature. This chapter is an adaptation of my work published in Ref. [78].

4.2 III–V Semiconductor Nanowires

III–V semiconductor nanowires are quasi-one dimensional structures with diameters typically less than 300 nm and lengths that extend up to several microns. Their reduced dimensionality grants nanowires unique properties that can greatly differ from their bulk counterparts. III–V nanowires are highly attractive building blocks for next-generation optoelectronic devices owing to their direct bandgaps, excellent charge transport properties, and compatibility with existing silicon electronics [11, 132, 133]. Nanowires have been demonstrated as part of field-effect transistors [134], nanoscale light emitters and detectors [135], and as components for photovoltaics [136]. Their

ability to guide and confine light at the nanoscale has enabled nanowire waveguides and lasers, while their high surface-to-volume ratio makes them excellent candidates for sensing applications [137].

Nanowires are highly sensitive to changes in their composition and crystallographic phase [61, 138–141]. Therefore, optimal nanowire fabrication requires a highly controlled process. There are two general approaches to nanowire fabrication: top-down and bottom-up [142]. The top-down approach uses etching and lithographic processes to pattern nanowires out of a bulk material. Top-down methods were adopted by the microelectronics industry, however lithographic resolution limits have made it challenging to fabricate ever-smaller, defect-free nanowires. In contrast, bottom-up techniques synthesise the nanowires by combining the constituent atoms to "grow" the nanowire [143]. Bottom-up growth allows for extreme control over the nanowire composition and geometry, making these methods especially promising for applications in nanoscale optoelectronics.

One of the most widely utilised nanowire growth mechanisms is the vapour-liquid-solid (VLS) mechanism [144, 145]. In VLS, a liquid metal droplet (the liquid), commonly gold, is used as a catalyst for growth. This catalyst mediates the absorption of gas-phase precursors (the vapour) and their crystallisation into a nanowire (the solid). Figure 4.1 depicts the VLS mechanism in the growth of a silicon nanowire. Other growth mechanisms are also used, including template-assisted growth, in which a template confines the crystal growth to one dimension [61]. Advances in fabrication techniques, such as molecular beam epitaxy (MBE) and metal-organic chemical vapour deposition (MOCVD), have enabled the synthesis of high-quality nanowires across a wide range of III–V materials, including GaAs, InP, and InAs [11, 146].

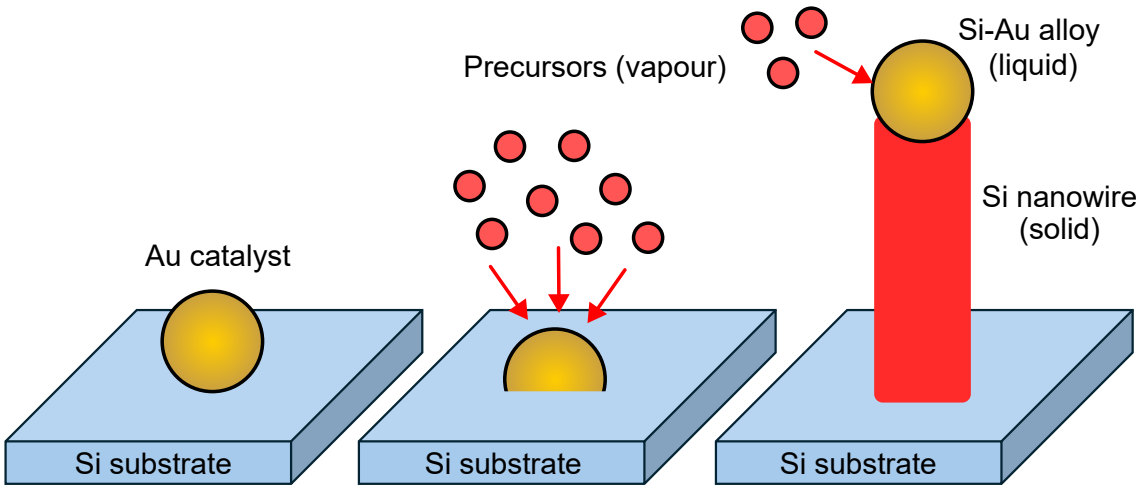

Figure 4.1: Schematic diagram of the VLS mechanism for the growth of a silicon nanowire using a gold catalyst.

4.2.1 Electronic and Optical Properties

III–V semiconductor nanowires are a particularly promising system because their electronic and optical properties can be precisely tuned through variations in composition and morphology. One of the most interesting parameters to tune is the degree of radial confinement. Quantum confinement phenomena can arise if the nanowire diameter becomes comparable to the semiconductor Bohr exciton radius, leading to size-dependent properties [147]. For example, the photoluminescence spectra of InP nanowires was shown to shift to higher energies as the nanowire diameter decreased [148]. Size dependent tuning of nanowire properties presents many opportunities for fundamental research on low dimensional systems as well as for novel device designs [147].

The large surface-to-volume ratio of nanowires makes properties such as charge-carrier lifetime and mobility extremely sensitive to the surface states [125]. Often non-radiative recombination centres form at the nanowire surface, which restricts the nanowire optoelectronic properties. A common method for mitigating this effect is by surface passivation. For example, growing an AlGaAs shell around a GaAs nanowire core

to create a GaAs/AlGaAs core-shell nanowire can significantly increase the charge-carrier lifetime and mobility compared to bare GaAs nanowires [149–151].

The anisotropic geometry of nanowires, coupled with their large dielectric mismatch with their environment, leads to strong polarisation sensitivity [63]. That is, the absorption and emission coefficients depend on whether the light is polarised parallel or perpendicular to the long axis of the nanowire, which can be exploited for polarisation sensitive devices, such as polarisation-sensitive THz detectors [57–59, 64]. The subwavelength geometry of nanowires also enables excellent waveguiding properties and strong light-matter interactions. These properties have allowed for development of nanowire lasers, LEDs, and photodetectors [147]. Furthermore, nanowire ensembles have been shown to provide enhanced light trapping, which can be leveraged in photovoltaic applications [136].

4.2.2 GaAs Nanowires

GaAs nanowires represent one of the most extensively studied III–V nanostructures [11]. Bulk GaAs is a very important semiconductor owing to its direct bandgap of approximately 1.41 eV (corresponding to photon wavelengths of ∼880 nm) [109] and very high electron mobility, which make GaAs ideally suited for high-performance optoelectronic applications. GaAs nanowires retain these advantages while offering greater tunability for specific applications. As this chapter studies GaAs nanowires, this section of the review focuses on their growth and characterisation by THz spectroscopy.

GaAs nanowires are commonly grown by MBE or MOCVD using gold nanoparticle catalysts. In particular, MOCVD allows for scalable nanowire fabrication with excellent control over diameter, length, orientation, and doping, making it the most promising method for industrial production. Au-assisted MOCVD works using the VLS growth mechanism, where the vapour phase group III and V precursors decompose to yield group III and V elements. These elements preferentially deposit at the Au-substrate

interface, thus mediating nanowire nucleation. Deposition of the constituent III–V material continues at the nanowire-Au interface, driving axial nanowire growth. The nanowire tip diameter is determined by the Au nanoparticle diameter. Simultaneously, III–V material can be deposited on the nanowire side walls, expanding the nanowire radially. This radial growth often results in tapering, where the nanowire base is wider than the tip. The growth conditions control the amount of axial and radial growth. See Ref. [61] for a detailed description of Au-assisted MOCVD nanowire growth.

THz spectroscopy has emerged as a powerful tool for characterising GaAs nanowires owing to its non-contact nature. Initial OPTP studies by Parkinson *et al.* demonstrated that the THz conductivity spectra of GaAs nanowires deviates strongly from the Drude response of bulk GaAs owing to a strong resonance [85]. The frequency of this resonance was found to decrease with increasing photoexcitation fluence (thus increasing charge-carrier density), following the trend expected for surface plasmon resonances (Equation 2.55) [81]. Fitting the surface plasmon model (Equation 2.54) to the nanowire conductivity allowed for extraction of the charge-carrier mobility and density. The bare GaAs nanowires had significantly lower electron mobilities than bulk GaAs, which was attributed to scattering at surface defects. Photoconductivity decay traces revealed short carrier lifetimes ($< 10\,\mathrm{ps}$) in the nanowires owing to ultrafast trapping at the nanowire surface. These short lifetimes have been exploited in ultrafast polarisation modulators [152].

Research by Joyce *et al.* investigated the relationship between GaAs nanowire diameter and charge-carrier lifetime [62]. Lifetimes were found to decrease with decreasing diameter, highlighting the effect of surface states on the optoelectronic properties of nanowires. Furthermore, they found that GaAs nanowires have a very high surface recombination velocity of $5.4\times10^5\,\mathrm{cms}^{-1}$, making surface passivation highly important for most device applications. A later study found that the mobility of GaAs nanowires

was strongly degraded when the diameter was reduced, further emphasising the need for surface passivation [153].

Many studies have explored the effect of passivating the GaAs surface by overcoating it with AlGaAs to create a GaAs/AlGaAs core-shell nanowire. Work by Parkinson *et al.* determined that the surface-trap density was 82% lower in GaAs/AlGaAs core-shell nanowires than in bare GaAs nanowires, leading to an increase in carrier lifetime by a factor of ~ 4 [86]. Additionally, improvements to the growth process allowed crystallographic twin defects to be eliminated, which further increased the nanowire mobility and lifetime. Joyce *et al.* later optimised the GaAs/AlGaAs nanowires to achieve photoconductivity lifetimes of 1.6 ns and mobilities up to 3000 $\mathrm{cm^2V^{-1}s^{-1}}$, comparable to bulk GaAs [151].

Boland *et al.* extended the research on GaAs/AlGaAs core-shell nanowires by incorporating a Si-doped layer to the AlGaAs shell. The surface plasmon model was employed to determine the charge-carrier density at different photoexcitation fluences, which allowed the number of photoinjected carriers to be separated from the equilibrium carrier density. An extrinsic electron density of $1.1\times10^{16}\,\mathrm{cm^{-3}}$ was recorded, demonstrating the effectiveness of modulation doping for increasing the nanowire charge-carrier density. Additionally, the photoconductivity lifetime was extended to 3.9 ns, showing that modulation doping can effectively passivate interfacial traps [111, 154]. Boland *et al.* also investigated the effect of overcoating the GaAs core with p- and n-type doped GaAs shells. Electron and hole densities greater than $10^{18}\,\mathrm{cm^{-3}}$ were measured for n- and p-type doping respectively. These high carrier concentrations are very promising for GaAs nanowire device applications. Moreover, the photoconductivity lifetimes increased from 0.13 ns in the undoped nanowires to 3.8 and 2.5 ns in the n- and p-doped nanowires respectively, indicating that this doping method can be an alternative method of surface passivation. However, the carrier mobilities were significantly reduced owing to scattering off the introduced impurities [74].

More recently, high electron mobility has also been reported in strained GaAs nanowires, where careful control of growth conditions enhanced the transport properties [155]. In addition to highlighting the importance of strain engineering for mobility enhancement, this work subtly pointed to the role of nanowire geometry in determining transport behaviour. In particular, the study compared nanowires arranged side-by-side with those aligned end-to-end and observed a decrease in the resonant frequency for the vertically aligned nanowires. This investigation implicitly raises the question of how nanowire length and collective geometry influence measured THz responses. While the focus of that work was on strain-induced mobility enhancement, the observations reinforce that nanowire length and arrangement can play a significant role in determining photoconductivity spectra. This connection motivates the work presented in this chapter, where the effect of nanowire length on THz photoconductivity resonances is explicitly investigated.

Overall, THz spectroscopy has established itself as an important tool for characterising GaAs nanowires. While previous studies have addressed property characterisation, surface passivation, and doping, the role of nanowire geometry – particularly length – remains less explored. This chapter addresses this gap by exploring the effect of nanowire length on the surface plasmon resonances and validating the surface plasmon model as a means to extract the charge-carrier properties from nanowires and other nanostructures [78].

4.3 Experimental Methods

The samples were studied by OPTP spectroscopy using the same conditions as described in Section 3.3.1, except the optical-pump beam was not blocked. Instead, the pump beam was directed onto the sample to photoexcite free charge carriers. A neutral density filter wheel was used to control the pump fluence and thus the photoinjected carrier density. THz radiation was generated using the AR+HR-coated STE described in Chapter 3.

The emitted THz pulse was focused onto the sample and overlapped with the centre of the pump beam. At the sample, the THz spot had a FWHM of ∼0.8 mm, which was much smaller than the ∼7.5 mm FWHM of the optical-pump beam. This size difference ensured the THz pulse probed a homogeneous charge-carrier density. A delay stage was used to control the relative timing of the pump beam and THz pulse at the sample.

4.4 Results and Discussion

4.4.1 Length Dependence of Nanowires on THz Photoconductivity Spectra

GaAs nanowires were grown by Dr. Chawit Uswachoke at the University of Cambridge, UK. Briefly, the nanowires were grown on (111)B GaAs substrates by the VLS mechanism inside a MOCVD system. The duration of each growth was carefully controlled such that nanowires of different lengths were produced. In total, three samples were grown with nominal lengths of 8, 6, and 2 μm. All nanowires had approximately 50 nm diameters. After growth, the nanowires were mechanically transferred onto 2-mm-thick, z-cut quartz substrates for measurement.

After substrate transfer, the nanowire samples were imaged using a scanning electron microscope (SEM) by Dr. Kun Peng at the University of Oxford, UK. Thin conductive layers of 5 nm/10 nm Ti/Au were deposited onto the nanowires by sputter coating in order to reduce the electrical charging of the nanowires under the electron beam. The SEM images are presented in Figure 4.2 (a). As shown in the figure, the substrate transfer method ensured the nanowires were reasonably well aligned, minimising the effects of nanowire polarisation anisotropy on the photoconductivity spectra [63, 152].

Many nanowires broke during substrate transfer, thus they are much shorter than their growth lengths and each sample has a distribution of nanowire lengths. To assess the post-transfer nanowire lengths, Fiji image analysis software [156] was used to manually

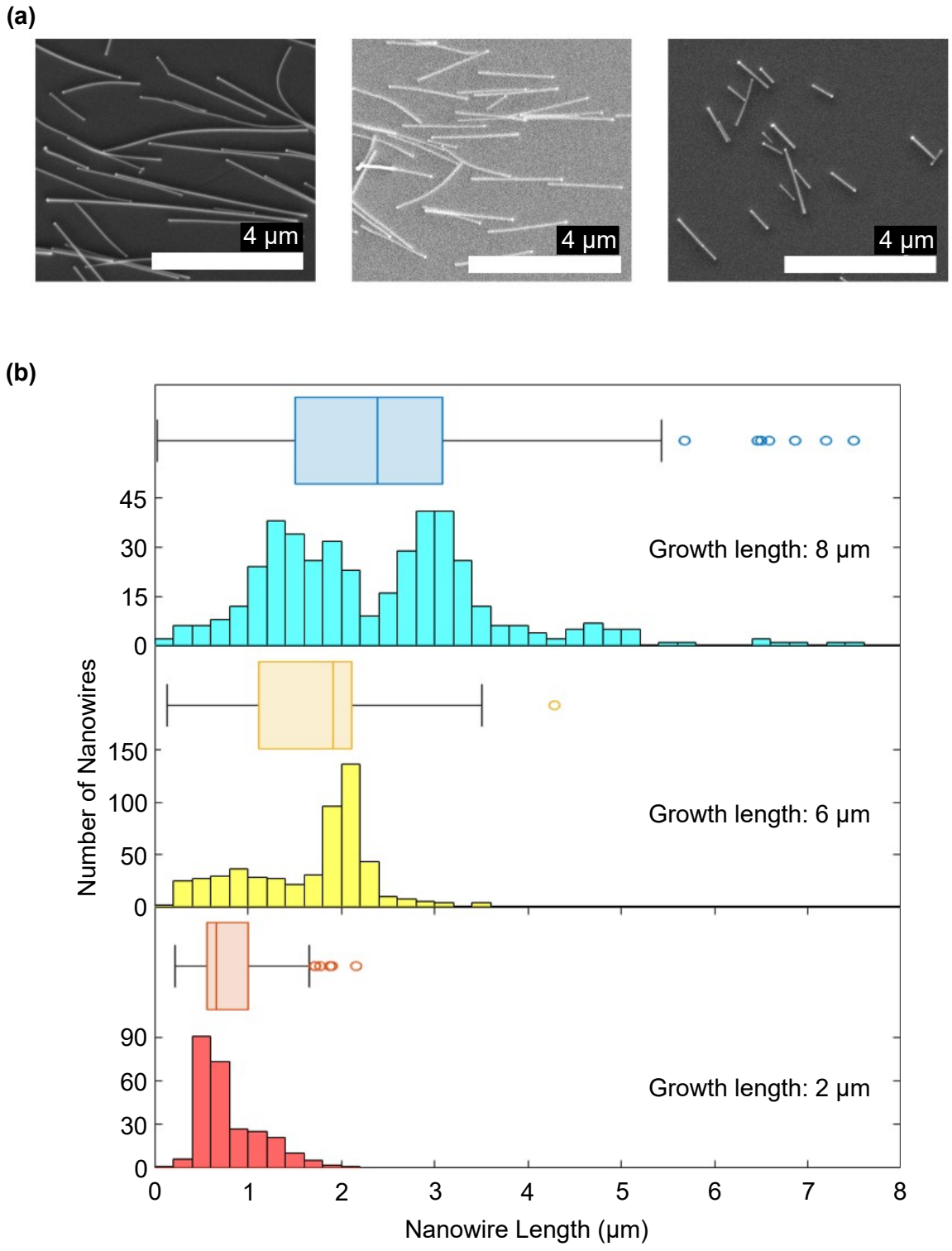

Figure 4.2: (a) SEM images of the GaAs nanowire ensembles after transfer to quartz substrates [images taken by Dr. Kun Peng]. The nominal growth lengths from left to right are: 8 μm, 6 μm, and 2 μm. The scale bar is 4 μm in each image. (b) Histograms of the nanowire length distributions for each sample after transfer onto quartz substrates. Note that the supporting boxplots were calculated with pre-binned data.

calculate the length of nanowires from the SEM images. Table 4.1 summarises the results and Figure 4.2 (b) presents histograms of the length distributions. Note that the nanowires often bundled together, particularly the longer nanowires, which made it impossible to confidently measure their length. Hence, the length statistics are weighted towards the shorter, more confidently measured nanowires, and the length statistics act as a lower bound for the true average lengths. While there is a large distribution of lengths for each sample, there is a clear increase in nanowire average length with increasing growth length.

Growth length (μm)	Mode length (μm)	Mean length (μm)	Median length (μm)	Standard deviation (μm)	Total measured nanowires
8	3	2.41	2.38	1.20	433
6	2	1.66	1.91	0.69	535
2	0.5	0.79	0.65	0.35	262

Table 4.1: Statistics for the nanowire length distributions for the three nanowire samples. All data was manually measured from SEM images using Fiji software [156].

Here onward, the nanowire samples are referred to by the mode of their length distribution after substrate transfer: 0.5, 2, and 3 μm. Dr. Djamshid Damry (University of Oxford, UK) used OPTP spectroscopy to measure the photoconductivity spectra of the nanowires while I conducted all data processing and analysis. The photoconductivity was extracted from the OPTP measurements using the procedure described in Section 2.6.3, with sample fill factors determined by analysis of optical microscope images of the nanowires, which were captured by Dr. Kun Peng.

The photoconductivity spectra of the nanowire ensembles are presented in Figure 4.3. Each spectrum exhibits a distinct resonance that increases in frequency as the nanowire length decreases. Importantly, this trend holds regardless of whether the mode, median, or mean of the length distribution (Table 4.1) is taken as the characteristic length, demonstrating a robust inverse relationship between nanowire length and resonant frequency. This behaviour is consistent with simulations of neighbouring GaAs nanowires,

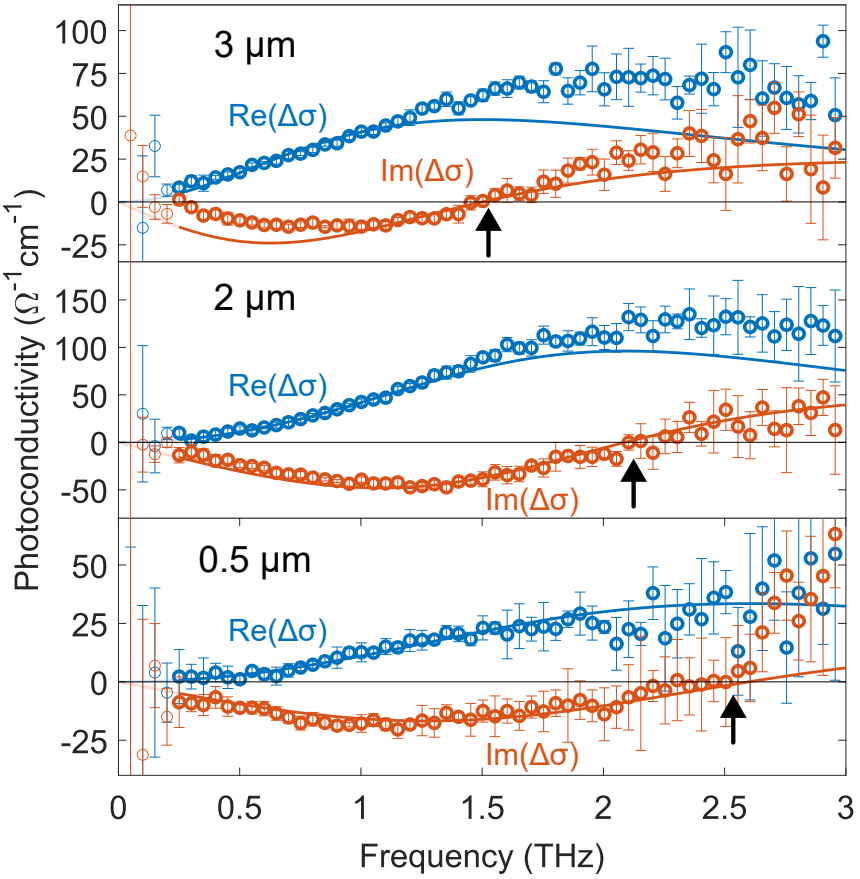

Figure 4.3: THz photoconductivity spectra of the three different nanowire samples, labelled by their mode length after substrate transfer. The solid lines show fits to the surface plasmon model (Equation 2.54), and the arrows indicate the resonant frequencies. Data were measured 0.5 ps after photoexcitation with a pump beam fluence of 395 μJcm^{-2}. These data were measured by Dr. Djamshid Damry, while I conducted the analysis.

which show that end-to-end aligned nanowires can behave as a single longer structure with a lower resonant frequency [155]. Moreover, a similar length-frequency relationship has been reported in mid-infrared studies of silicon nanowires [157], suggesting that this phenomenon is general to semiconductor nanowire systems.

The origin of the geometric resonance is described by Nienhuys and Sundström [81], who developed the surface plasmon model to explain how small-scale structure can change the conductivity spectrum of a material. This model is detailed in Section 2.7.2. Briefly, the surface plasmon model introduces an electrostatic restoring force to the Drude

equation of motion, which results in harmonic oscillations with a resonant frequency. The conductivity under this model is given by Equation 2.54. The resonant frequency is related to the sample geometry through a factor g (Equation 2.55). By fitting the surface plasmon model to the photoconductivity spectra, the charge-carrier mobility (μ) and density (N) can be extracted, along with the resonant frequency (ω_0) and geometric factor. Note that the effective mass of electrons in GaAs ($0.063\,m_e$, where the rest mass of the electron is $m_e = 9.109 \times 10^{-31}\,\mathrm{kg}$) is much smaller than the mass of holes ($\sim 0.5\,m_e$) [158]. Thus, the electrons have a greater contribution to conductivity than the holes, and any extracted properties are attributed fully to the electrons.

The solid lines in the spectra of Figure 4.3 indicate fits to the surface plasmon model using a non-linear least squares algorithm with three free parameters: N, ω_0, and μ. The model agrees reasonably well with the experimental data. Table 4.2 displays the fit parameters along with the fill factor for each sample. The charge-carrier densities strongly depend on the fill factor, which is challenging to estimate in these inhomogeneous nanowire arrays. Hence, the calculated differences in N are likely due to differences between the calculated fill factor and the true fill factor of the nanowires at the measured position.

The extracted mobilities were similar across all nanowire samples and are consistent with previously reported values for GaAs nanowires of comparable dimensions [62]. This indicates that nanowire length has little to no influence on charge-carrier mobility. By contrast, studies investigating nanowire diameter have reported a reduction in mobility as diameter decreases, which is attributed to the enhanced impact of surface scattering at higher surface-to-volume ratios [153]. However, unlike diameter, variations in length do not significantly alter the surface-to-volume ratio, as both parameters scale approximately linearly with nanowire size. Consequently, mobility remains largely independent of nanowire length.

Mode length (μm)	Fill factor	N ($\times 10^{17}$ cm^{-3})	ω_0 (THz)	μ (cm^2 V^{-1}s^{-1})
3	0.19 ± 0.07	2 ± 1	1.50 ± 0.08	1500 ± 100
2	0.14 ± 0.04	4 ± 2	2.09 ± 0.08	1500 ± 100
0.5	0.12 ± 0.03	1.9 ± 0.5	2.6 ± 0.2	1100 ± 300

Table 4.2: Nanowire material characteristics extracted from fits to the surface plasmon model to the spectra shown in Figure 4.3. Errors were determined by propagating the error in the nanowire fill factor.

The inverse relationship between nanowire length and resonance frequency has direct consequences for interpreting THz spectra from ensembles of nanowires, as illustrated in Figure 4.4. In particular, the width of the resonance is directly related to the charge-carrier mobility: the broader the resonance, the lower the mobility [11]. In an ensemble of nanowires with a distribution of lengths – commonly as result of nanowires breaking during substrate transfer – each nanowire will have a slightly different resonance frequency. The superposition of these resonances yields a broadened feature that, if fitted by a single resonance model, will result in an artificial decrease in the nanowire mobility. As a result, the mobility extracted from THz analysis of nanowire ensembles should be treated as a lower bound on the true mobility.

The artificial resonance broadening effect and the difficulty in determining fill factor and average nanowire length after substrate transfer are complications that arise from working with the inhomogeneous nanowire ensembles. These results can suggest a relationship between length and geometric resonances, but the sample inhomogeneities make it difficult to conclude anything meaningful. Thus, to fully understand the relationship between these resonances and structure size, it is necessary to investigate a well-defined system that does not suffer from the effects of inhomogeneity.

4.4.2 GaAs Microsquare Arrays

To confirm the link between size and resonance in structured semiconductors, a system of GaAs microsquare arrays were fabricated and studied. The microsquares were fabricated

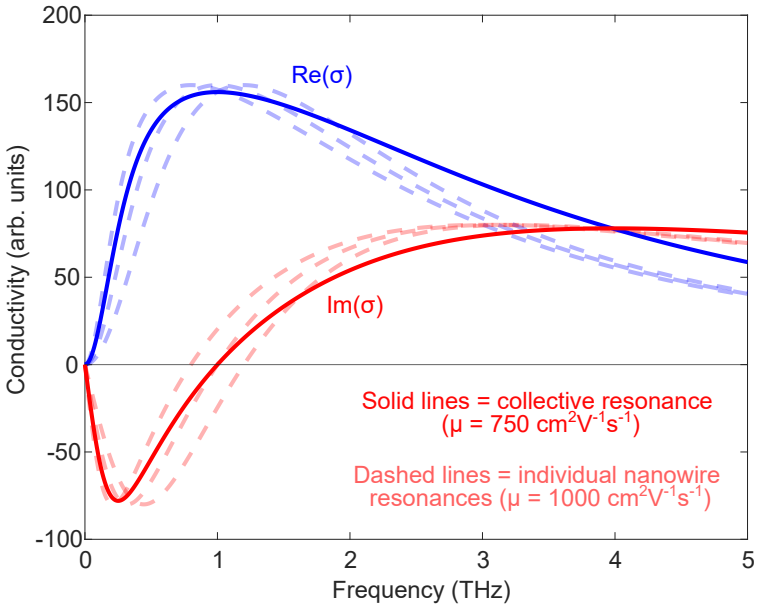

Figure 4.4: Example conductivity spectra emphasising the impact of resonant frequency being inversely related to nanowire length. The dashed lines show the conductivity of nanowires of different lengths (resonant frequencies 0.8, 1.0, 1.2 THz) but the same charge-carrier mobility of $1000\,\mathrm{cm^2\,V^{-1}s^{-1}}$. The solid line shows a potential surface-plasmon fit to the nanowire ensemble. The ensemble has a lower mobility of $750\,\mathrm{cm^2\,V^{-1}s^{-1}}$ as a result of the spectral broadening from the different nanowire resonant frequencies.

by Dr. Tuomas Haggren (Australian National University, Australia) and full details of the fabrication are available in Appendix A.1. Briefly, 600-nm-thick GaAs films were epitaxially grown using MOCVD on (100) GaAs substrates. Electron beam lithography was used to pattern an approximately 5×5 mm area into an array of squares. The GaAs wafer was then hot embossed onto a 2-mm-thick c-sapphire substrate, and then the bulk GaAs was etched away, leaving the patterned GaAs film on c-sapphire. Sapphire offers excellent thermal conductivity and is transparent over the THz range, making it an excellent substrate for THz photoconductivity studies [104]. A thin-layer of PMMA (1.2 μm) and SU8 (800 nm) separated the GaAs and sapphire for lithographic and adhesion purposes. Measurements of a sapphire substrate with the same polymers showed no response, thus the polymers are expected to have negligible impact on the results.

In total, four samples were prepared: one with $500\times500\,\mu\mathrm{m}^2$ squares, another with

$50\times50\,\mu m^2$ squares, and one with $7\times7\,\mu m^2$ squares. Each microsquare was isolated from the others by 300 nm to ensure electrical isolation. The final sample was an unpatterned, 600-nm-thick GaAs film on c-sapphire, which was used as a reference. Figure 4.5 (b-d) shows SEM images of the microsquare arrays, while Figure 4.5 (a) shows a schematic diagram of the sample geometry relative to the THz pulses during OPTP spectroscopy. All SEM images of the microsquare arrays were taken by Dr. Tuomas Haggren.

The microsquare arrays are an ideal platform to understand the size dependence of the geometric resonances. All samples were fabricated from identically prepared GaAs thin-films, hence any observed differences in their photoconductivity spectra can be directly attributed to their structural differences. Note that these samples satisfy the thin-film approximation, allowing the photoconductivity to be extracted from the OPTP data using the procedure in Section 2.6.2.

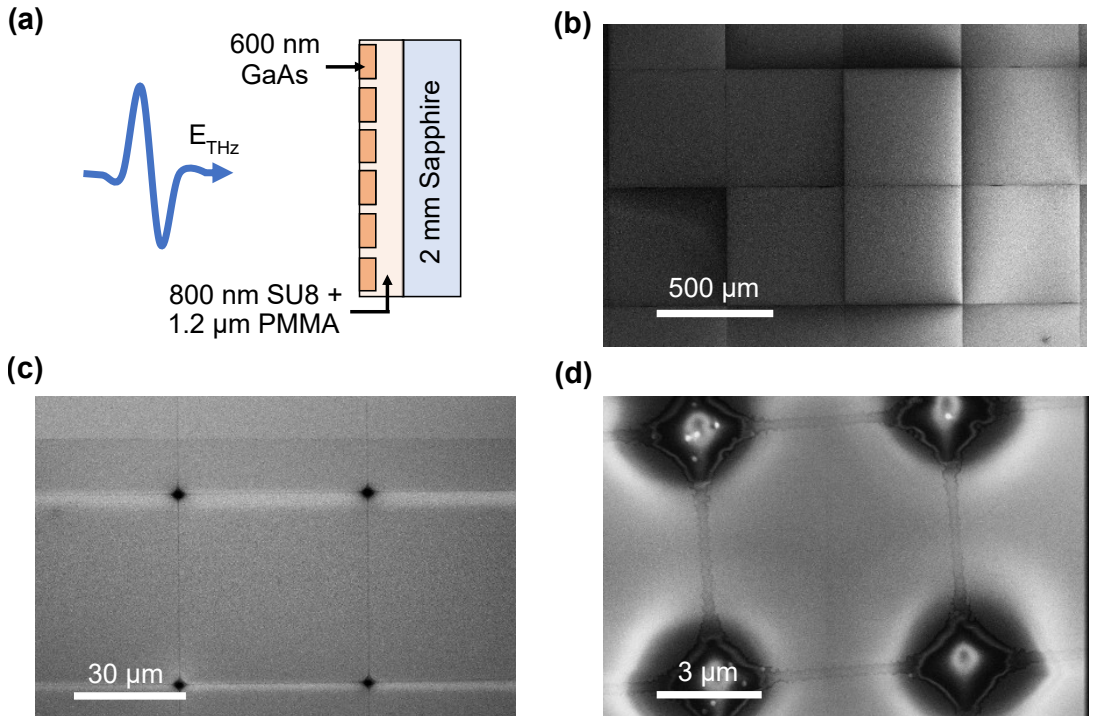

Figure 4.5: (a) Schematic diagram of the GaAs microsquare sample geometry with respect to the incident THz pulse. (b-d) SEM images of the $500\times500\,\mu m^2$, $50\times50\,\mu m^2$, and $7\times7\,\mu m^2$ GaAs microsquare arrays respectively. The gap between squares is approximately 300 nm. All SEM images of the microsquare arrays were captured by Dr. Tuomas Haggren.

The THz photoconductivity spectra of the GaAs microsquares and reference film are shown in Figure 4.6. The reference GaAs film exhibits a typical Drude photoconductivity spectrum, consistent with results for bulk GaAs [110]. The spectrum of the $500\times500\,\mu m^2$ microsquares is very similar to the spectrum for the GaAs film, indicating that the geometric resonances are not clearly observed in THz measurements at this scale. In contrast, the photoconductivity spectra of the $50\times50\,\mu m^2$ and $7\times7\,\mu m^2$ microsquares show clear resonances at non-zero frequencies. The resonance is at a significantly higher frequency in the $7\times7\,\mu m^2$ microsquares, which aligns with an inverse relationship between structure size and resonant frequency. This result is consistent with the observations in the nanowire ensembles and strongly suggests a general trend in how THz conductivity spectra change with structure size.

The surface plasmon model was fitted to the spectra in Figure 4.6 (solid lines) and is in excellent agreement with the experimental data across most of the frequency range. A small deviation is visible at frequencies below $\sim$0.25 THz, particularly in the 7×7 and $50\times50\,\mu m^2$ samples. This deviation is attributed to aperture-related artefacts resulting from the beam geometry. Specifically, the THz beam is collimated and refocused by a pair of OAP mirrors. This process is highly sensitive to the alignment of the divergent lens located immediately before the THz emitter (see Figure 2.2). Small misalignments of this lens can lead to imperfect collimation and consequently a distorted focus at the sample position. The lower-frequency components, which occupy a larger diffraction-limited spatial area, can clip the edges of the sample aperture or the boundary of the patterned microsquare array. This frequency-dependent clipping can introduce artefacts to the THz transmission, as observed in the low-frequency "bump" in Figure 4.6. Hence, data below 0.25 THz (indicated by transparent circles) were excluded from the surface plasmon model fits.

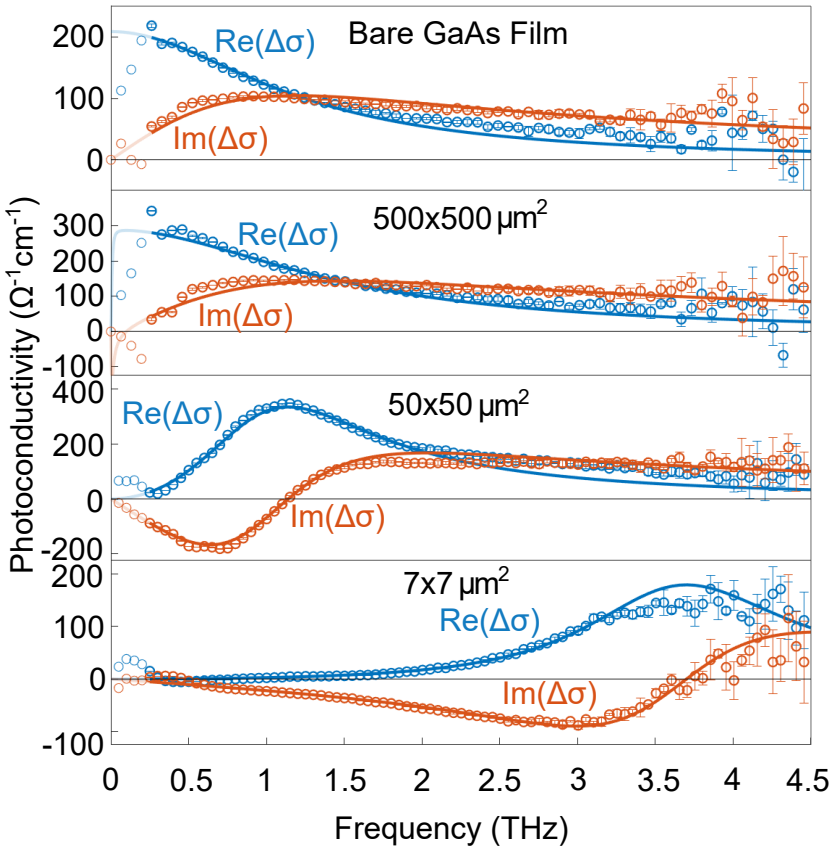

Figure 4.6: THz photoconductivity spectrum of (top to bottom) a 600-nm-thick film of GaAs, a $5\times5\,\mathrm{mm}^2$ array of $500\times500\,\mu\mathrm{m}^2$ GaAs microsquares, $50\times50\,\mu\mathrm{m}^2$ GaAs microsquares, and $7\times7\,\mu\mathrm{m}^2$ GaAs microsquares. The circles represent measured data while the solid lines are fits to the surface plasmon model. Data below 0.25 THz (transparent data points) were excluded from the fit because they suffered from aperture-related artefacts. Data were measured 8 ps after photoexcitation at a fluence of $23.6\,\mu\mathrm{J\,cm}^{-2}$. Note that the presented bare GaAs film data was measured by Dr. Jasmin-Clara Bürger and Dr. Terng Junn Keat to correct for artefacts in my initial measurements.

Table 4.3 shows the extracted parameters from the surface plasmon model fits. Note that the reference film was fitted with the Drude model (Equation 2.54 with $\omega_0 = 0$) as it had no structure to allow for the formation of a depolarisation field. Interestingly, the fitted data suggests that there was a resonance at very low frequencies (0.1 THz) in the $500\times500\,\mu\mathrm{m}^2$ sample. This resonance is at too low a frequency to be accurately resolved in our spectrometer, but would be expected to appear in measurements that can better resolve this low frequency range. The charge-carrier densities varied from the experimentally calculated value of $5.4\times10^{17}\,\mathrm{cm}^{-3}$, however the values were within

expectations when accounting for differences in absorption and charge recombination between samples. Critically, the electron mobilities were similar across all samples, despite the significant differences in their photoconductivity spectra. It was known that the samples had similar properties as they were prepared from identical GaAs films. Hence, this result confirms that the surface plasmon model can successfully separate the influence of sample geometry from the intrinsic charge-carrier response in THz spectroscopy.

Microsquare Sample	N ($\times 10^{17}\,\mathrm{cm}^{-3}$)	ω_0 (THz)	μ ($\mathrm{cm}^2\,\mathrm{V}^{-1}\mathrm{s}^{-1}$)
Film	3.5 ± 0.3	0	3700 ± 500
$500 \times 500\,\mu\mathrm{m}^2$	5.9 ± 0.1	0.1 ± 0.1	3000 ± 300
$50 \times 50\,\mu\mathrm{m}^2$	3.5 ± 0.3	1.14 ± 0.01	3200 ± 100
$7 \times 7\,\mu\mathrm{m}^2$	4.0 ± 0.1	3.7 ± 0.1	2800 ± 200

Table 4.3: GaAs microsquare array material characteristics extracted from fits to the surface plasmon model to the spectra shown in Figure 4.6. Errors are the standard deviation of fits to three repeated THz scans.

4.4.3 Plasmonic Nature of the Resonance

Sections 4.4.1 and 4.4.2 established an inverse relationship between feature size and geometric resonance frequency in THz studies of structured semiconductors. This section confirms that the resonances follow the plasmonic description of Nienhuys and Sundström [81] by measuring the photoconductivity spectrum of the $7{\times}7\,\mu\mathrm{m}^2$ microsquare array at different photoexcitation fluences. Figure 4.7 (a) shows the measured photoconductivity spectra. The resonant frequency significantly increases with excitation fluence. Figure 4.7 (c) shows that this increase in resonant frequency is proportional to the square root of the charge-carrier density – a clear signature of plasmons (Equation 2.55).

The experimental results are supported by FDTD simulations conducted by Dr. Thomas Siday (University of Oxford, UK) using the Lumerical commercial FDTD solver. In the simulation, an individual, isolated, $7{\times}7\,\mu\mathrm{m}^2$ GaAs microsquare was excited by a total field scattered field source at normal incidence with a centre frequency of 3 THz. Aside from being isolated to avoid strong diffraction effects, the GaAs microsquares were

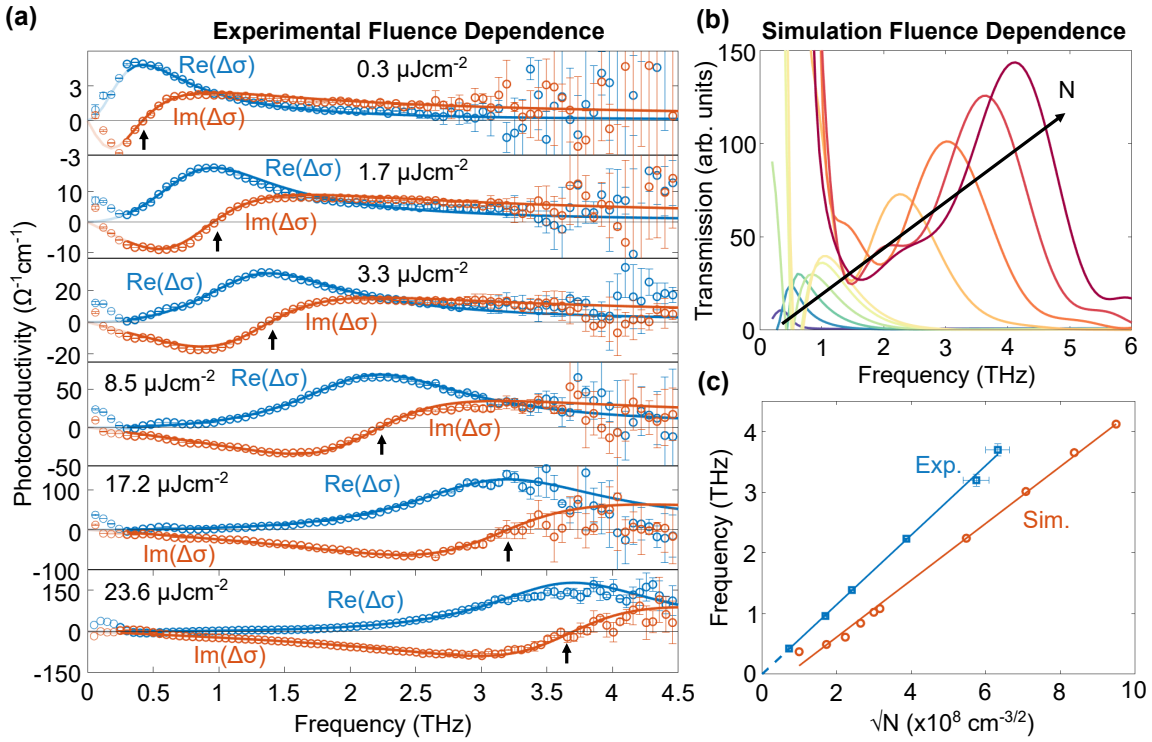

Figure 4.7: (a) THz photoconductivity spectra of the $7\times7\,\mu m^2$ microsquare array measured $\sim$8 ps after photoexcitation with excitation fluences of 0.3 to 23.6 $\mu J\,cm^{-2}$. The circles are the measured data while solid lines are fits to the surface plasmon model. Black arrows indicate the resonant frequency. (b) Select photoconductivity spectra from FDTD simulations [conducted by Dr. Thomas Siday] of a single $7\times7\,\mu m^2$ microsquare at different charge-carrier densities ranging from 1×10^{16} to $9\times10^{17}\,cm^{-3}$. The arrow indicates the increasing resonant frequency with increasing charge-carrier density, N (low densities are blue and become progressively redder as the charge-carrier density increases). (c) Plot of the resonant frequency against $\sqrt{N}$. The blue data shows the relationship for the experimental data presented in (a), whereas the red data shows the relationship for the simulation data in (b).

otherwise modelled as closely as possible to the experimental configuration, including the sapphire substrate and PMMA/SU8 polymer layers. A Drude model conductivity was added to the GaAs to model the photoexcitation, and then the power transmission through the sample was measured with a transmission monitor and normalised to the non-photoexcited case.

Figure 4.7 (b) shows the FDTD THz transmission spectra at charge-carrier densities of 1×10^{16} to $9\times10^{17}\,cm^{-3}$. The transmission has a strong peak that shifts to higher frequencies as the charge-carrier density increases. This maximum corresponds to the

resonance condition, where incident THz radiation couples most effectively into the structure. This is the same resonance that appears as a peak in the photoconductivity spectra of the experimental data. The red data in Figure 4.7 (c) shows that the resonant frequencies from the FDTD simulations are proportional to the square root of the charge-carrier density. This result matches the experiments, except with an offset of a factor of 2. This offset is likely due to differences in the background doping and optical absorption between the experiment and simulation. Yet, the good agreement between simulations and experiments strongly indicates a plasmonic origin to the resonance observed in the microsquares. Previous studies have identified this same trend in nanowires [85, 86], thus linking the results on nanowires and microsquares to the same phenomena relating plasmonic resonant frequencies to their geometry.

According to Equation 2.55, the geometric factor g determines the proportionality between ω_0 and $\sqrt{N}$, with higher values of g corresponding to stronger confinement of the plasmon mode. Figure 4.8 (a) plots the extracted geometric factor for the nanowire samples as a function of nanowire length. As expected, shorter nanowires exhibit larger g values, reflecting stronger confinement and higher resonant frequencies. The trend confirms that length plays a key role in defining the resonance behaviour through its influence on the depolarization field. In comparison, Figure 4.8 (b) shows the geometric factor for the microsquare samples as a function of side length on a log-log scale. Here, g spans several orders of magnitude, decreasing sharply with increasing microsquare size. This result highlights the strong size dependence of plasmonic resonances in microscale structures. Finally, to confirm that g is independent of photoexcited carrier density, the geometric factor was extracted for the 7×7 μm^2 microsquares across a range of excitation fluences, as shown in Figure 4.8 (c). The geometric factor remains approximately constant, within uncertainty, confirming that g is a purely geometric quantity and is not influenced by changes in carrier density or pump fluence. Together, these results validate the

surface plasmon model and demonstrate that the geometric factor describes the resonant behaviour in nanostructured semiconductors.

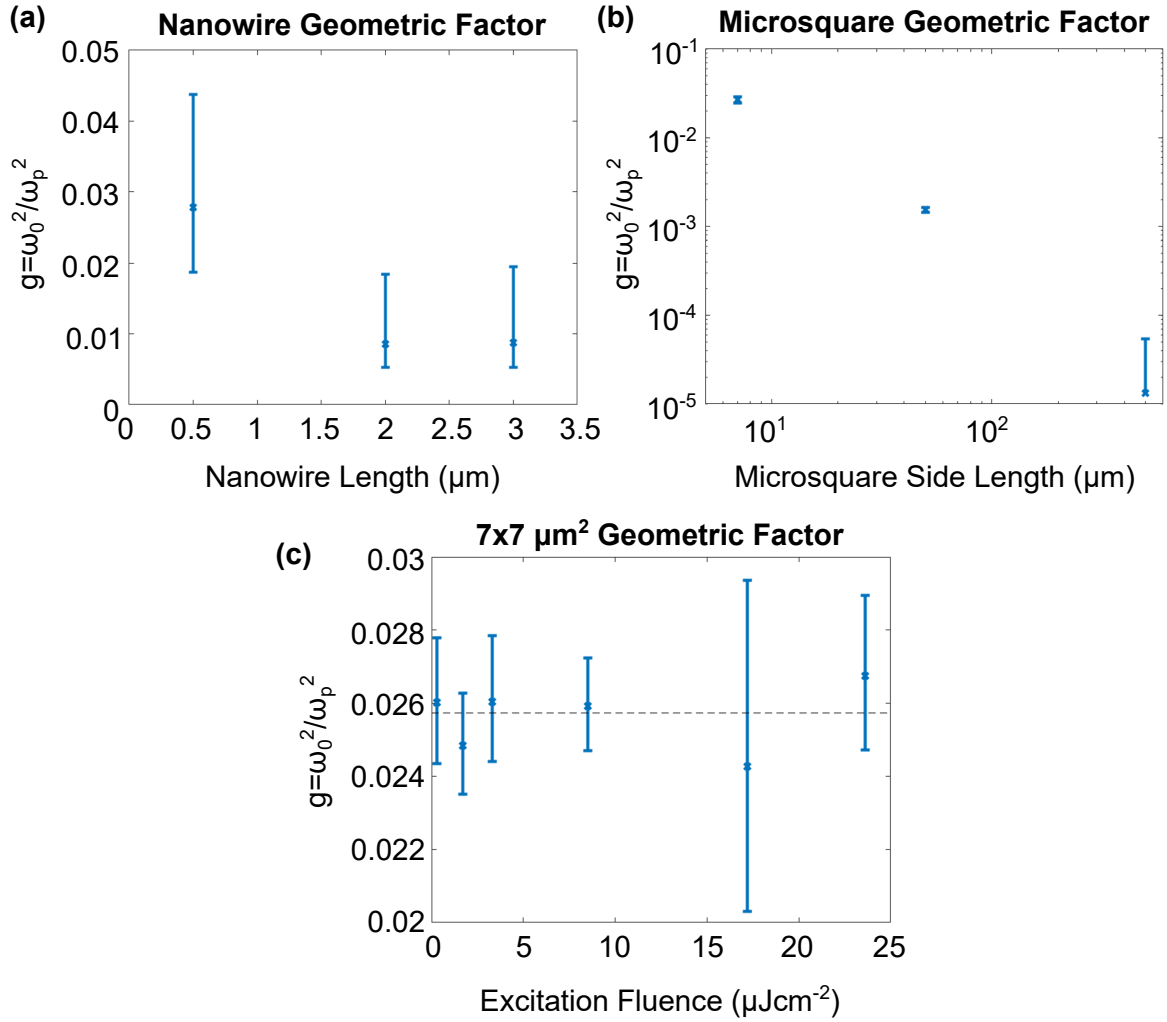

Figure 4.8: Geometric factors, g, for (a) nanowires of different lengths, and (b) microsquares of different sizes. Note that (b) is on a log-log scale to improve data visibility. (c) shows the geometric factor of the 7×7 μm^2 microsquares sample for the different excitation fluences used in Figure 4.7 (a). The dotted line is a guide to the eye to highlight the stable value of g. Errors in each plot were estimated by propagating the error in N and ω_0 into Equation 2.55.

4.5 Conclusion

This chapter has investigated the influence of sample geometry on THz photoconductivity measurements, with a particular focus on ensembles of GaAs nanowires and microsquare arrays. Plasmonic resonances were observed in both material systems, with the resonant

frequency increasing as feature size decreased. These resonances were accurately described using the surface plasmon model, which enabled extraction of key material properties. In particular, electron mobilities could be accurately separated from the geometric resonance using the surface plasmon model. Furthermore, the electron mobilities of the GaAs nanowires were largely unaffected by nanowire length, which is consistent with the expectation that length does not significantly alter the nanowire surface-to-volume ratio.

From a broader perspective, this study demonstrated that structural inhomogeneities – such as variations in nanowire lengths within an ensemble – can artificially broaden the plasmonic resonance and thus reduce the mobility extracted using the surface plasmon model. Consequently, the charge-carrier mobilities extracted from such samples should be interpreted as lower bounds for the true mobility.

Fluence-dependent experiments and FDTD simulations demonstrated that the resonant frequency also scaled with the square root of the charge-carrier density – a defining characteristic of surface plasmon modes. Hence, the size dependence observed in this study is expected to apply to any material system exhibiting such plasmonic resonances.

The geometric factor, g, quantifies the link between structure and the surface plasmon resonant frequency. The value of g increased as feature size decreased, reflecting the stronger plasmonic confinement in smaller structures. Notably, g was shown to be independent of excitation fluence (charge-carrier density), confirming its role as a purely geometric factor.

Within the broader scope of this thesis, this chapter serves as a focused investigation into the role of geometry in shaping THz photoconductivity measurements. The optimised THz emitters from the previous chapter enabled measurement of the high SNR THz photoconductivity spectra, while this chapter focussed on the interpretation of THz signals from structured nanomaterials. The findings highlight the importance of accounting for geometric resonances when working with nanoscale systems, particularly when extracting

charge transport properties. The next chapter shifts the focus from instrumentation and analysis to practical demonstrations of how THz spectroscopy can characterise III–V semiconductors and methods to engineer their electronic properties.

5

Controlling and Characterising the Properties of $In_{0.53}Ga_{0.47}As$ with Terahertz Spectroscopy

The previous experimental chapters focused on improving THz spectroscopy by optimising the THz emitter (Chapter 3) and by addressing how to accurately interpret THz measurements of nanostructured semiconductors (Chapter 4). Here, the focus shifts to using THz spectroscopy to accurately characterise semiconductors and to determine the optimal material composition and conditions for device applications.

5.1 Introduction

The ternary group III–V semiconductor $In_xGa_{1-x}As$ has received widespread attention owing to its high electron mobility and direct bandgap in the infrared (IR) range. These intrinsic properties make $In_xGa_{1-x}As$ particularly well-suited for high-speed photodetectors operating at the low-loss fibre-optic communication wavelengths of 1300 and 1550 nm [159–161]. The telecommunications industry has driven optimisation of $In_xGa_{1-x}As$, lowering its cost and making $In_xGa_{1-x}As$-based components widely available. As these components become increasingly optimised and economical, they become more

viable for an expanding range of applications. For example, $In_xGa_{1-x}As$ components are now used for quantum communications, high-speed electronics, and off-the-shelf $In_xGa_{1-x}As$ detectors have recently been tested as low-cost alternatives to HgCdTe detectors for astronomical imaging projects [162–164]. The most widely used alloy fraction is $In_{0.53}Ga_{0.47}As$ because it is lattice matched to InP, allowing the growth of thick, low-defect density epitaxial layers, which enables reproducible fabrication of high-performance devices. Furthermore, $In_{0.53}Ga_{0.47}As$ can be easily integrated with other materials that are lattice matched to InP, such as $In_{0.52}Al_{0.48}As$ [165]. Overall, $In_xGa_{1-x}As$ balances performance, price, and compatibility with existing semiconductor infrastructure, making it an attractive material system for a diverse range of electronic and optoelectronic technologies.

Despite these advantages, the relatively long charge-carrier lifetime of $In_xGa_{1-x}As$, which typically exceeds hundreds of picoseconds in undoped/lightly-doped samples [35], limits its applicability in devices that require ultrafast response times, such as high-speed photodetectors and modulators [166–170]. Ultrafast charge-carrier lifetimes ($< 1\,ps$) are particularly important for THz photoconductive antennas (PCAs) for both detection and emission of THz frequency radiation [1, 5, 65, 171]. Therefore, engineering $In_xGa_{1-x}As$ to reduce the charge-carrier lifetime is highly desirable, such that it can be utilised in ultrafast optoelectronic applications.

The main challenge is to reduce the charge-carrier lifetime of $In_xGa_{1-x}As$ without hindering its mobility and resistivity. THz spectroscopy is an ideal tool for accurately characterising both the charge-carrier lifetime and mobility of $In_xGa_{1-x}As$: THz spectroscopy probes the complex, frequency-dependent conductivity on a sub-picosecond time scale without the need for electrical contacts. Thus, it can assess both the charge-carrier mobility and recombination dynamics.

This chapter presents two THz-based studies aimed at controlling and optimising the optoelectronic response of $In_{0.53}Ga_{0.47}As$. First, the influence of Fe dopants on the carrier lifetime and mobility of $In_{0.53}Ga_{0.47}As$ is investigated. Second, the effect of uniaxial strain on the optoelectronic properties is explored. The chapter begins with a brief review of the relevant $In_xGa_{1-x}As$ material properties and prior work, followed by the experimental methods. Next, the results and discussion for the Fe-doped samples are presented, followed by the strain study. Finally, the conclusion brings together the results of both studies and discusses the future outlook for this research.

5.2 $In_xGa_{1-x}As$ Material Properties and Literature Review

$In_xGa_{1-x}As$ is a ternary III–V alloy of GaAs and InAs whose properties can be tuned continuously between the two binaries by adjusting the alloy fraction, x. This chapter focuses on the widely used $In_{0.53}Ga_{0.47}As$ composition, hence the term "InGaAs" is hereafter used to refer exclusively to the $In_{0.53}Ga_{0.47}As$ composition. Additionally, all material properties in this short review are at room temperature, unless stated otherwise.

InGaAs has a direct bandgap of ∼0.75 eV, aligning well with the 1300–1550 nm low-loss fibre-optic transmission regime (photon energies of ∼0.95–0.8 eV) [172]. InGaAs absorbs strongly at 1550 nm, with an absorption coefficient of approximately 8100 cm^{-1} [173]. The electron effective mass (∼0.041 m_e) is much smaller than for holes (heavy-hole effective mass ∼0.46 m_e) [172], which means the electrons dominate the conductivity of InGaAs. This small effective mass facilitates high electron mobilities of approximately 12000 $cm^2V^{-1}s^{-1}$ in high-quality films [174]. This mobility is larger than typical values for high-quality GaAs (∼8000 $cm^2V^{-1}s^{-1}$) [109], which, together with its strong IR absorption, makes InGaAs highly attractive for high-speed IR photodetectors.

However, high-quality InGaAs has a low resistivity (∼0.4 Ωcm) [55] that leads to a significant dark conductivity (conductivity at equilibrium). This background conductivity is detrimental to device performance as it reduces the breakdown electric field and achievable signal-to-noise ratio (SNR) [175]. Ideally, the resistivity of a semiconductor is limited by its intrinsic (no doping) carrier density, n_i, which represents the minimum number of thermally generated carriers. At room temperature (T =300 K), n_i for InGaAs is given by

$$n_i = \frac{1}{\sqrt{2}} \left(\frac{k_B T}{\pi \hbar^2} \right)^{3/2} (m_e^* m_h^*)^{3/4} \exp\left(\frac{-E_g}{2k_B T} \right), \tag{5.1}$$

where k_B is the Boltzmann constant, E_g is the bandgap, and m_e^* and m_h^* are the effective electron and hole masses respectively [80]. Inserting the relevant values for InGaAs ($m_e^* = 0.041 m_e$, $m_h^* = 0.46 m_e$, and $E_g = 0.75$ eV) results in an intrinsic carrier density of $n_i \sim 6.3 \times 10^{11}\,\mathrm{cm}^{-3}$. For a high-quality film with a typical electron mobility of $\mu \sim 12000 \mathrm{cm}^2\mathrm{V}^{-1}\mathrm{s}^{-1}$, the theoretical intrinsic limit for resistivity is $\rho = (q n_i \mu)^{-1} \sim 1000\ \Omega$cm. The fact that literature values for nominally undoped InGaAs are three orders of magnitude less than this limit (∼0.4 Ωcm) indicates that the equilibrium properties are dominated by unintentional background impurities, typically resulting in an n-type carrier concentration of $\sim 10^{15}\ \mathrm{cm}^{-3}$ [55].

Compounding the issue of low resistivity is the relatively long electron lifetime of InGaAs, which often exceeds hundreds of picoseconds [35]. This slow recombination limits the applicability of InGaAs for ultrafast optoelectronic devices, such as THz photoconductive antennas. Consequently, these limitations have motivated significant research efforts into engineering InGaAs to simultaneously reduce its electron lifetime while increasing its resistivity towards the intrinsic limit.

The following section reviews the key research on optimising these properties of InGaAs. Specifically, it covers low-temperature growth of InGaAs, Be-doped InGaAs,

InGaAs/$In_{0.52}Al_{0.48}As$ superlattices, and transition-metal-doped InGaAs. The transition-metal dopants (Fe and Rh) show the most promising properties, with the Fe-dopants low cost making them highly attractive for ultrafast optoelectronic applications. Note that this review is not a comprehensive coverage of all routes to ultrafast electron lifetimes in InGaAs. Other methods have been explored, such as irradiation of InGaAs with high-energy ions, doping with ErAs during growth, or creating ErAs/InGaAs superlattices [176–178]. These topics are well covered in the recent review by Chen *et al.* [35].

5.2.1 Optimising InGaAs Electron Lifetime, Mobility, and Resistivity

Shockley-Read-Hall (SRH) recombination theory predicts an inverse relationship between the charge-carrier lifetime, τ, and the density of charge-carrier traps, N_t

$$\tau = \frac{1}{N_\mathrm{t}\sigma_\mathrm{cc}v_\mathrm{th}}, \tag{5.2}$$

where σ_cc is the carrier capture cross-section, and v_th is the thermal velocity of the carriers [179, 180]. Therefore, a clear pathway to optimising InGaAs for ultrafast applications is to intentionally increase the trap density. Note that the electron lifetime is the critical parameter owing to their small effective mass, hence this review will focus explicitly on the electron properties.

Low-temperature molecular-beam epitaxy (LT-MBE)

LT-MBE of III–V semiconductors has been very successful at introducing defects to reduce charge-carrier lifetimes [181]. In conventional MBE, the substrate is held at a high temperature (∼500-600 °C) to allow deposited adatoms to diffuse to their equilibrium lattice sites, enabling highly stoichiometric growth. In contrast, LT-MBE uses much lower substrate temperatures (∼150-300 °C) to limit surface diffusion, resulting in high densities of point defects, such as group–V antisites and interstitials [181, 182]. For

LT-MBE of InGaAs (LT-InGaAs), these As-antisites (As atom in the expected position of a Ga atom) have a defect energy level slightly less ($< 0.1\,\text{eV}$) than the conduction band minimum of InGaAs [183, 184]. These defects are readily ionised at room temperature, creating As^+ states that can trap electrons.

Early studies of LT-InGaAs by Gupta *et al.* demonstrated the growth process significantly decreased the electron lifetime, with a lifetime of 2.5 ps reported for InGaAs grown on InP at 180 °C [175, 180]. Further studies revealed that the density of ionised As-antisite defects increased as the substrate temperature decreased, resulting in a growth-temperature dependent electron lifetime [183, 185]. Researchers also found that LT-InGaAs became amorphous at substrate temperatures below ∼125 °C, which limited the lifetime reduction possible with just LT-MBE. Additionally, as the defect density increased with decreasing substrate temperature, the electron mobility decreased [175]. However, the most pressing issue with LT-InGaAs is the resistivity: the ionisation of the As-antisites liberates electrons into the conduction band, resulting in a very high n-type conductivity (small dark resistivity) that is further from the intrinsic limit than undoped InGaAs [186]. This low resistivity reduces the SNR of potential LT-InGaAs devices and severely lowers their breakdown electric field. Consequently, other methods must be used in conjunction with LT growth to make it a viable material for device applications.

Beryllium doping

An obvious step to increasing the resistivity of LT-InGaAs is to dope it with an acceptor to compensate for the n-type conductivity and bring its resistivity closer to the intrinsic limit. One of the most widely studied dopants for this purpose is Be [187–190]. Be doping significantly reduces the free electron concentration of LT-InGaAs [186, 189]. Interestingly, scanning tunnelling microscopy has revealed that Be-doped LT-InGaAs has fewer As-antisites than undoped LT-InGaAs. However, the Be doping lowers the Fermi

level of InGaAs, leading to a larger proportion of the As-antisites being ionised. Overall, this effect means Be-doped LT-InGaAs has more ionised As-antisites – the defect that most readily traps electrons – than undoped LT-InGaAs [188]. As a result, Be-doped LT-InGaAs has a shorter electron lifetime than undoped LT-InGaAs, with electron lifetimes of ∼1 ps reported [184, 191]. The lifetime is shorter for higher Be doping concentrations, however the Be dopants also act as scattering centres that lower the electron mobility [35]. Additionally, the Be concentration should be carefully balanced with the background electron concentration – too little leaves a significant n-type conductivity, but too much may lead to p-type conductivity [186, 189] – which can prove technically challenging.

Superlattices

To make fabrication more tolerant, the Be-doped LT-InGaAs can be implemented in superlattices (multilayer heterostructures) of InGaAs and $In_{0.52}Al_{0.48}As$ [184, 186, 189, 192]. $In_{0.52}Al_{0.48}As$ (hereafter, InAlAs) is also lattice-matched to InP and has a much larger bandgap (∼1.47 eV [193]) than InGaAs. Therefore, light between 900 and 1650 nm incident on InGaAs/InAlAs heterostructures will pass through the InAlAs layers and only photoexcite the InGaAs layers. When InAlAs is grown at substrate temperatures of ∼300-500 °C, it forms cluster defects (InAs or AlAs-like regions) with activation energies of approximately 0.7 eV. The conduction band of InAlAs is approximately 0.44 eV above the conduction band of InGaAs, resulting in the cluster defects having an energy level within the bandgap of InGaAs, as depicted in Figure 5.1. When the InAlAs is thin enough – several nanometres such that the InGaAs electron wavefunction overlaps with the InAlAs defect – electrons from the conduction band of InGaAs (or holes from valence band, as the defect is a mid-gap state) can be captured by the InAlAs [193]. Therefore, superlattices of InGaAs/InAlAs can effectively increase the resistivity of InGaAs by removing free charge carriers.

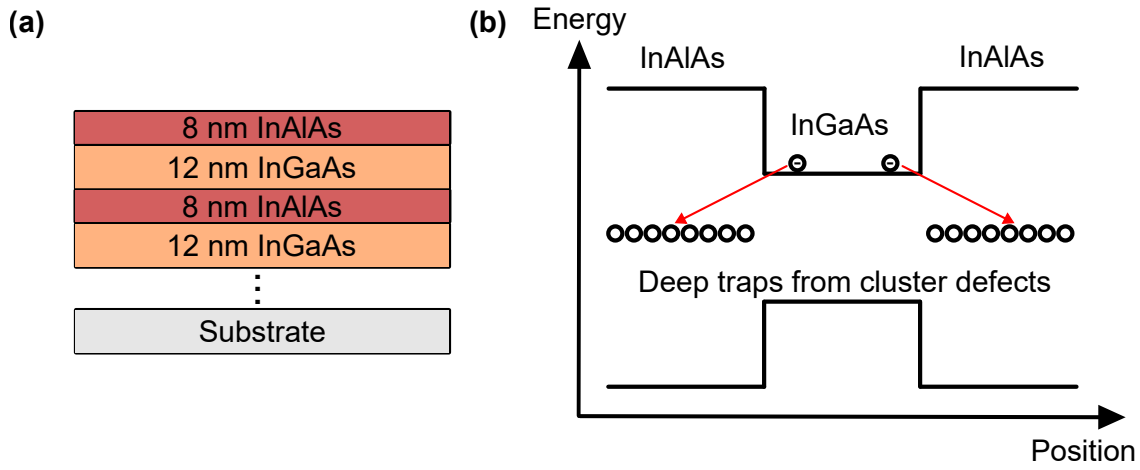

Figure 5.1: (a) Schematic diagram of the InGaAs/InAlAs superlattice. Up to 100 periods are typically used in the full structure [193]. (b) Schematic band-diagram showing the position of the cluster defect states relative to the InGaAs band gap. The InGaAs is thin such that electrons can be captured from the conduction band into the InAlAs trap states.

Such superlattices have been implemented with Be-doped LT-InGaAs as well as undoped InGaAs grown at higher temperatures [194–197]. InGaAs/InAlAs superlattices using Be-doped LT-InGaAs have achieved electron lifetimes as low as 140 fs, however the mobilities were severely reduced to $\sim$200 $cm^2V^{-1}cm^{-1}$ [55]. Other studies found similarly low mobilities as well as resistivity values of $\sim$240 Ωcm [193]. In contrast, superlattices with InGaAs grown at higher temperatures (350–450 °C) have relatively high mobilities of 1500–3000 $cm^2V^{-1}cm^{-1}$, owing to their higher crystallinity, and resistivities of nearly 6000 Ωcm – close to the intrinsic limit for an electron mobility of 1500 $cm^2V^{-1}cm^{-1}$ [193]. Moreover, the superlattices reduce the photoexcited electron lifetime of the undoped InGaAs to $\sim$2 ps [194, 195]. InGaAs/InAlAs superlattice THz PCAs have been reported by many groups [35].

Transition metal doping

Transition metal doping offers an alternative method for reducing the electron lifetime of InGaAs. Transition metal dopants introduce deep energy levels within the bandgap that act as efficient SRH recombination centres, simultaneously reducing the electron

lifetime and increasing the resistivity [55]. Of the transition metal dopants, Fe has been the most extensively studied for InGaAs [198–202].

Fe dopants substitute for In or Ga cations, forming substitutional Fe^{3+} impurities that can capture an electron to form Fe^{2+} [55]. The impurity acts as a deep trap with an energy level approximately 0.39 eV above the valance band maximum – roughly half of the 0.75 eV band gap [200, 201]. Free electrons and holes are rapidly captured by these mid-gap states and cannot be thermally re-excited. As a result, the Fe dopants compensate for the background conductivity and function as ultrafast recombination centres that significantly shorten the electron lifetime of InGaAs.

Fe can be incorporated during epitaxial growth (MBE, MOCVD (metal-organic chemical vapour deposition)) or by ion implantation of already grown InGaAs. Early studies on Fe-ion implantation showed that electron lifetimes as low as 300 fs could be achieved, while increasing the resistivity above the levels of undoped-InGaAs [202]. Suzuki *et al.* demonstrated that Fe-implanted InGaAs could be used in THz PCA detectors pumped by 1550 nm light [203]. However, the ion implantation caused damage to the InGaAs and introduced many scattering centres that reduced the electron mobility to less than 200 $cm^2V^{-1}cm^{-1}$ [202].

Doping Fe into InGaAs during MBE allows for extremely uniform doping distributions without the lattice damage associated with ion implantation. Globisch *et al.* demonstrated Fe-doped InGaAs (InGaAs:Fe) with Fe concentrations between 1×10^{18} and 5×10^{20} cm^{-3} grown by MBE at growth temperatures between 350 and 450 °C [55]. Hall effect and differential transmission (DT) measurements showed the resistivity increased and electron lifetime decreased as the Fe concentration increased, with reported values of ~2000 Ωcm and 300 fs respectively at an Fe concentration of 5×10^{20} cm^{-3}. Moreover, relatively high mobilities of ~900 $cm^2V^{-1}s^{-1}$ were measured despite the large dopant density. Analysis of the InGaAs:Fe suggests that only a small fraction (~0.5%) of

the incorporated Fe is electrically active (forms a substitutional defect) while the remainder form inactive interstitial defects. This low yield explains why such high Fe concentrations are required to push the lifetime to sub-picosecond levels. Globisch *et al.* also fabricated THz PCA detectors from the highest doped InGaAs:Fe samples and recorded an impressive bandwidth of 6 THz and a dynamic range of 95 dB, demonstrating the excellent performance of Fe-doped InGaAs. A later study showed that InGaAs:Fe could be used in fibre-compatible THz transceivers – capable of detection and emission of THz radiation – that is ideal for reflection-mode THz spectroscopy [56].

Other transition metals can be substituted for Fe. For example, Rh dopants in InGaAs form a deep level defect at 0.38 eV below the conduction band minimum, also serving as ultrafast recombination centres [204]. At a doping concentration of $\sim 8\times10^{19}\,\mathrm{cm}^{-3}$, Rh-doped InGaAs grown by MBE has achieved electron lifetimes as short as 220 fs, with a mobility of $1010\,\mathrm{cm}^2\mathrm{V}^{-1}\mathrm{s}^{-1}$ and a high resistivity of $\sim 3200\,\Omega\mathrm{cm}$ – all slight improvements over Fe-doped InGaAs at a doping concentration of $5\times10^{20}\,\mathrm{cm}^{-3}$ [205]. This Rh-doped InGaAs has been utilised in THz PCAs with a record detection dynamic range of 111 dB and bandwidth of 6.5 THz, as well as in efficient THz emitters [36]. Despite the excellent properties of Rh-doped InGaAs, Rh is a significantly more expensive and less available dopant than Fe, limiting the viability of Rh-doped InGaAs devices.

Summary

Overall, many methods have been explored for making InGaAs suitable for ultrafast device applications. Table 5.1 summarises the material properties for each method. Of the different techniques reviewed, MBE-grown InGaAs:Fe is particularly promising owing to its high electron mobility and resistivity, sub-picosecond electron lifetime, and availability as a dopant material. The next steps in the development of InGaAs:Fe is to understand fully how Fe concentration and photoexcited charge-carrier density

impact the material properties. With this information, the ideal material composition for a given application can be readily identified.

5.3 Experimental Methods: OPTP Setup

OPTP spectroscopy was used to study the InGaAs samples in both the Fe-dopant and strain studies after photoexcitation with 1550 nm light. The experiment was setup similarly to the previous chapter (see Section 4.3), except the optical-pump beam from the Ti:sapphire laser was redirected into an optical parametric amplifier (Light Conversion, TOPAS). The TOPAS converted the 800-nm wavelength light into 1550-nm light, and a 1550-nm bandpass filter was placed after the TOPAS to remove any residual wavelengths, as shown in Figure 5.2. There was significant power loss during conversion – the initial ~2 W of 800-nm light entering the TOPAS was reduced to ~60 mW of 1550-nm light. As a result, the photoexcitation fluence on the sample was limited and two different pump beam sizes were required: a small spot (2.8 mm FWHM) to achieve high fluences, and a large one (5.3 mm FWHM) to ensure a highly uniform charge-carrier density at lower fluences. Measurements using the different beam sizes are compared in Appendix A.3 to check that the change in beam size did not significantly impact the results. As for the THz pulse, it was focussed onto the sample with a spot size of 1.3 mm FWHM. Using this system, photoconductivity spectra can be measured by holding the pump-probe delay, Δt_{pp}, constant and measuring the full THz pulse in the time domain. Alternatively, the signal from the THz peak can be tracked as the pump-probe delay changes, thus tracking the decay in photoconductivity over time (see Section 2.2 for details of each measurement). To account for the inherent instabilities in the output of the TOPAS, all measurements were repeated three times. These repeated scans allowed for determination of the average signal and the associated experimental error in all the reported data.

Approach	Electron Lifetime τ_e	Electron Mobility μ ($cm^2V^{-1}s^{-1}$)	Resistivity (Ωcm)	Notes	Key References
Baseline high-quality $In_{0.53}Ga_{0.47}As$	>100 ps	~12000	~0.4	High-quality film grown by MOCVD	[55, 174]
LT-InGaAs	~2.5 ps	Limited by high defect density	—	LT-MBE at 180 °C; limited by poor resistivity	[175]
Be-doped LT-InGaAs	~1 ps	Limited by high defect density	Improved compared to baseline $In_{0.53}Ga_{0.47}As$	Challenging to balance the Be concentration with background conductivity	[184, 191]
InGaAs/InAlAs superlattice (with Be-doped LT-InGaAs)	~140 fs	~200	~240	Very fast τ_e but low μ	[184]
InGaAs/InAlAs superlattice (with undoped InGaAs)	~2 ps	1500–-3000	~6000	High resistivity and μ with τ_e in low-ps range	[193, 194]
InGaAs:Fe (ion-implanted)	~300 fs	<200	~5×10^5 Ω/square	Damage from implantation reduces μ	[202]
InGaAs:Fe (MBE)	~300 fs	~900	~2000	Values for Fe concentration of 5×10^{20} cm^{-3}; ~0.5% of dopants electrically active	[55]
InGaAs:Rh (MBE)	~220 fs	~1000	~3200	Values for Rh concentration of ~8×10^{19} cm^{-3}	[36, 204, 205]

Table 5.1: Electrical properties of InGaAs after different modifications.

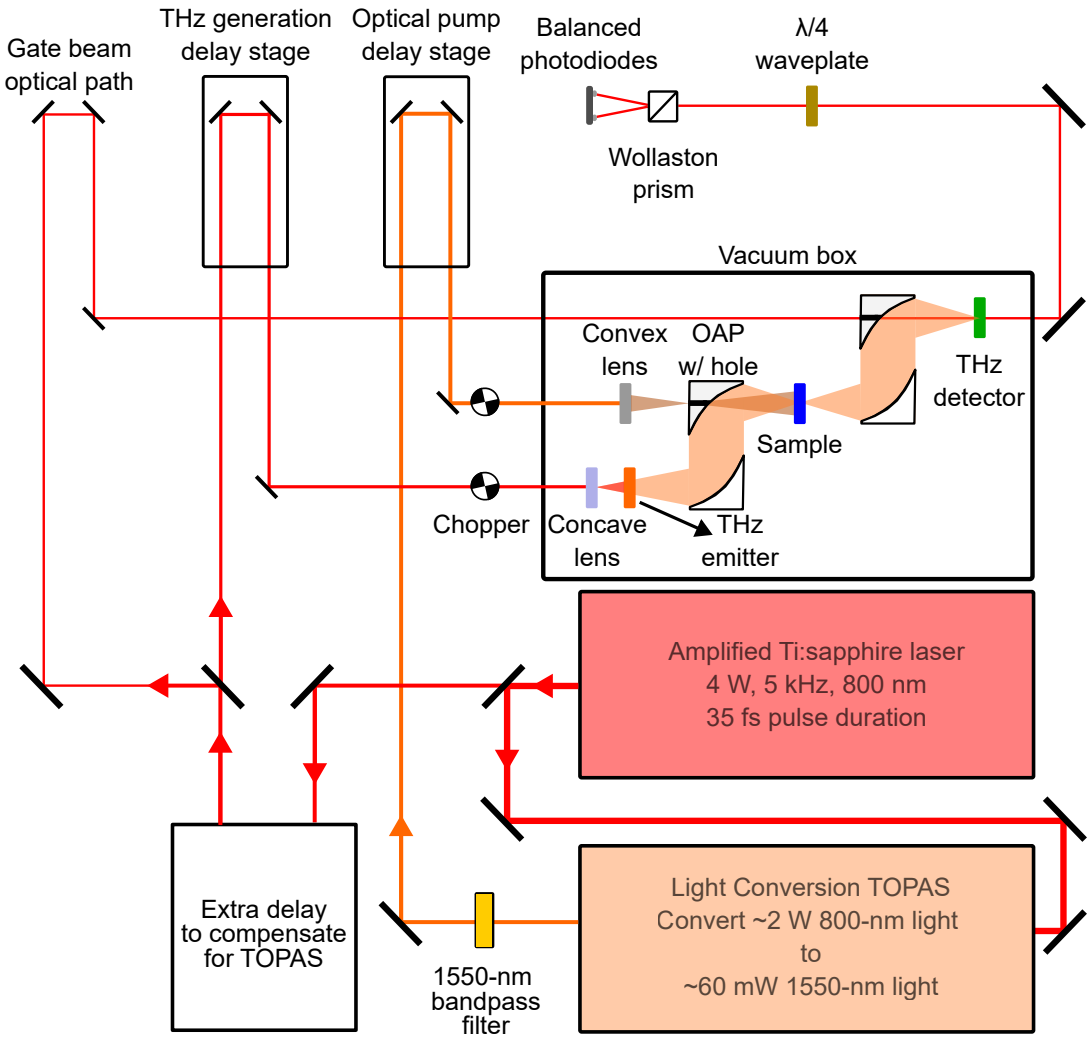

Figure 5.2: Schematic diagram of the OPTP spectroscopy setup with the TOPAS. Arrows indicate the direction of the laser beams along each optical path. See Section 2.2 for further details of the spectrometer.

5.4 Study 1: Characterisation of InGaAs:Fe

InGaAs doped with Fe is a highly promising material for ultrafast optoelectronics that are compatible with fibre-optic systems. Each application that may use InGaAs:Fe will operate at a different charge-carrier density. These changes in carrier density will impact the material properties, and so it is important to have a comprehensive understanding of what the key charge-transport properties (electron lifetime, mobility) are over a range of charge-carrier densities. To address this gap, this section investigates MBE-grown

InGaAs:Fe over a wide range of photoexcitation fluences and Fe-doping concentrations using OPTP spectroscopy. These results form a map of the electron lifetimes and mobilities in the parameter space such that the ideal material for a given application can be selected. The photoexcitation wavelength was 1550 nm to ensure the measurements addressed the most technologically relevant wavelength.

5.4.1 Material Fabrication

The InGaAs samples were grown by my collaborators using gas-source MBE on a $10\times10\,\mathrm{mm}^2$ semi-insulating InP substrate (350-μm thick) at the Fraunhofer Institute for Telecommunications. First, a nominally undoped $In_{0.52}Al_{0.48}As$ buffer layer (660 nm) was grown on the substrate. Next, a thin doped layer of $In_{0.52}Al_{0.48}As$:Fe ($\sim$40 nm) was deposited, followed by 1200 nm of $In_{0.53}Ga_{0.47}As$:Fe. Finally, a capping layer of $In_{0.52}Al_{0.48}As$ ($\sim$20 nm) completed the structure. Note that the $In_{0.52}Al_{0.48}As$ layers were included to protect and passivate the $In_{0.53}Ga_{0.47}As$ top surface. The capping layer plays no part in the photoconductivity signal beyond passivating the $In_{0.53}Ga_{0.47}As$ surface because the energy of the 1550-nm-wavelength photons is much less than the bandgap of $In_{0.52}Al_{0.48}As$. A schematic diagram of the sample structure is presented in Figure 5.3. The full structure is referred to as InGaAs:Fe throughout this chapter.

The samples in this study were analysed by my collaborators with secondary ion mass spectrometry (SIMS) at the Fraunhofer Institute for Applied Solid State Physics. The Fe doping concentrations were: nominally undoped, 1.7×10^{17}, 2.7×10^{17}, 1.1×10^{18}, 3.4×10^{18}, 1.6×10^{19}, 1.5×10^{20}, and $4.6\times10^{20}\,\mathrm{cm}^{-3}$. Each sample is usually referred to by its Fe concentration using the notation $[\mathrm{Fe}] = x\,\mathrm{cm}^{-3}$. For example, the sample with an Fe concentration of $3.4\times10^{18}\,\mathrm{cm}^{-3}$ is typically referenced by $[\mathrm{Fe}] = 3.4\times10^{18}\,\mathrm{cm}^{-3}$.

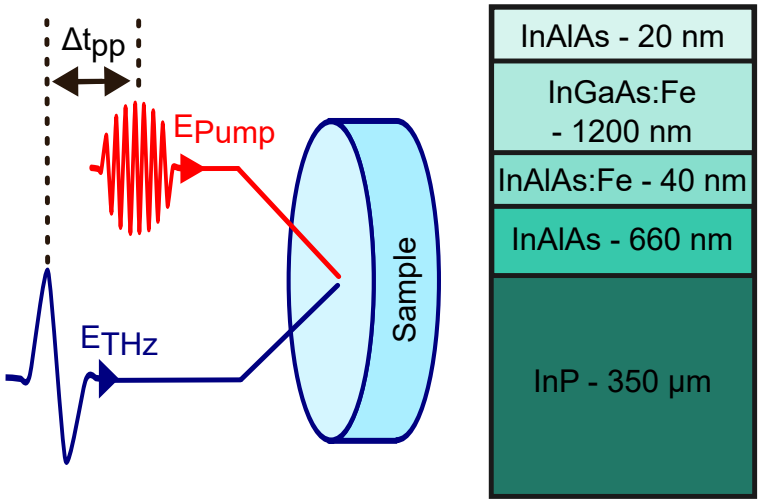

Figure 5.3: Schematic diagram of the InGaAs:Fe sample structure and the OPTP experiment geometry. Δt_{pp} is the time delay between the optical-pump beam (E_{pump}) and THz probe (E_{THz}).

5.4.2 Evaluating Electron Lifetime

Figure 5.4 shows the effect of changing the Fe doping concentration on the electron lifetime of InGaAs:Fe. The photoconductivity decayed faster as [Fe] increased. For example, the photoconductivity of the [Fe] = $4.6\times10^{20}\,cm^{-3}$ sample decayed within a few picoseconds for all photoinjected carrier densities, whereas the [Fe] = $1.1\times10^{18}\,cm^{-3}$ sample decayed much more gradually. These results clearly link the Fe dopant concentration to the trap density (N_t), and demonstrate that the electron lifetime can be tuned by adjusting [Fe].

The photoconductivity decay is dominated by trap-assisted (SRH) capture due to the high density of Fe-induced deep traps, thus higher-order contributions (radiative and Auger recombination) are negligible here. Therefore, the decay rate of the photoinjected carrier density is

$$\frac{dN(t)}{dt} = -kN(t), \tag{5.3}$$

where k is the SRH capture rate constant. Solving the above rate equation results in

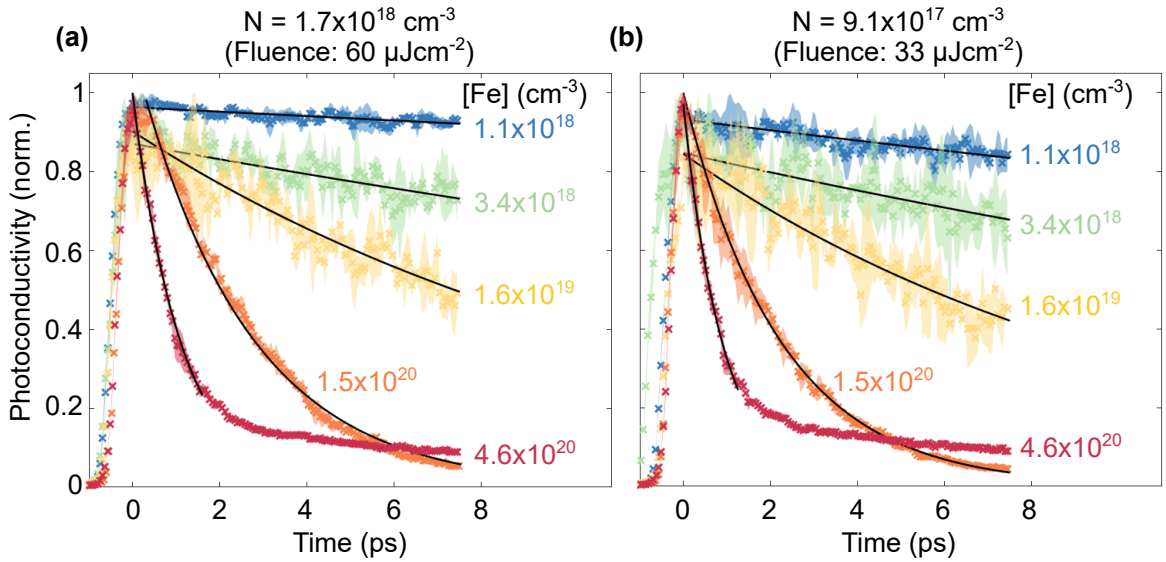

Figure 5.4: Photoconductivity of InGaAs:Fe as a function of time after photoexcitation using a 60 μJcm^{-2} (a) and 33 μJcm^{-2} (b) excitation beam (initial photoexcited carrier density, N, of 1.7×10^{18} and 1.9×10^{17} cm^{-3} respectively). The different coloured data correspond to different Fe doping concentrations, [Fe], as indicated on the figure. The black lines are fits to a monoexponential decay and the semi-transparent regions are the standard deviation of three repeated measurements. The fitting window was selected as the best fit (highest R^2 coefficient of determination) that covered at least 70 % of the decay in the photoconductivity amplitude. Curves that did not decay at least 70 % within the first 7.5 ps used the full 7.5 ps fitting window.

$$N(t) = N_0 \exp(-t/\tau), \tag{5.4}$$

where N_0 is the initial photoinjected carrier density immediately after photoexcitation and τ is the (trap-limited) lifetime. The photoconductivity is proportional to the carrier density and mobility ($\Delta\sigma(t) \propto qN(t)\mu(t)$). Assuming the mobility is roughly constant, the photoconductivity exhibits the same monoexponential decay as $N(t)$.

Monoexponential fits were individually applied (not globally) to the photoconductivity decay data to extract the electron lifetimes. Note that fits were only applied to the first ~7.5 ps after photoexcitation to avoid a back-reflection artefact (see Appendix A.2), which made it too challenging to fit the longest-lived samples (nominally undoped and [Fe] = 1.7×10^{17} cm^{-3}). The electron lifetimes for all other samples at each N are presented in Table 5.2. Notably, sub-picosecond lifetimes were achieved in both

samples with Fe concentrations above $1\times10^{20}\,\mathrm{cm}^{-3}$ at all N below $\sim3.6\times10^{17}\,\mathrm{cm}^{-3}$ (corresponding to an excitation fluence of $\sim13\,\mu\mathrm{Jcm}^{-2}$), demonstrating the suitability of InGaAs:Fe for ultrafast applications.

The electron lifetimes reported here are slightly longer than those in Ref. [55] for similarly prepared InGaAs:Fe at comparable Fe concentrations and photoexcited carrier densities (e.g., $\sim$600 fs at $[\mathrm{Fe}] = 4.6\times10^{20}\,\mathrm{cm}^{-3}$ for $N = 3.6\times10^{16}\,\mathrm{cm}^{-3}$ here, and $\sim$300 fs at $[\mathrm{Fe}] = 5\times10^{20}\,\mathrm{cm}^{-3}$ for $N = 5\times10^{16}\,\mathrm{cm}^{-3}$ in Ref. [55]). This difference is likely related to fundamental differences in the measurement techniques: Ref.[55] used DT to measure the electron lifetime, while OPTP spectroscopy is used here. OPTP was used to monitor the photoinduced change of the transmitted THz field at the time-domain peak – this is effectively a spectrally weighted measure of the photoconductivity averaged through the full 1200 nm film thickness. As the charge-carrier density and/or mobility decreases after excitation, the photoconductivity decays and the transmitted THz field recovers to its equilibrium value. In contrast, DT measurements track the transmission of an optical probe after photoexcitation. This probes the recovery of the band-edge absorption (Pauli blocking) – transmission of the optical probe increases immediately after excitation because band-edge states are occupied, and then transmission decreases as states near the conduction-band minimum (Γ point) empty, mainly due to trapping and recombination.

Four effects can bias OPTP toward longer time constants than DT. Firstly, hot carriers (carriers excited above the band edge) have a reduced mobility that increases as they rapidly cool (typical timescale of hundreds of femtoseconds [110]). This increase in $\mu(t)$ can partially compensate for the drop in $N(t)$, thus slowing the apparent photoconductivity decay and extending the extracted lifetime from OPTP measurements. Secondly, DT at 1550 nm is strongly weighted towards the sample surface due to optical absorption, whereas the THz pulse probes an average over the full film. Hence, any surface deviations, such as an increased trap density, contribute more to the DT signal than OPTP. Thirdly,

[Fe] (cm^{-3})	τ (ps)						
	1.8×10^{16} ($0.7\,\mu J\,cm^{-2}$)	3.6×10^{16} ($1.3\,\mu J\,cm^{-2}$)	9.0×10^{16} ($3\,\mu J\,cm^{-2}$)	1.8×10^{17} ($6\,\mu J\,cm^{-2}$)	3.6×10^{17} ($13\,\mu J\,cm^{-2}$)	9.1×10^{17} ($33\,\mu J\,cm^{-2}$)	1.7×10^{18} ($60\,\mu J\,cm^{-2}$)
2.7×10^{17}	25 ± 4	36 ± 7	70 ± 10	60 ± 10	69 ± 3	300 ± 100	300 ± 300
1.1×10^{18}	9 ± 1	13 ± 2	19 ± 3	28 ± 4	40 ± 10	70 ± 10	170 ± 40
3.4×10^{18}	6.6 ± 0.5	6.5 ± 0.5	14 ± 1	22 ± 4	27 ± 4	34 ± 5	43 ± 5
1.6×10^{19}	1.35 ± 0.08	1.7 ± 0.2	2.5 ± 0.2	5.3 ± 0.6	7.7 ± 0.5	10.8 ± 0.6	12.5 ± 0.8
1.5×10^{20}	0.75 ± 0.04	0.65 ± 0.06	0.69 ± 0.03	0.7 ± 0.1	1.04 ± 0.06	2.24 ± 0.02	2.55 ± 0.05
4.6×10^{20}	0.55 ± 0.06	0.61 ± 0.07	0.62 ± 0.05	0.66 ± 0.09	0.65 ± 0.09	0.92 ± 0.03	1.10 ± 0.05

Table 5.2: Electron lifetime, τ_e, of InGaAs:Fe for different [Fe] and photoinjected charge-carrier densities (excitation fluences). Values were extracted from monoexponential fits to the data, like those shown by the black lines in Figure 5.4. A photoexcitation spot size of 2.8 mm FWHM was used to reach fluences of 33 and 60 μJcm^{-2}, while the lower fluences were achieved with the larger spot size of 5.3 mm FWHM. Errors were calculated using fits to three separate scans under each set of conditions.

monitoring the peak of the THz transmission emphasises the low–mid THz frequencies, which can reduce the contribution of high frequency changes at early times (charge-carrier thermalisation) and thus the influence of fast components on the fitted photoconductivity. Finally, sample-to-sample variation in the density of Fe dopants and the proportion that are electrically active can shift the electron lifetime. Taken together, these factors account for the slightly longer OPTP-derived electron lifetimes. Despite these differences, the central conclusion of sub-picosecond dynamics at high Fe-doping concentrations is consistent across both studies [55].

The electron lifetime results in Table 5.2 are summarised in Figure 5.5. As indicated by the dashed line, the lifetimes are reasonably close to an inverse proportionality to the Fe doping concentration, as predicted by SRH recombination theory (Equation 5.2) [179]. The slight offset to a perfect $1/x$ relationship likely arises from three factors: (i) the long lifetimes are underestimated as the exponential fits were restricted to the first $\sim$7.5 ps; (ii) short lifetimes are overestimated as explained in the previous paragraph; (iii) the proportion of electrically active dopants may decrease as more Fe is introduced, thus a linear increase in doping concentration is not a linear increase in trap density.

The electron lifetimes generally increased with charge-carrier density. This effect can be explained in terms of trap filling: upon photoexcitation, the free electrons are rapidly trapped by the Fe impurities, but recombination at the trap occurs on a longer timescale. Thus, traps become filled and no longer participate in carrier capture until recombination occurs, resulting in an increase in the effective electron lifetime [55]. Unfortunately, the TOPAS limited the achievable fluences in these experiments, and so a full study of the saturation effects could not be conducted.

While Fe doping sharply reduced the electron lifetime in InGaAs, high-speed opto-electronics also require high carrier mobilities. To assess the impact of Fe doping on the

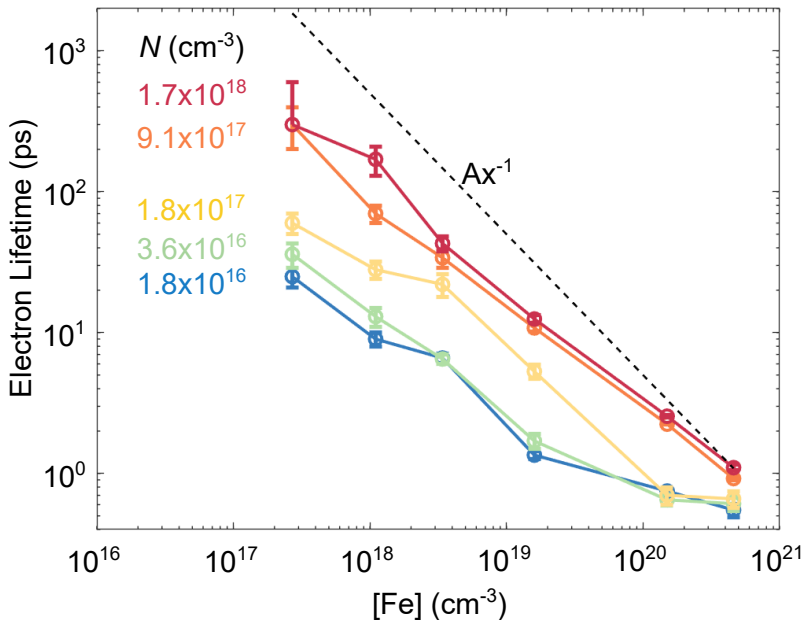

Figure 5.5: Electron lifetimes extracted from the exponential decay model fits for selected photoinjected charge-carrier density, N, and [Fe]. The dashed line shows an inverse relationship, while the solid lines are guides to the eye.

electron mobility, a second series of OPTP measurements were conducted with the pump-probe delay time (Δt_{pp}) fixed, and the full THz pulse measured in the time-domain. With this data, the photoconductivity spectra could be calculated using the thin-film analysis described in Section 2.6.2. It is important that the THz pulse probes a highly uniform charge-carrier density at the sample [19], therefore these measurements only used the larger optical-pump beam size of 5.3 mm FWHM. Consequently, the initial photoinjected carrier densities were restricted to $\sim 5.3 \times 10^{17}$ cm^{-3} and below (fluences of 19 μJcm^{-2} and below).

Figure 5.6 shows representative photoconductivity spectra for several InGaAs:Fe samples measured 1 ps after photoexcitation. The spectra exhibit a characteristic Drude shape across all doping levels: the real and imaginary parts of the conductivity remain positive and intersect at a non-zero frequency. The crossing point shifts to higher frequencies with increasing Fe concentration, indicating increased scattering and hence reduced electron mobilities. The spectra were fitted to the Drude model (Equation 2.51)

using a least squares fitting algorithm. The extracted electron mobilities are tabulated in Table 5.3 and Figure 5.7 (a) plots the relationship between electron mobility and [Fe] for several charge-carrier densities.

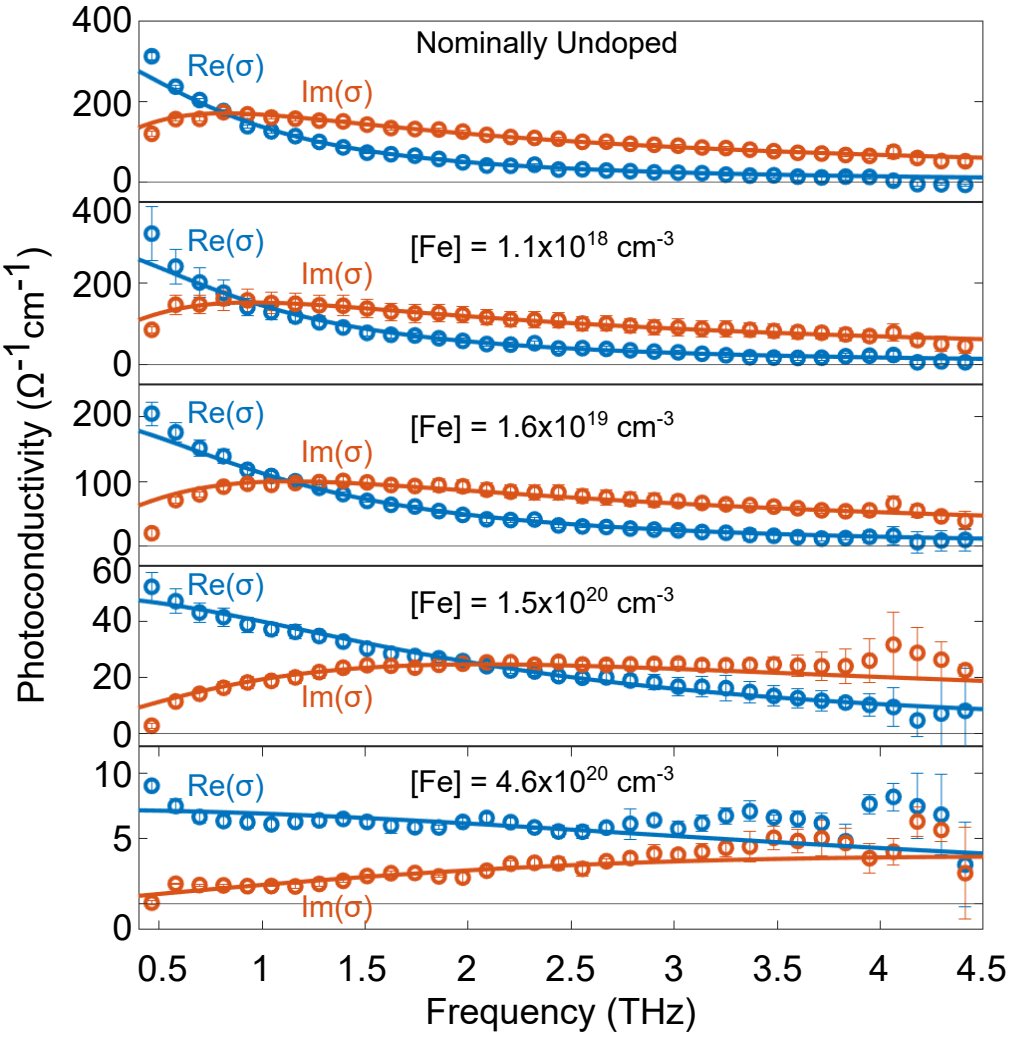

Figure 5.6: THz photoconductivity spectra of InGaAs:Fe samples at different [Fe]. The initial average photoexcited charge-carrier density was $N = 5.3{\times}10^{17}\,\mathrm{cm}^{-3}$ (excitation fluence of $19\,\mu\mathrm{Jcm}^{-2}$). The solid lines are fits to the Drude model (Equation 2.51). All spectra were measured at a pump-probe delay of 1 ps. Errors were calculated from the standard deviation of three separate measurements under the same conditions.

Very high electron mobilities over $10000\,\mathrm{cm}^2\mathrm{V}^{-1}\mathrm{s}^{-1}$ were measured in the nominally undoped InGaAs, which agrees well with literature values for high-quality InGaAs films [174], demonstrating the quality of the InGaAs growth process and validity of the THz analysis. The mobility remained high as [Fe] increased to $\sim 1{\times}10^{18}\,\mathrm{cm}^{-3}$, but proceeded

[Fe] (cm^{-3})	μ ($cm^2V^{-1}s^{-1}$)					
	1.8×10^{16} ($0.7\,\mu J\,cm^{-2}$)	3.6×10^{16} ($1.3\,\mu J\,cm^{-2}$)	9.0×10^{16} ($3\,\mu J\,cm^{-2}$)	1.5×10^{17} ($5\,\mu J\,cm^{-2}$)	3.1×10^{17} ($11\,\mu J\,cm^{-2}$)	5.3×10^{17} ($19\,\mu J\,cm^{-2}$)
Undoped	10200 ± 200	10200 ± 200	9800 ± 100	9300 ± 100	8400 ± 100	8300 ± 100
1.7×10^{17}	10800 ± 500	10700 ± 300	9600 ± 100	9200 ± 200	8600 ± 500	8300 ± 700
2.7×10^{17}	10700 ± 200	10800 ± 100	9500 ± 400	9600 ± 300	8600 ± 300	8300 ± 300
1.1×10^{18}	9500 ± 400	10400 ± 700	8700 ± 200	8500 ± 200	7700 ± 300	7000 ± 1000
3.4×10^{18}	7200 ± 300	8500 ± 100	8000 ± 600	7600 ± 900	9000 ± 1000	7700 ± 300
1.6×10^{19}	6200 ± 900	5800 ± 200	6100 ± 200	5600 ± 200	5700 ± 100	6000 ± 200
1.5×10^{20}	3000 ± 400	2400 ± 200	2500 ± 200	2900 ± 100	2800 ± 100	3300 ± 100
4.6×10^{20}	2100 ± 700	1500 ± 100	1300 ± 200	1200 ± 200	1200 ± 100	1400 ± 100

Table 5.3: Electron mobilities of InGaAs:Fe samples extracted from Drude model fits (Equation 2.51) to THz photoconductivity spectra measured 1 ps after photoexcitation. The average photoinjected charge-carrier densities immediately after excitation are listed along with the excitation fluences. Appendix A.4 lists the charge-carrier densities at the time of measurement, accounting for trapping within 1 ps. Errors were calculated as the standard deviation of three measurements under the same conditions.

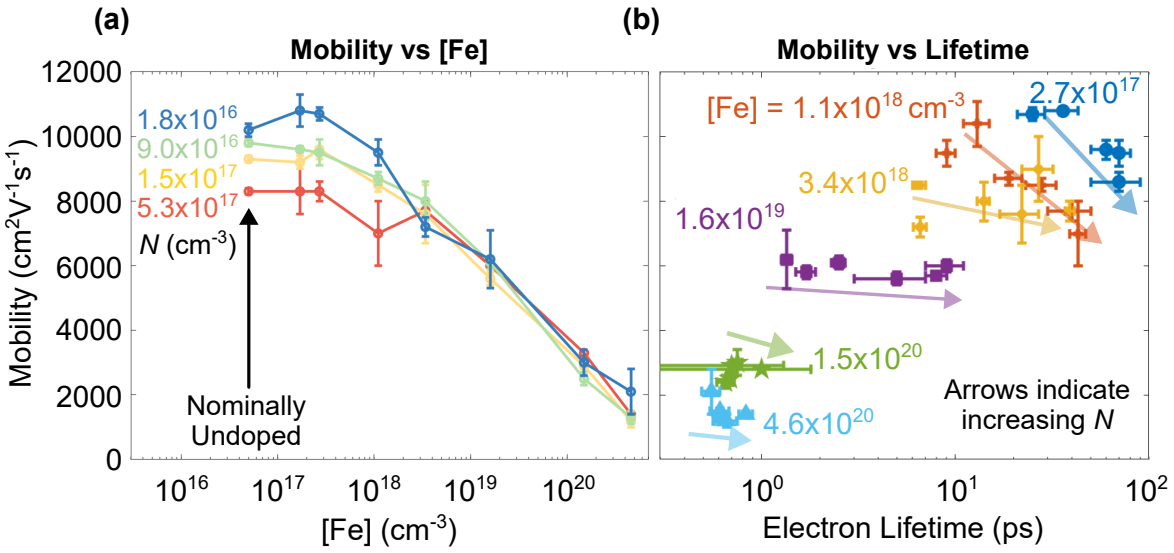

Figure 5.7: (a) Electron mobilities of InGaAs:Fe samples at different photoinjected charge-carrier densities, N, as [Fe] is varied. The solid lines are guides to the eye. The lowest [Fe] data point represents the nominally undoped sample. (b) Summary of the electron lifetimes and mobilities for each InGaAs:Fe sample that both properties could be measured from. Each colour/data-point shape indicates a different [Fe], as shown by the numbers in the figure. The different points of the same colour/shape correspond to the properties at a different N. The arrows indicate the trend of increasing N for each [Fe].

to decrease quickly as more Fe was incorporated, with the highest doping concentration of [Fe] = $4.6\times10^{20}\,\mathrm{cm}^{-3}$ exhibiting a mobility between ~1000–2000 $\mathrm{cm}^2\mathrm{V}^{-1}\mathrm{s}^{-1}$. These results are consistent with Fe dopants acting as scattering centres that reduce mobility.

Higher photoexcitation fluences generally led to reduced electron mobilities. This effect was most pronounced in the low-[Fe] samples and may arise from electrons occupying higher-energy states in the conduction band when the carrier density is high. In InGaAs, the conduction band is non-parabolic, so electrons at higher energies experience increased effective masses that reduce their mobility [206–208]. This effect is less prominent in the high-[Fe] samples as the excited charge-carrier density is significantly lower 1 ps after photoexcitation than in the lower-[Fe] samples owing to the rapid charge trapping (see Appendix A.4).

Figure 5.7 (b) combines the electron lifetime and mobility data for each doping concentration and photoinjected charge-carrier density. The arrows indicate the trend

of increasing electron lifetime and decreasing mobility as N increases. These results map out the properties of InGaAs:Fe, illustrating the trade-off between electron mobility and lifetime. Importantly, these results show an Fe concentration of $1.5\times10^{20}\,\mathrm{cm}^{-3}$ can achieve sub-picosecond lifetimes while retaining mobilities above $\sim$2500 $\mathrm{cm}^2\mathrm{V}^{-1}\mathrm{s}^{-1}$ – priming it for high-speed applications that require a balance of ultrafast response time and rapid charge transport.

5.5 Study 2: Effect of Mechanical Strain on InGaAs

The previous section demonstrated that Fe doping is a powerful mechanism for tuning the optoelectronic properties of InGaAs. This section examines a complementary tuning tool: strain. By definition, strain, ε, is the fractional change in the lattice constant, a, of a material: $\varepsilon = \Delta a/a$. The electronic band structure is determined by the crystal lattice, therefore even modest amounts of strain can strongly impact the optoelectronic properties of the material. For example, strain can break crystal symmetries to lift degeneracies, alter band curvatures, and shift the band edges, all of which changes the effective mass, scattering rate, and bandgap [209].

Strain engineering is used extensively in both research and industry. In silicon CMOS, biaxial and uniaxial strain have been leveraged to increase the carrier mobility of n- and p-type MOSFETs, raising the drive current without increasing leakage current or overhauling the fabrication process [210]. Beyond Si, strain has improved performance across a diverse range of systems, including enhancing electron mobility in GaAs nanowires [155], raising the superconductive critical temperature of Sr_2RuO_4 [211], and inducing a direct bandgap in Ge to enable lasing [212]. The success of strain for enhancing material properties, together with the significant interest in flexible electronics, motivates this targeted study of strain in InGaAs.

Several studies have explored strain in $In_xGa_{1-x}As$. One strategy to implement strain is through lattice-mismatch, where $In_xGa_{1-x}As$ is grown on/against a material with a different lattice constant. Ponomarev *et al.* used lattice-mismatched $In_{0.38}Al_{0.62}As$ in their InGaAs/$In_xAl_{1-x}As$ superlattices and observed a decrease in the InGaAs bandgap, as well as increased interface roughness that reduced the electron lifetimes compared to non-strained superlattices [195]. Alternatively, the alloy fraction of $In_xGa_{1-x}As$ can be changed such that it is not lattice matched to InP. Kuo *et al.* reported how the strain induced by changing the composition of $In_xGa_{1-x}As$ on InP shifted the bandgap [213]. However, these composition changes also change the interface quality and material properties, making it challenging to attribute any changes solely to strain. A more direct approach is to apply external stress to the material, for example through bending. Shi *et al.* studied InGaAs HEMTs and found only small changes in the device performance under strain [214]. However, this study explored strain of less than 0.5% and focussed on the device properties instead of the response of bare InGaAs.

To isolate the effects of strain in InGaAs, this section investigates the effect of uniaxial bending on the optoelectronic properties of undoped, lattice-matched $In_{0.53}Ga_{0.47}As$ (InGaAs) on flexible PET substrates. The strained InGaAs is probed with OPTP spectroscopy to obtain the electron mobility and lifetime without contacts or modifying the sample strain. X-ray diffraction (XRD) spectroscopy is utilised to confirm the degree of strain in the InGaAs films. This approach allows for the strain response of InGaAs to be quantified and for its potential as a complementary tuning mechanism to Fe doping to be evaluated. The following sections describe the sample fabrication, method for controlling the applied strain, XRD results, and THz spectroscopy characterisation of the strained InGaAs.

5.5.1 Straining InGaAs on PET

InGaAs thin-films were grown by MOCVD at the Australian National University by Dr. Tuomas Haggren. Full details of the fabrication are available in Appendix A.5. Briefly, $In_{0.53}Ga_{0.47}As$ was grown on an InP substrate before being hot embossed onto a film of PET. The InP was etched away, leaving an InGaAs film on a flexible PET substrate. Two samples were studied; one with a 400-nm-thick InGaAs layer, and the other with a 620-nm-thick InGaAs layer. The PET was approximately 150 μm thick. Figure 5.8 (a) shows a schematic of the sample geometry and a photograph of the 400-nm-thick InGaAs on PET sample.

The sample was strained by putting it into a sample holder that bends it to a controlled radius of curvature. See Appendix A.6 for full details of the sample holder design. Both tensile and compressive strain could be achieved with this approach by flipping the sample holder. Figure 5.8 (b) illustrates the compressive (ε_C) and tensile (ε_T) strain experiment geometries, and (d) shows a photograph of the sample holder for a radius of curvature of 12 mm ($R_C = 12$ mm). The InGaAs film was always oriented outward, such that XRD and THz spectroscopy probed a top layer of InGaAs and a bottom layer of PET.

The amount of strain the InGaAs experiences can be calculated by considering the InGaAs and PET as a composite beam. When the beam is bent like in Figure 5.8 (c), the bottom surface is compressed (ε_C) while the top surface is extended (ε_T). Along some arc between the these surfaces, the beam has the same length as it would at equilibrium (no applied stress) – this arc is the neutral axis (NA). All points on one side of the NA are under compressive strain, while all points on the other are under tensile strain. The strain at a certain radius is given by its strained length divided by its unstrained length (length at NA). Assuming the arc of the bent beam covers an angle θ and the radius of curvature at the NA is R_{NA}, then the strain along an arc some distance x from the neutral axis is

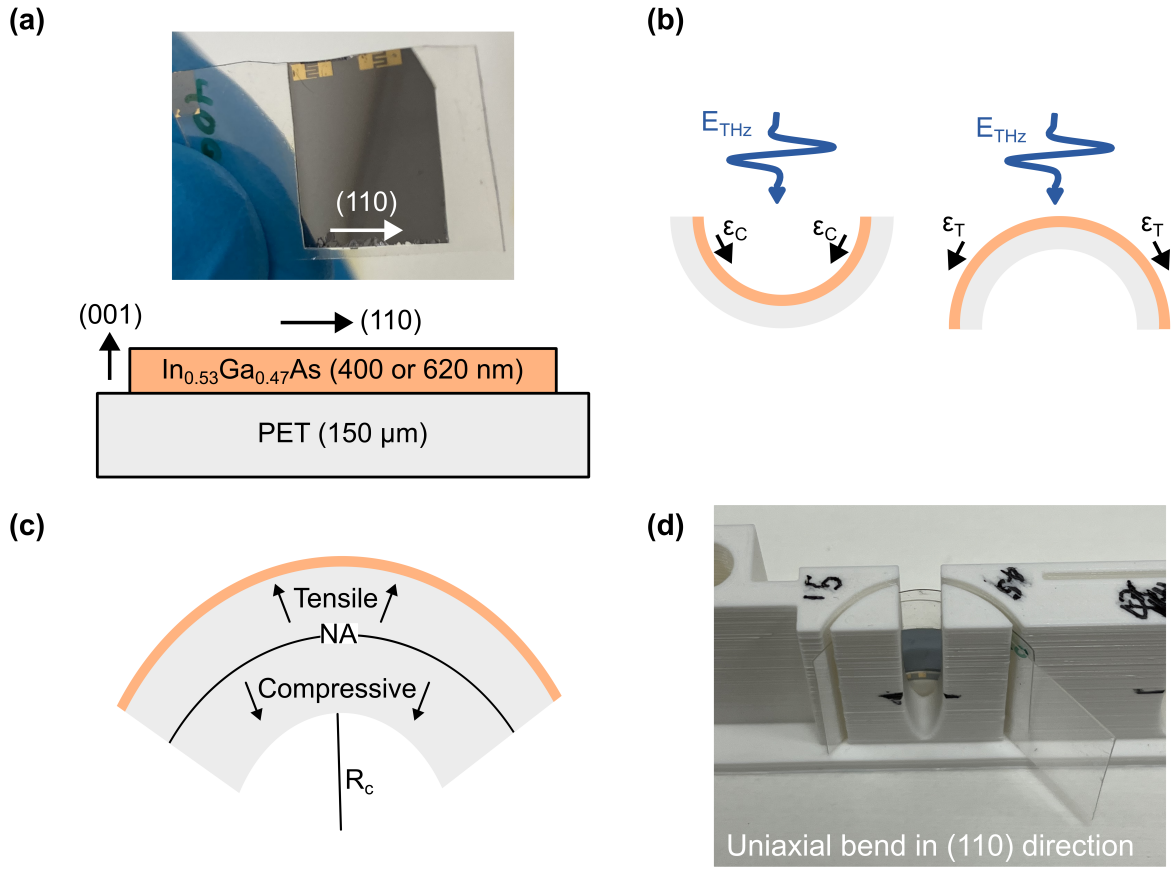

Figure 5.8: (a) (top) Photograph of the 400-nm-thick InGaAs on PET sample with the (110) plane highlighted. (bottom) Schematic diagram of the InGaAs on PET sample structure. (b) Geometry with the InGaAs layer under compressive strain (ε_C) and tensile strain (ε_T) relative to the THz pulse during OPTP spectroscopy. (c) Schematic of the effect of bending the sample to a radius of curvature R_C. The neutral axis (NA) has the same length as the unstrained sample. All points on one side of the NA are under compressive strain whereas all points on the opposite side are under tensile strain. (d) Photograph of the sample holder used to bend the InGaAs on PET during measurement. This holder has a 12 mm radius of curvature.

$$\varepsilon(x) = \frac{\theta(R_{\mathrm{NA}} + x) - \theta R_{\mathrm{NA}}}{\theta R_{\mathrm{NA}}} = \frac{x}{R_{\mathrm{NA}}}. \tag{5.5}$$

The radius of curvature at the NA can be calculated by ensuring the zero net axial force in the beam: $\int Y\varepsilon\, dA = 0$, where Y is Young modulus for the material and A is the cross-sectional area. Assuming that the InGaAs and PET have the same width, the radius of curvature for the NA of the InGaAs on PET samples is given by

$$R_{\mathrm{NA}} = R_C + \frac{Y_s t_s(t_s/2) + Y_f t_f(t_s + t_f/2)}{Y_s t_s + Y_f t_f}, \tag{5.6}$$

where Y_i are the Young's moduli of the PET ($Y_s \approx 3\,\text{GPa}$ [215]) and InGaAs film ($Y_f \approx 60\,\text{GPa}$ [216]) and t_i are the thicknesses of the PET ($t_s \approx 150\,\mu\text{m}$) and InGaAs ($t_f = 400\,\text{or}\,620\,\text{nm}$) [217]. Substituting these values into Equation 5.6 gives $R_{\text{NA}} \approx R_C + 79\,\mu\text{m}$ for the 400-nm-thick InGaAs and $R_{\text{NA}} \approx R_C + 81\,\mu\text{m}$ for the 620-nm-thick InGaAs. This places the NA near the centre of the PET, but slightly closer to the InGaAs layer, as the InGaAs is much stiffer than the PET (greater Young's modulus). Thus, the entire InGaAs film experiences the same kind of strain when bent in the sample holder.

A series of sample holders were created, covering radii of curvature from 5 mm to 12 mm, with an extra holder created to keep the film flat ($R_C = \infty$). The holders were designed such that their inner radius was $R_C - 0.5\,\text{mm}$ and outer radius $R_C + 0.5\,\text{mm}$, allowing the InGaAs on PET to slide in-between the two surfaces and be bent to the target R_C. Using the different R_C along with R_{NA} and Equation 5.5, the amount of strain in the InGaAs films can be calculated.

Table 5.4 lists the calculated strain in each InGaAs sample for each sample holder radius of curvature. Both the outer and inner surfaces of the InGaAs are included in the results to emphasise that the strain is approximately constant across the thin film. Tensile and compressive strain have the same magnitude but opposite sign – in this study, positive values indicate tensile strain, whereas negative values are compressive strain. The applied strain ranges from ∼0.5% to ∼1.4%, covering a modest range that exceeds that of previous studies on external strain in InGaAs [214].

5.5.2 X-ray Diffraction

Strain was verified by symmetric θ–2θ XRD on a Rigaku Smartlab diffractometer using a Cu source and Ge monochromator to select the Kα_1 line (wavelength $\lambda = 1.54059\,\text{Å}$). InGaAs has a zinc-blende crystal structure, thus the (001) reflection is forbidden [218]. The first allowed reflection along the growth direction is the (002) reflection. The XRD scans

R_C (mm)	% strain in 400 nm film		% strain in 620 nm film	
	Inner surface	Outer surface	Inner surface	Outer surface
5	1.402	1.410	1.363	1.375
6	1.171	1.178	1.139	1.149
7	1.006	1.011	0.978	0.987
8	0.881	0.886	0.857	0.865
9	0.784	0.789	0.763	0.769
10	0.706	0.710	0.687	0.693
11	0.643	0.646	0.625	0.631
12	0.589	0.593	0.573	0.578

Table 5.4: Surface strain (%) at the inner (contacted to PET) and outer surfaces of the InGaAs film for the two film thicknesses.

covered $2\theta = 27$–$34°$, ensuring the InGaAs (002) reflection near 30.4° was resolved [219]. In a symmetric scan, the scattering vector lies in the instrument's scattering plane and is parallel to the sample's surface normal. The InGaAs film is single-crystal, hence the (002) peak only appears when the surface normal is in the scattering plane. Under strain, the bent InGaAs has its surface normal rotated about the bend axis, thus the sample was rotated about its normal such that the bend axis was in the scattering plane. The (002) peak signal was maximised when the sample was correctly rotated.

The position of the (002) peak relates to the interplanar spacing, d_{002}, via Bragg's law:

$$n\lambda = 2d\sin(\theta), \tag{5.7}$$

where n is an integer for the reflection order (here $n = 1$), and θ is the angle of the x-rays relative to the lattice plane. The out-of-place lattice constant of InGaAs, a, is then given by $a = 2d_{002}$. The resulting out-of-plane strain ($\varepsilon_{001} = \Delta a/a$) was converted to the strain in the (110) direction using

$$\varepsilon_{110} = \varepsilon_{001}\frac{\frac{s_{11}+s_{12}}{2} + \frac{s_{44}}{4}}{s_{12}} \approx -1.88\,\varepsilon_{001}, \tag{5.8}$$

where s_{ij} are components of the cubic compliance tensor (inverse of the elasticity tensor) [220]. See Appendix A.7 for details of the strain conversion. This relation means that an out-of-plane compression corresponds to extension along the (110) direction of nearly double the magnitude. Due to time and space constraints, XRD was only performed under tensile strain with the 400-nm film. The same alignment protocol was used for all bending radii.

Figure 5.9 (a) shows wide θ–2θ scans for 400-nm InGaAs on PET at different bend radii, along with a scan of bare PET. PET exhibits a broad amorphous feature around 20–30°, and the high-angle tail is visible in each scan [221]. All InGaAs scans display a sharp peak near $2\theta = 30.4°$, which is assigned to the (002) reflection of InGaAs. Panel (b) zooms on the region around the (002) peak. The peak shifts to higher scattering angles as the radius of curvature decreases, indicating smaller d_{002} – consistent with out-of-plane compression when the sample is under tensile strain along the (110) plane. Note that the measurements were repeated to ensure the peak positions were reproducible and not a result of experimental error or damage to the sample.

The scattering angle of the peak was determined by fitting to a Gaussian profile and then converted to d_{002} using Bragg's law. For the flat holder ($R_C = \infty$), the peak at $2\theta \approx 30.4°$ gives $d_{002} \approx 2.94\,\text{Å}$, which corresponds to a lattice constant of $a \approx 5.887\,\text{Å}$ – reasonably close to the literature value of $a \approx 5.65\,\text{Å}$ for $In_{0.53}Ga_{0.47}As$ [219]. The out-of-plane strain was calculated as the relative change in d_{002} compared to the flat case, and then converted to in-plane strain along (110) using Equation 5.8. Figure 5.9 (c) plots both the out-of-plane and in-plane strain for each bending radius.

The measured in-plane strain along the (110) direction is approximately half the expected theoretical value calculated in Table 5.4. This discrepancy between theory and experiment is primarily attributed to the formation of microcracks within the brittle InGaAs layer as it reaches its critical strain limit (fracture toughness) [222]. Such

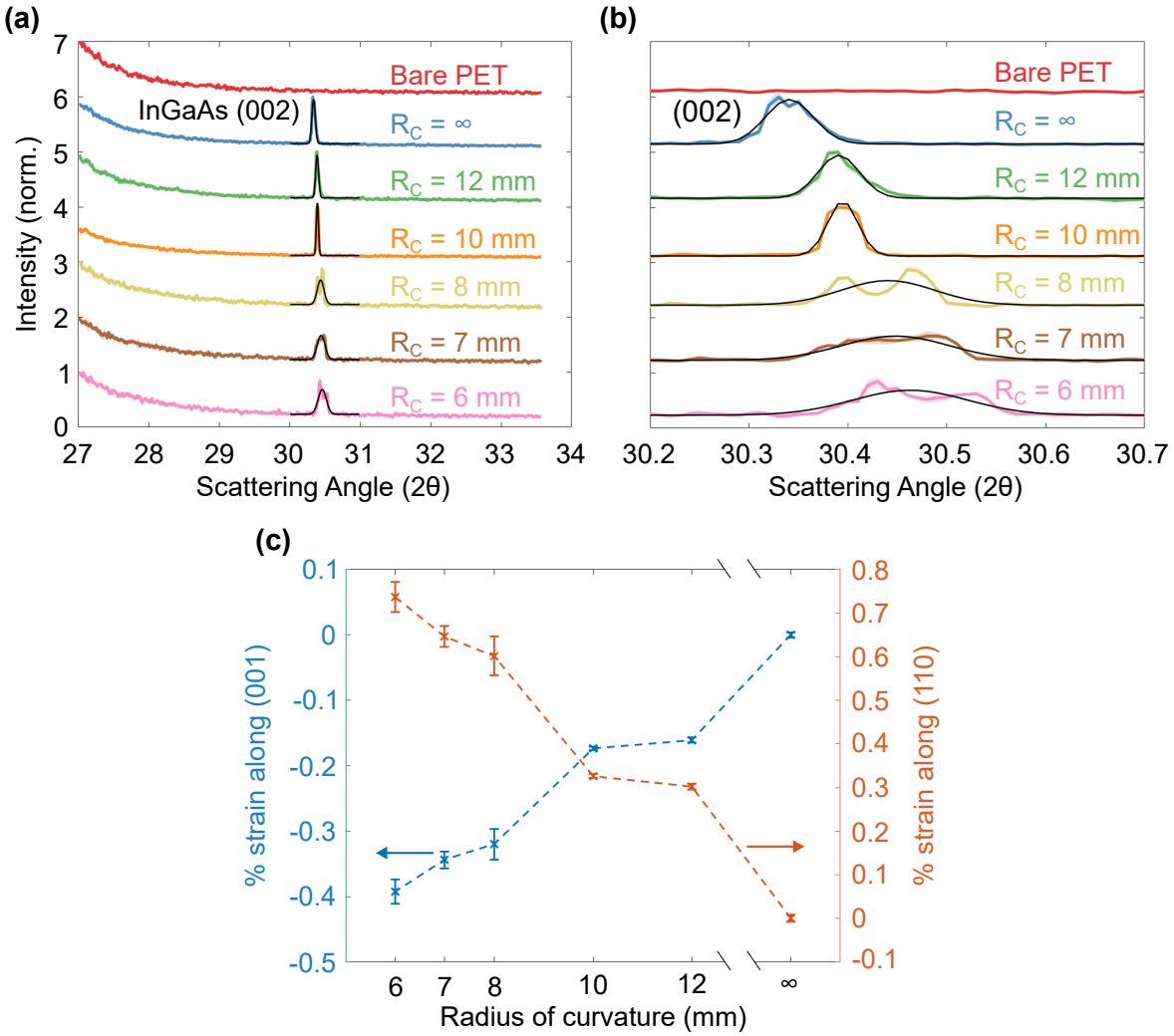

Figure 5.9: (a) θ–2θ XRD spectra of bare PET (in the $R_C = \infty$ holder) and of the 400-nm-thick InGaAs on PET sample when bent to different radii of curvature. All strain was tensile. (b) Zoom of the angles near the InGaAs (002) diffraction peak. Black lines show Gaussian fits to the data and shaded regions are the standard deviation of multiple scans. (c) Out-of-plane strain (in (001) direction) (left axis) at each bending radius calculated from the change in lattice spacing determined by XRD. These values were converted to strain along the (110) direction using Equation 5.8 and plotted on the right axis. Error bars were calculated using the error in the Gaussian fits.

microcracking is a well-known strain relaxation mechanism in thin films on flexible substrates where, once the fracture toughness is exceeded, the film fragments into discrete regions. This cracking allows material near the crack edges to relax towards its equilibrium lattice constant [223, 224].

This fragmentation can explain the observed broadening of the (002) XRD peak at

smaller radii of curvature. Within the cracked regions, a range of strain values exist, from a maximum at the centre to a minimum at the crack edges where the strain is relaxed. Consequently, there is a range of lattice constants across the microcrack that result in a broadened XRD peak. Furthermore, as will be discussed in Section 5.5.3, these microcracks also act as scattering centres that reduce the electron mobility of the InGaAs. Beyond cracking, the difference in experimental and theoretical strain may be influenced by the sample not perfectly following the bend of the sample holder due to bridging (the sample lifting slightly off the curved surface of the sample holder). Regardless of the observed relaxation effects, the XRD data confirms that increasing the sample curvature leads to a modest, reproducible strain in the InGaAs layer, the effect of which can be tested in the subsequent THz analysis.

5.5.3 THz Spectroscopy

OPTP spectroscopy was employed to study the photoconductivity of the InGaAs on PET samples under strain. Figure 5.10 (a) shows some example spectra for the 620-nm-thick InGaAs sample under different degrees of compressive strain. The spectra are similar for all bending radii, although there is a slight shift to higher frequencies in the crossing point between the imaginary and real conductivity components, which indicates a small decrease in mobility with increasing strain. Additionally, the amplitude of the photoconductivity decreases with strain, further suggesting a decrease in mobility. Note that the raw photoconductivity spectra featured oscillations originating from Fabry-Pérot interference within the thin PET substrate that could not be time-windowed out. The presented spectra have most of the oscillations removed, though there are still residual features. See Appendix A.8 for details of the raw spectra and the correction procedure.

Drude model fits closely matched the photoconductivity spectra and allowed for extraction of the electron mobility at each level of strain. Tables 5.5 and 5.6 summarise

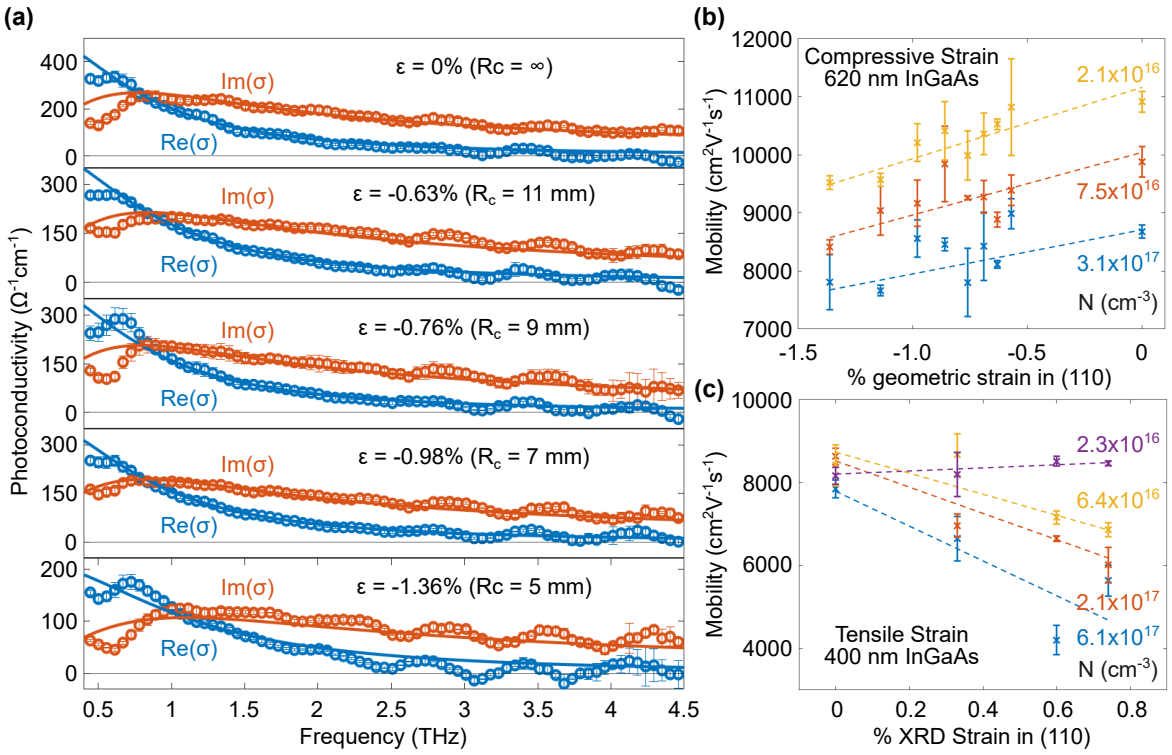

Figure 5.10: (a) THz photoconductivity spectra at different bending radii for compressively strained 620-nm-thick InGaAs on PET films. All spectra were measured 8 ps after a 16 μJcm^{-2} photoexcitation (average initial photoexcited carrier density $N \sim 5.6 \times 10^{17}$ cm^{-3}). The strain (negative for compression, taken from Table 5.4) and bending radii are recorded next to each spectrum. Solid lines show Drude model fits to the experimental data. Frequencies below 0.4 THz were impacted by aperture artefacts and are thus excluded from the figure. The raw spectra featured Fabry-Pérot oscillations that have been subtracted in these spectra. (b,c) Electron mobilities extracted from Drude fits to THz photoconductivity spectra for compressively strained 620-nm-thick InGaAs on PET (b) and tensile strained 400-nm-thick InGaAs on PET (c). Dotted lines show linear fits to the data. Different colours indicate data measured at different excitation fluences with the initial average photoexcited carrier densities are shown next to each set of data.

the mobility results for compressive strain and tensile strain respectively. Panels (b) and (c) plot the extracted mobilities of 620-nm-thick InGaAs under compressive strain and 400-nm-thick InGaAs under tensile strain respectively. The mobility generally decreases as the strain increases for both compressive and tensile strain. There is significant noise within the mobilities that arises from fluctuations in the optical pump from instabilities in the TOPAS, which can lead to a spread in the mobility values – which likely caused the mobility to slightly increase with increasing strain when the 400-nm thick InGaAs had a

photoinjected carrier density of $N = 2.3 \times 10^{16}\,\mathrm{cm}^{-3}$ (purple line in panel (c)). Despite this limitation, linear fits to the data indicate an average decrease of $\sim 1200\,\mathrm{cm}^2\mathrm{V}^{-1}\mathrm{s}^{-1}$ per % of compressive strain and $\sim 2000\,\mathrm{cm}^2\mathrm{V}^{-1}\mathrm{s}^{-1}$ per % of tensile strain. Note that the compressive strain here is the geometric strain of the inner surface of the 620-nm-thick InGaAs from Table 5.4, whereas the tensile strain is the strain in the (110) direction calculated from XRD. Assuming the true compressive strain is approximately half the geometrically calculated strain, as it was for the tensile strain, then the change in mobility with strain is almost identical for both compressive and tensile bending.

As observed in the InGaAs:Fe samples, mobilities are reduced at higher charge-carrier densities. Similarly, this trend is attributed to band non-parabolicity and carrier-carrier scattering. The 400-nm-thick InGaAs had lower mobilities than the 620-nm-thick film, likely owing to the formation of microcracks in the 400-nm-thick film that act as scattering centres to reduce charge-carrier mobility. Note that the microcracks require tensile strain to form, which is why the 620-nm-thick film under compressive strain did not exhibit these cracks, however it was still susceptible to other strain relaxation mechanisms, such as delamination and buckling [225]. Finally, it is important to note that these THz measurements were conducted in the following order for compressive strain: $R_C = \infty$, 6 mm, 12 mm, 7 mm, 11 mm, 8 mm, 10 mm, 9 mm, and lastly 5 mm; and for tensile strain: $R_C = \infty$, 6 mm, 10 mm, 8 mm. This approach of alternating between low and high bending radii was to prevent any trends from resulting solely from damage to the films from excessive stress. Note that the 620-nm-thick InGaAs was visibly delaminating from the PET at $R_C = 5$ mm, hence the switch to the 400-nm-thick sample for the tensile strain measurements.

Figure 5.11 shows how the photoconductivity of the InGaAs on PET samples decayed after photoexcitation for the 620-nm-thick InGaAs on PET under compressive strain (a) and the 400-nm-thick InGaAs on PET under tensile strain (b). While the data is noisy

R_C (mm)	$\varepsilon_{\text{theory}}$ (%)	μ ($\text{cm}^2\text{V}^{-1}\text{s}^{-1}$)					
		2.1×10^{16} ($0.6\,\mu\text{J}\,\text{cm}^{-2}$)	3.8×10^{16} ($1\,\mu\text{J}\,\text{cm}^{-2}$)	7.5×10^{16} ($2\,\mu\text{J}\,\text{cm}^{-2}$)	1.5×10^{17} ($4\,\mu\text{J}\,\text{cm}^{-2}$)	3.1×10^{17} ($9\,\mu\text{J}\,\text{cm}^{-2}$)	5.6×10^{17} ($16\,\mu\text{J}\,\text{cm}^{-2}$)
∞	0.00	10900 ± 100	9700 ± 200	9900 ± 300	9200 ± 200	8700 ± 100	8800 ± 200
12	-0.57	10800 ± 800	9900 ± 200	9400 ± 300	9200 ± 400	9000 ± 300	8600 ± 200
11	-0.63	10500 ± 100	9600 ± 500	8900 ± 100	8400 ± 300	8100 ± 100	8100 ± 200
10	-0.69	10400 ± 400	10400 ± 200	9300 ± 300	10700 ± 700	8400 ± 600	8200 ± 200
9	-0.76	10000 ± 400	10100 ± 300	9300 ± 100	8100 ± 300	7800 ± 600	8600 ± 400
8	-0.86	10400 ± 500	9800 ± 200	9800 ± 700	8700 ± 100	8500 ± 100	8300 ± 100
7	-0.98	10200 ± 300	9200 ± 200	9200 ± 400	8500 ± 100	8600 ± 300	8300 ± 300
6	-1.14	9600 ± 100	9500 ± 300	9000 ± 400	8400 ± 400	7700 ± 100	8000 ± 100
5	-1.36	9500 ± 100	8500 ± 100	8400 ± 100	7500 ± 100	7800 ± 100	6200 ± 300

Table 5.5: Mobility μ from Drude fits to the THz photoconductivity spectra of 620-nm-thick InGaAs on PET under compressive strain. Nominal strain $\varepsilon_{\text{theory}}$ is computed from holder radius. Average initial photogenerated carrier densities N are quoted for each photoexcitation fluence (parentheses).

R_C (mm)	ε_{XRD} (%)	μ ($cm^2V^{-1}s^{-1}$)			
		2.3×10^{16} ($0.6\,\mu J\,cm^{-2}$)	6.4×10^{16} ($2\,\mu J\,cm^{-2}$)	2.1×10^{17} ($6\,\mu J\,cm^{-2}$)	6.1×10^{17} ($16\,\mu J\,cm^{-2}$)
∞	0.00	8200 ± 200	8400 ± 500	8600 ± 200	7800 ± 200
10	0.33	8200 ± 500	8700 ± 500	7000 ± 300	6600 ± 500
8	0.60	8500 ± 100	7200 ± 200	6700 ± 100	4200 ± 300
6	0.74	8500 ± 100	6900 ± 200	6000 ± 400	5600 ± 400

Table 5.6: Mobility μ from Drude fits to the THz photoconductivity spectra of 400-nm-thick InGaAs on PET under tensile strain. Strain ε_{XRD} is the strain along the (110) direction extracted from XRD measurements.

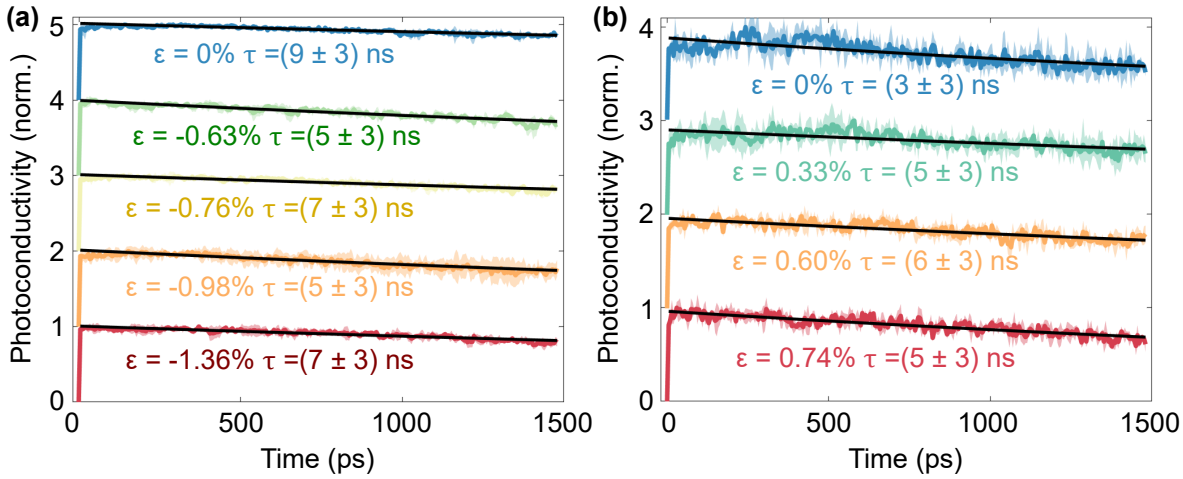

Figure 5.11: THz photoconductivity as a function of time after a $16\,\mu Jcm^{-2}$ photoexcitation for different levels of compressive strain in 620-nm-thick InGaAs on PET (a) and tensile strain in 400-nm-thick InGaAs on PET (b). Solid lines show fits to a monoexponential decay and the fitted lifetimes are shown next to the data.

due to the instabilities in the TOPAS, it is clear that the charge-carriers have lifetimes that cannot be precisely resolved on the time-scale of this THz spectrometer. Estimates of the electron lifetimes from monoexponential fits suggest lifetimes of several nanoseconds, with no obvious change as a function of strain. Measurements were conducted across a range of excitation fluences with no measurable change in lifetime. Measurement with a system that can resolve a greater time window is necessary to identify a trend in electron lifetime with strain in these samples. Regardless, the data here shows that strain alone cannot reduce the lifetimes to the picosecond range that Fe-doping achieved.

5.6 Conclusions

This chapter has explored two different approaches for controlling the properties of $In_{0.53}Ga_{0.47}As$: doping with Fe during MBE growth, and applying external uniaxial strain. Fe doping was shown to be highly effective at controlling the electron lifetime of InGaAs by introducing deep trap states. Lifetimes of hundreds of picoseconds to ∼600 fs could be achieved by adjusting the Fe dopant concentration from nominally undoped to $4.6\times10^{20}\,cm^{-3}$. The electron mobility also dropped as the Fe concentration increased, but mobilities over $2000\,cm^2V^{-1}s^{-1}$ were paired with sub-ps lifetimes for InGaAs:Fe with an Fe concentration of $1.5\times10^{20}\,cm^{-3}$. Such a material is highly promising for high speed optoelectronics operating at 1550 nm. The results presented here form a map of the electron mobilities and lifetimes of InGaAs:Fe as a function of both Fe doping density and charge-carrier density, providing a clear description of the optimal properties for a range of device operating conditions.

The study on uniaxial strain revealed no changes in the electron lifetime of InGaAs, but did show a modest decrease in mobility with increasing strain – approximately 1000–$2000\,cm^2V^{-1}s^{-1}$ per % strain for both tensile and compressive bending along the (110) axis of InGaAs. These results demonstrate that strain is not an effective tool for controlling the optoelectronic properties of InGaAs, but show that InGaAs can maintain its high electron mobilities even under significant bending, indicating its potential in flexible electronics. Development of the sample holders to strain the samples and the experimental methods for conducting XRD and THz spectroscopy are useful tools that can be employed in future strain studies on other materials that have a stronger response to strain than InGaAs. Identifying such materials with band structure calculations will be an important step before undertaking the experimental work. Overall, this chapter has demonstrated the effectiveness of THz spectroscopy for the study and optimisation of III–V semiconductors.

6

Conclusion

Terahertz (THz) spectroscopy has matured into a powerful tool for probing charge transport and ultrafast dynamics in semiconductors. This thesis has advanced both the experimental toolkit and the analysis, and utilised the refined methods to characterise and optimise the optoelectronic properties of nanostructures and thin films.

Chapter 3 highlighted the problems of residual light transmitting through spintronic THz emitters (STEs) and subsequently photoexciting samples or damaging detection elements. An improved STE design incorporating high-reflectivity (HR) and anti-reflective (AR) coatings addressed this problem. The HR coating suppressed transmission of the target wavelength (800 nm) to less than 0.1 % while increasing the absorption of the optical pulse within the STE layers. The AR coating on the front surface further increased the absorption of the optical pulse by the STE. As a result, the AR+HR-coated STE generated THz radiation with a roughly 40 % increase in electric field strength compared to an uncoated STE. These enhanced emitters enable THz spectroscopy with greater signal levels and sensitivity while eliminating undesirable photoexcitation to the sample. Measurements of a GaAs wafer demonstrated the effectiveness of the coated STEs for accurately extracting the equilibrium transport parameters.

Chapter 4 investigated how geometry impacts the THz conductivity spectra of micro and nanostructured semiconductors. GaAs nanowires of different lengths exhibited resonances in their photoconductivity spectra, with the resonant frequency increasing as the length of the nanowire decreased. This effect was made clear in measurements of well-defined GaAs microsquare arrays, confirming the inverse relationship between resonance frequency and feature size. The resonant frequency scaled with the square root of the charge-carrier density, consistent with a plasmonic origin, corroborated by finite-difference time-domain simulations. The plasmon resonances were separated from the intrinsic response of the materials using the surface plasmon model [81] – verifying the model as a means to accurately extract the charge-carrier mobility from micro/nanostructures with vastly different geometries. An important consequence of the relationship between geometry and plasmon resonance is that ensembles of nanostructures with different feature sizes (such as nanowire ensembles with a distribution of lengths) will broaden the geometric resonance and reduce the extracted THz mobility. Hence, mobilities measured by THz spectroscopy in ensembles with significant size distributions should be considered a lower bound for the true mobility of the samples.

Chapter 5 explored how the optoelectronic properties of InGaAs are impacted by two different methods: Fe doping during crystal growth; and applying mechanical strain to $In_{0.53}Ga_{0.47}As$ (InGaAs) thin-films. Optical-pump THz-probe spectroscopy revealed that Fe-doping can reduce the electron lifetime from hundreds of picoseconds in nominally undoped InGaAs to several hundred femtoseconds in highly Fe-doped InGaAs. Moreover, the electron mobilities of the highly-doped InGaAs remained high ($> 2000\,cm^2V^{-1}s^{-1}$) at Fe doping densities as high as $1.5\times10^{20}\,cm^{-3}$, priming InGaAs:Fe for operation in high-speed optoelectronics. The results in this thesis map out the electron mobilities and lifetimes of InGaAs:Fe as a function of Fe concentration and photoinjected charge-carrier density, such that the ideal material composition can be selected for a given application.

In contrast, uniaxial bending of thin-film InGaAs on PET resulted in no observable decrease in electron lifetime and a modest decrease in mobility ($\sim$1000–2000 $\mathrm{cm^2V^{-1}s^{-1}}$ per % strain), indicating that InGaAs maintains its excellent charge transport under strain (suitable for flexible electronics) while demonstrating that strain is not a strong tuning tool for electron lifetimes in InGaAs. The tools and methodology developed for study of InGaAs under strain are all applicable to future THz studies of materials with greater potential for strain engineering.

Overall, these results illustrate how careful understanding of THz spectroscopy allows for the reliable extraction of material properties without the need for intrusive contacts, and how these properties can inform the design and optimisation of III–V semiconductors for device applications. The coated STEs increase the available THz signal while eliminating a source of uncontrolled photoexcitation; the surface-plasmon model enables analysis of semiconductors at the nanoscale and presents a path to understanding and exploiting geometric resonances; and the InGaAs studies demonstrate the effectiveness of THz spectroscopy for understanding tuning mechanisms and optimising III–V semiconductor properties.

6.1 Outlook

There are many routes to build on the research in this thesis. One route is to consider alternative materials to Ta_2O_5 in the design of the HR coating on the optimised STEs to reduce absorption of the high-frequency THz components while blocking transmission of the THz-generation beam. Additionally, the substrate material could be swapped with Si to further improve the thermal conductivity of the STE. Importantly, Si absorbs 800 nm light strongly, so the design would need to be reversed such that the THz-generation beam enters the STE layers before the substrate, rather than entering the substrate first as it currently does. The reversed design concept should promote propagation of the

THz emission into the forward direction [51]. Extra design concepts could introduce variable magnetic fields around the STE to increase tunability of the polarisation state of the emitted THz pulse.

The establishment of a relationship between subwavelength geometry and THz resonances is an important step in potentially exploiting the resonances. A natural next step is to characterise the geometric factor, g (Section 4.4.3), such that the resonant frequency of a given structure can be quickly identified. Simulations paired with an experimental study of micro-rectangle arrays to investigate the effect of aspect ratio would be a good starting point. Additionally, a study of carefully grown III–V semiconductor nanowire arrays with uniform lengths and directionality would be an interesting verification of the results in this thesis.

One could continue the research on Fe-doped $In_{0.53}Ga_{0.47}As$ by comparing the properties of ion-implanted Fe dopants to dopants incorporated during growth to see if there are alternative methods to achieve the optimal material properties. The strain study also has plenty of potential for future research. For example, band structure simulations can be used to identify good candidate materials and the methodology developed in this thesis applied to these materials. Additional measurements to identify shifts in the band gap, such as photoluminescence spectroscopy, would help further scrutinise the effects of strain. Furthermore, a comparison between externally applied strain and an equivalent amount of lattice-mismatch strain could illuminate fundamental differences in these two approaches.

Overall, THz spectroscopy is a powerful tool that presents many exciting opportunities for impactful research and is well-positioned to continue to drive improvements in our understanding of III–V semiconductors.

Appendices

A

Appendix

A.1 Detailed Microsquare Fabrication

The GaAs microsquare arrays were fabricated at the Australian National University by Dr. Tuomas Haggren. The process began with epitaxial growth using MOCVD on epi-ready (100) GaAs wafers. Prior to growth, the wafer was annealed at 720 °C for 10 minutes under arsine (AsH_2) overpressure to desorb contaminants and surface oxides. The reactor temperature was then lowered to 650 °C for the growth of a GaAs buffer layer, InGaP etch stop layer, and a GaAs layer to be transferred for fabrication. Trimethylgallium, trimethylindium, and PH_3 were used for the InGaP growth with nominal vapour phase flows of 2.1×10^{-5}, 2.2×10^{-5}, and 8.3×10^{-3} mol/min respectively, yielding a V/III ratio of 196 and a lattice-matched solid phase composition. After the growth of the 300-nm-thick InGaP etch stop layer, a 600-nm-thick GaAs layer was grown at 650 °C using 1.1×10^{-4} mol/min of trimethylgallium and 4.5×10^{-3} mol/min of AsH_3, yielding a V/III ratio of 40.

To create the microsquare pattern, electron beam lithography was used to pattern ZEP resist that was used as an etch mask for inductively coupled reactive ion etching (ICP-RIE) of the GaAs layer. The GaAs etching was done using $SiCl_4$ (1.5 sccm) and Ar (10 sccm) at 0.3 Pa with a bias of 40 W and ICP power of 200 W. After etching, the remaining ZEP

resist was removed with a remover and ultrasonication, followed by O_2 plasma etching. The patterned wafer was then covered with SU8-2 (by spin coating at 5000 rpm for 60 s, baking at 85 °C for 15 minutes, and at 250 °C for 7 minutes on a hot plate). Next, PMMA A8 was spin-coated on the GaAs wafer as well as a reference c-sapphire substrate. PMMA-coated GaAs films (∼1 cm^2 in size) and sapphire wafers were hot embossed together at 180 °C for 10 minutes with a piston force of 500 N. Finally, the GaAs wafer was etched selectively in H_3PO_4:H_2O_2 1:3 solution for ∼2 hours, and subsequently the InGaP etch stop layer was etched with concentrated HCl for 60 s, completing the fabrication.

In total four samples of 600-nm-thick GaAs on c-sapphire substrates were produced – one with a 5×5 mm active area of 7×7 μm^2 squares, one with a 5×5 mm active area of 50×50 μm^2 squares, and another with a 5×5 mm active area of 500×500 μm^2. The final GaAs film had no patterning and was used as a reference.

A.2 InGaAs:Fe Reflection Artefact

Section 5.4 extracts the electron lifetimes of $In_{0.53}Ga_{0.47}As$ doped with Fe by fitting a monoexponential decay to OPTP spectroscopy data. The fitting procedure was limited to times less than 7.5 ps after photoexcitation because of a secondary rise in the photoconductivity near 8 ps. Figure A.1 (a) illustrates this secondary rise in the [Fe] = 1.5×10^{20} cm^{-3} sample.

The refractive index of InP at 1550 nm is approximately $n_{InP} = 3.2$ [226]. Hence the travel time of light through the InP substrate is

$$t_{InP} = \frac{d}{v} = \frac{350\mu m}{c/n_{InP}} \approx 3.74\,\text{ps}. \tag{A.1}$$

Therefore, the time for the reflected pulse to reach the InGaAs layers is roughly 7.5 ps – very close to the observed timing of the secondary rise. The slight difference could arise from a ∼5% increase in InP thickness compared to the nominal value. Thus, the secondary

rise in the InGaAs:Fe is attributed to back-reflection of the 1550 nm excitation beam from the rear surface of the InP substrate, which subsequently re-excites the InGaAs:Fe layer, as depicted in Figure A.1 (b). The rise is not as sharp as the initial excitation, likely due to dispersion of the 1550 nm light within the InGaAs/InAlAs/InP stack.

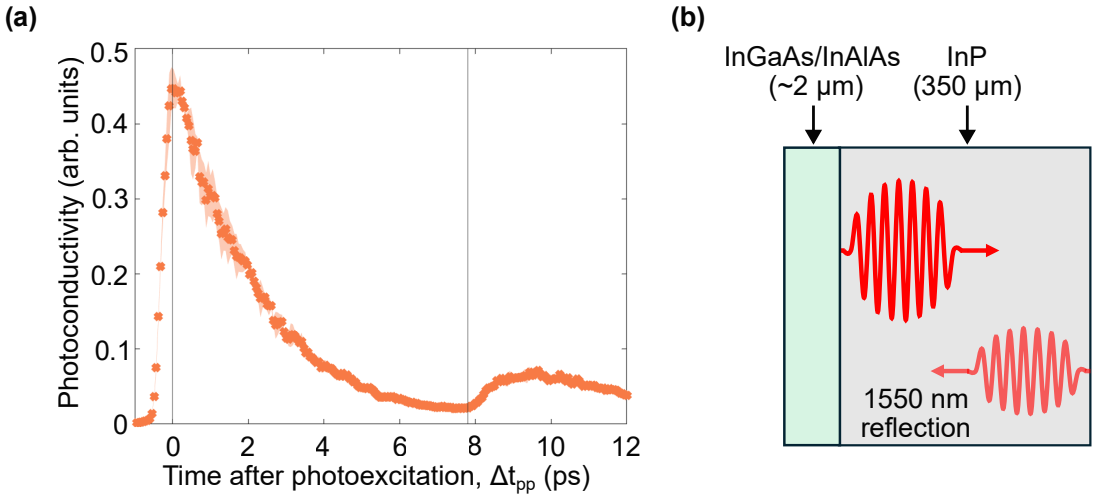

Figure A.1: (a) Photoconductivity decay of InGaAs:Fe ([Fe] = $1.5\times10^{20}\,\mathrm{cm}^{-3}$) after photoexcitation with a 1550 nm laser beam (spot size 2.8 mm FWHM) with fluence $33\,\mu\mathrm{Jcm}^{-2}$ (initial $N = 9.1\times10^{19}\,\mathrm{cm}^{-3}$). A secondary rise was observed approximately 8 ps after photoexcitation. (b) Schematic diagram of the InGaAs:Fe sample on its InP substrate. A fraction of the 1550 nm excitation transmits through the InGaAs, travels through the InP substrate, and is then reflected back towards the InGaAs layer.

A.3 Comparison of Excitation Spot Sizes

Two excitation spot sizes were used in the analysis of the InGaAs:Fe samples: a 2.8 mm and a 5.3 mm FWHM beam. The 5.3 mm beam was significantly larger than the THz beam size of 1.3 mm FWHM, which ensured the THz radiation probed a highly uniform charge-carrier density, thus reducing any deviations from the Drude model that may arise from probing a variable carrier density [19]. Thus, the THz photoconductivity spectra were measured only with the larger spot size and the reduced fluence range that it could achieve.

The spot size was less important for measurements of the photoconductivity decay. Hence, the smaller excitation beam could be used to reach higher fluences and probe the

effect of greater charge-carrier densities on the electron lifetime of the samples. To verify that the change in beam size had limited effect on the measurements, photoconductivity decay curves were measured at similar fluences using both beam sizes.

Figure A.2 shows the photoconductivity as a function of time after photoexcitation for the [Fe] $= 1.6 \times 10^{19}\,\mathrm{cm}^{-3}$ InGaAs:Fe sample. Panels (a) and (b) were measured with the large spot size, while panels (c) and (d) used the small spot size. The electron lifetimes for each measurement are recorded on the figure. The large beam excitations resulted in slightly lower electron lifetimes than with the small excitation beam. However, the fluences with the large beam were also slightly lower (13 and $6\,\mu\mathrm{Jcm}^{-2}$) compared to the small beam excitations (14 and $7\,\mu\mathrm{Jcm}^{-2}$). As demonstrated in Section 5.4, the electron lifetime of the InGaAs:Fe samples increases with increasing charge-carrier density (excitation fluence), hence part of the difference in electron lifetime for the beam sizes can be explained by this slight fluence difference. Taking this effect into account, the change in excitation beam size is expected to have only a minor impact on the photoconductivity decay results and thus results with both beam sizes are used in throughout Section 5.4.

A.4 Calculation of Photoinjected Charge-Carrier Density

The excitation fluences were calculated from the experimentally measured beam widths and incident power at the sample position. The fluences were then converted to a photoinjected charge-carrier density by considering the number of 1550 nm photons absorbed by the InGaAs. The calculation procedure is as follows:

Photons per excitation laser pulse: the total number of photons incident on the sample per laser pulse is given by

$$N_{\mathrm{total}} = \frac{E_{\mathrm{pulse}}}{E_{\mathrm{photon}}}, \tag{A.2}$$

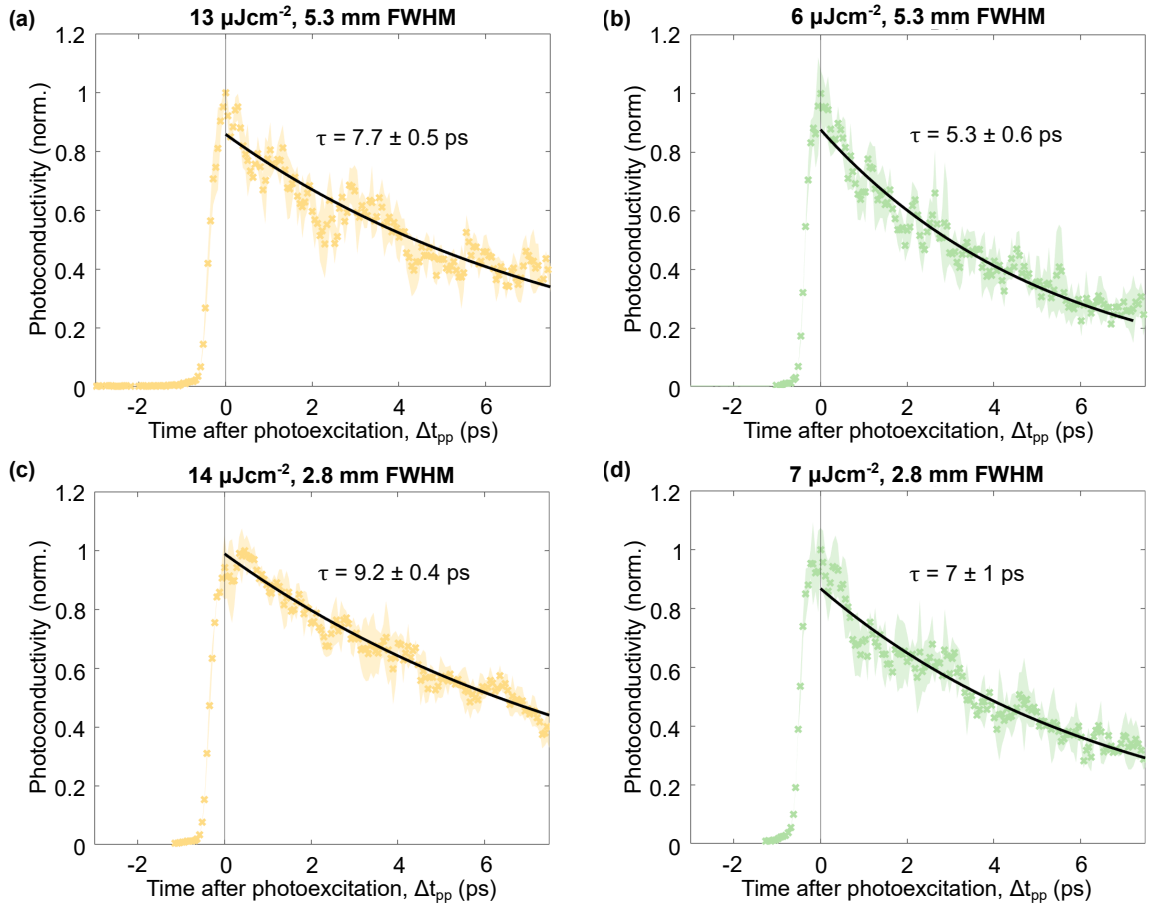

Figure A.2: Photoconductivity decay measurements for InGaAs:Fe at [Fe] $= 1.6 \times 10^{19}\,\mathrm{cm}^{-3}$. The top row (a,b) shows data obtained using the 5.3 mm FWHM excitation beam, while the bottom row (c,d) was measured using the 2.8 mm FWHM excitation beam. The excitation fluences were (a) $13\,\mu\mathrm{Jcm}^{-2}$, (b) $6\,\mu\mathrm{Jcm}^{-2}$, (c) $14\,\mu\mathrm{Jcm}^{-2}$, and (d) $7\,\mu\mathrm{Jcm}^{-2}$. Black lines show monoexponential fits to the data and the corresponding electron lifetimes are displayed on each panel.

where E_{pulse} is the total energy per laser pulse and $E_{\mathrm{photon}} \approx 0.8\,\mathrm{eV}$ is the energy of each 1550 nm photon.

Reflection loss at vacuum|InGaAs interface: a significant fraction of the incident photons are reflected at the vacuum|InGaAs interface. The reflectance for normal incidence light is given by

$$R = \left|\frac{n-1}{n+1}\right|^2, \tag{A.3}$$

where $n = 3.56$ is the refractive index of InGaAs at 1550 nm [173]. Note that this

calculation assumes the InAlAs buffer layer has negligible effect on the reflection as it was only 20 nm thick. Thus, the number of photons entering the InGaAs layer per laser pulse is

$$N_0 = (1 - R)N_{\text{total}}. \tag{A.4}$$

Absorption within InGaAs layer: the spatial distribution of absorbed photons within the InGaAs layer is determined by the Beer-Lambert law. Assuming that each absorbed photon generates one free charge-carrier, the number of carriers generated per unit volume at depth z into the InGaAs is

$$N(z) = \frac{N_0 \alpha \exp(-\alpha z)}{A_{\text{eff}}}, \tag{A.5}$$

where $\alpha = 8100\,\text{cm}^{-1}$ is the absorption coefficient of InGaAs at 1550 nm [173], and A_{eff} is the effective areal overlap of the THz and photoexcitation beams as defined in section 2.3.2. Figure A.3 shows an example of the excited charge-carrier profile in the InGaAs:Fe samples after a $60\,\mu\text{Jcm}^{-2}$ photoexcitation. Note that $N(z)$ is the profile immediately after photoexcitation with no recombination or diffusion effects factored in.

The THz wavelength is large compared to the thickness of the InGaAs layer, hence the THz effectively probes the average charge-carrier density within the InGaAs. This average is calculated from the total absorbed charge-carrier density throughout the full thickness divided by the volume of the excitation area. Whenever charge-carrier density is referred to in Chapter 5, it is, unless otherwise stated, this average initial value derived from the excitation fluence.

Charge-carrier density 1 ps after photoexcitation: the THz photoconductivity spectra for the InGaAs:Fe samples were measured 1 ps after photoexcitation. As the electrons lifetimes of these samples was very fast, it is important to consider the effective charge-carrier density that was probed at 1 ps. Using the electron lifetimes, τ_e in Table 5.2, the average carrier-density at 1 ps is

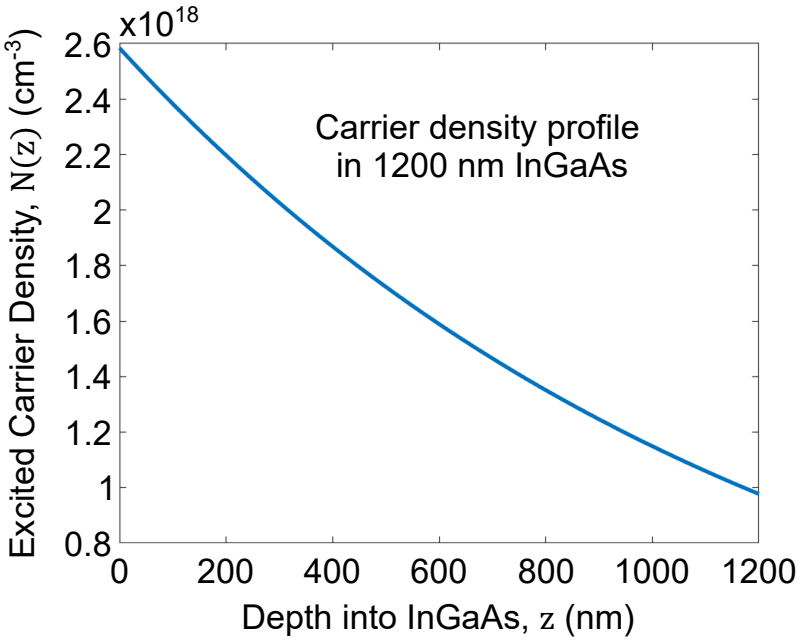

Figure A.3: Photoexcited charge-carrier density profile through a 1200-nm-thick InGaAs layer after a 60 μJcm^{-2} photoexcitation. The profile is calculated immediately after photoexcitation and does not factor in diffusion.

$$N(t = 1\,\text{ps}) = N_{\text{peak}} \exp(-t/\tau_e). \tag{A.6}$$

Table A.1 lists the carrier densities 1 ps after excitation for the fluences used during measurement of the THz photoconductivity spectra of the InGaAs:Fe samples. Note the densities corresponding to the 6, 11, and 19 μJcm^{-2} fluence excitations were approximated using the electron lifetime measured at the closest fluence to those values.

A.5 Detailed Fabrication of Strained InGaAs on PET samples

The $In_{0.53}Ga_{0.47}As$ on PET samples studied in the strain sections of Chapter 5 were fabricated by Dr. Tuomas Haggren at the Australian National University. The detailed fabrication process is as follows:

The $In_{0.53}Ga_{0.47}As$ thin-films were grown by MOCVD. First, $In_{0.53}Ga_{0.47}As$/InP/$In_{0.53}Ga_{0.47}As$

[Fe] (cm^{-3})	**Carrier density 1 ps after photoexcitation (cm^{-3})**					
	0.7 $\mu J\,cm^{-2}$	1.3 $\mu J\,cm^{-2}$	3 $\mu J\,cm^{-2}$	5 $\mu J\,cm^{-2}$	11 $\mu J\,cm^{-2}$	19 $\mu J\,cm^{-2}$
2.7×10^{17}	1.7×10^{16}	3.5×10^{16}	8.9×10^{16}	1.5×10^{17}	3.0×10^{17}	5.2×10^{17}
1.1×10^{18}	1.6×10^{16}	3.3×10^{16}	8.5×10^{16}	1.4×10^{17}	3.0×10^{17}	5.2×10^{17}
3.4×10^{18}	1.5×10^{16}	3.1×10^{16}	8.4×10^{16}	1.4×10^{17}	3.0×10^{17}	5.1×10^{17}
1.6×10^{19}	8.6×10^{15}	2.0×10^{16}	6.0×10^{16}	1.2×10^{17}	2.7×10^{17}	4.7×10^{17}
1.5×10^{20}	4.7×10^{15}	7.7×10^{15}	2.1×10^{16}	3.6×10^{16}	1.2×10^{17}	2.0×10^{17}
4.6×10^{20}	2.9×10^{15}	7.0×10^{15}	1.8×10^{16}	3.3×10^{16}	6.7×10^{16}	1.1×10^{17}

Table A.1: Photoexcited charge-carrier densities in the InGaAs:Fe samples 1 ps after different fluence excitations. Calculated using the electron lifetimes in Table 5.2. The carrier densities after the 5, 11, and 19 μJcm^{-2} fluence excitation were approximated using the lifetimes at 6, 13, and 13 μJcm^{-2} excitation respectively.

layers were grown on an epi-ready on-orient InP(100) substrate, where the $In_{0.53}Ga_{0.47}As$ layers were lattice matched to InP. The first $In_{0.53}Ga_{0.47}As$ layer was 180 nm thick, the InP 100 nm thick, and the final $In_{0.53}Ga_{0.47}As$ layer was either 400 or 620 nm thick. The epitaxial growth run started with a 10-minute de-oxidation step at 700 °C under PH_3 flow. The reactor temperature was then lowered to 650 °C (thermocouple reading), and the $In_{0.53}Ga_{0.47}As/InP/In_{0.53}Ga_{0.47}As$ layers were grown using trimethylgallium, trimethylindium, AsH_3, and PH_3 as precursors. The V/III ratio for the $In_{0.53}Ga_{0.47}As$ growth was 120. The reactor was then cooled down to 360 °C under AsH_3 flow.

The $InP/In_{0.53}Ga_{0.47}As$ substrate and a PET film were then coated with SU8-2 polymer via spin coating, and the $In_{0.53}Ga_{0.47}As$ on the InP substrate was placed against the PET film. The $InP/In_{0.53}Ga_{0.47}As$ wafer then permanently attached to the PET film using hot embossing (EVG 520HE) at 200 °C and a piston force of 500 N. Finally, the InP wafer was etched using concentrated HCl, which only slowly attacks $In_{0.53}Ga_{0.47}As$, and therefore the etching stopped in the first $In_{0.53}Ga_{0.47}As$ layer. Subsequently, the first $In_{0.53}Ga_{0.47}As$ layer was removed selectively using citric acid and hydrogen peroxide. Lastly, the remaining 100 nm InP layer was removed with a ∼5 s dip into concentrated HCl. the remaining $In_{0.53}Ga_{0.47}As$ film (400 or 620 nm) on PET was then rinsed in deionised water to remove acid residues and complete the fabrication.

A.6 Strain Sample Holder Schematics

Strain was induced in the InGaAs on PET samples by bending them to a certain radius of curvature. Special sample holders were developed for this task using Fusion 360 CAD software and a 3D printer to realise the designs. Figure A.4 shows several angles of such a sample holder with slots to keep the sample at a 7, 8, or 9 mm radius of curvature. The slots to bend a sample to x radius of curvature is effectively a gap between two cylinders: one with a radius of $x - 0.5$ mm and the other with a radius of $x + 0.5$ mm. This gap

allowed the sample to smoothly slot into the holder without needing to force it in, thus reducing the risk of significantly scratching the InGaAs surface. However, the gap is larger than the sample thickness, which means the true bending radius is likely slightly less than the designed value, which contributes to the reduced strain measured using XRD compared to the theoretical strain, as discussed in Section 5.5.2. Importantly, each radius of curvature slot kept the front surface of the sample at the same position relative to the front of the sample holder, thus ensuring the sample was at the same position along the optical axis during XRD and THz spectroscopy measurements.

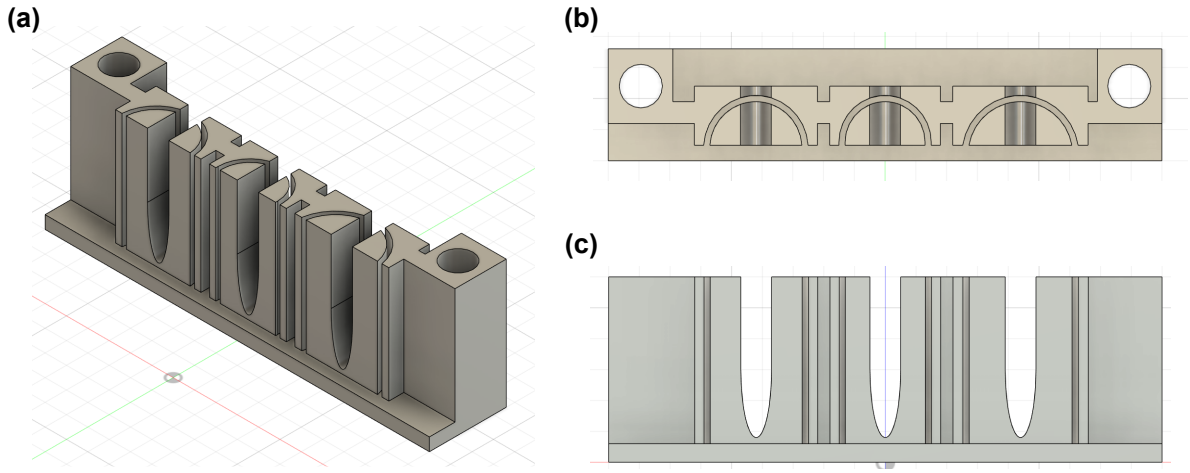

Figure A.4: Sample holder design for bending the InGaAs on PET samples. (a) Isometric view of the sample holder with 7 mm, 8 mm, and 9 mm radius of curvature slots for the sample. (b) Top-down view of the sample holder. (c) Front view of the sample holder.

A.7 Converting Strain Axes

The strained InGaAs study applied strain to the samples by bending them along the InGaAs (110) direction, hence the key strain parameter in the study is $\varepsilon_{(110)}$. However, the XRD measurements probe the inter-planar spacing in the growth direction of the crystal and thus the strain in the (001) direction, $\varepsilon_{(001)}$ is measured. Using the methods

described in Ref. [220], the strain along the (001) direction could be converted to strain along (110). The procedure is as follows:

Within the limits of Hooke's law, small material deformations are proportional to an applied stress. This relationship can be expressed using fourth-rank tensors to relate the strain, ε_{ij}, to the stress tensor, σ_{ij}, by the compliance tensor, S_{ijkl}, using the relation:

$$\varepsilon_{ij} = S_{ijkl}\sigma_{kl} \tag{A.7}$$

$In_{0.53}Ga_{0.47}As$ crystallises in a zinc-blende crystal structure [216]. The compliance tensor for crystals with this structure is given in Ref. [220] and the above equation can be expanded to (using Voigt notation)

$$\begin{pmatrix} \varepsilon_{xx} \\ \varepsilon_{yy} \\ \varepsilon_{zz} \\ 2\varepsilon_{yz} \\ 2\varepsilon_{xz} \\ 2\varepsilon_{xy} \end{pmatrix} = \begin{pmatrix} s_{11} & s_{12} & s_{12} & 0 & 0 & 0 \\ s_{12} & s_{11} & s_{12} & 0 & 0 & 0 \\ s_{12} & s_{12} & s_{11} & 0 & 0 & 0 \\ 0 & 0 & 0 & s_{44} & 0 & 0 \\ 0 & 0 & 0 & 0 & s_{44} & 0 \\ 0 & 0 & 0 & 0 & 0 & s_{44} \end{pmatrix} \begin{pmatrix} \sigma_{xx} \\ \sigma_{yy} \\ \sigma_{zz} \\ \sigma_{yz} \\ \sigma_{xz} \\ \sigma_{xy} \end{pmatrix}, \tag{A.8}$$

where x, y, z are the (100), (010), and (001) lattice directions such that ε_{xx} is the strain along the (100) direction and ε_{xy} is a shear term with components in the (100) and (010) directions. The s_{ij} terms are components of the compliance tensor and represent how much the material stretches in their relevant directions.

In section 5.5, the InGaAs is bent along the (110) crystal direction. The x, y, z basis can be transformed to one that better describes the physical scenario. Define the x', y', z' basis where x' is parallel to (110), y' is parallel to $(\bar{1}10)$, and $z' = z$ is along the (001) direction:

$$x' = \frac{1}{\sqrt{2}}(x + y), \qquad y' = \frac{1}{\sqrt{2}}(-x + y), \qquad z' = z. \tag{A.9}$$

The XRD measurements in section 5.5.2 directly measure the strain along the (001) direction – ε_{zz}. The stress is purely along the x' basis vector

$$\sigma_{x'x'} = \sigma_{\text{bend}}. \tag{A.10}$$

One can transform the new basis to the crystal basis using $\sigma_{ij} = a_{ip}a_{jq}\sigma_{p'q'}$, where

$$a = \begin{pmatrix} 1/\sqrt{2} & -1/\sqrt{2} & 0 \\ 1/\sqrt{2} & 1/\sqrt{2} & 0 \\ 0 & 0 & 1 \end{pmatrix}. \tag{A.11}$$

Thus, the stress components in the crystal basis are

$$\sigma_{xx} = \sigma_{yy} = \sigma_{xy} = \sigma_{\text{bend}}/2, \qquad \sigma_{zz} = \sigma_{yz} = \sigma_{xz} = 0. \tag{A.12}$$

These stress components can be substituted into Equation A.8 to get the (non-zero) strain components in the crystal basis

$$\varepsilon_{xx} = \varepsilon_{yy} = \frac{\sigma_{\text{bend}}}{2}(s_{11} + s_{12}), \qquad \varepsilon_{zz} = \sigma_{\text{bend}}s_{12}, \qquad \varepsilon_{xy} = \frac{\sigma_{\text{bend}}}{4}s_{44}. \tag{A.13}$$

The strain along the (110) direction follows from the definition of the new basis vectors

$$\varepsilon_{x'x'} = \frac{1}{2}(\varepsilon_{xx} + \varepsilon_{yy}) + \varepsilon_{xy} = \sigma_{\text{bend}}\left(\frac{s_{11} + s_{12}}{2} + \frac{s_{44}}{4}\right). \tag{A.14}$$

Substituting in $\sigma_{\text{bend}} = \varepsilon_{zz}/s_{12}$ relates the XRD measured strain, ε_{zz} to the strain along the bend axis, $\varepsilon_{x'x'}$

$$\varepsilon_{x'x'} = \frac{\varepsilon_{zz}}{s_{12}}\left(\frac{s_{11} + s_{12}}{2} + \frac{s_{44}}{4}\right). \tag{A.15}$$

The components of the compliance tensor are related to the stiffness constants of InGaAs by the following [220]

$$s_{11} = \frac{C_{11} + C_{12}}{(C_{11} - C_{12})(C_{11} + 2C_{12})}, \tag{A.16}$$

$$s_{12} = \frac{-C_{12}}{(C_{11} - C_{12})(C_{11} + 2C_{12})}, \tag{A.17}$$

$$s_{44} = \frac{1}{C_{44}}, \tag{A.18}$$

where $C_{11} \approx 100\,\text{GPa}$, $C_{12} \approx 49\,\text{GPa}$, and $C_{44} \approx 60\,\text{GPa}$ [216]. Substituting these values leads to the final relationship between the strain measured by XRD (ε_{zz}) and the strain along the direction of bending ($\varepsilon_{x'x'}$)

$$\varepsilon_{x'x'} \approx -1.88\,\varepsilon_{zz}. \tag{A.19}$$

A.8 Analysis of Substrate Etalon Oscillations

The THz photoconductivity spectra of the InGaAs on PET samples exhibited strong oscillations that were removed in the presented spectra of Figure 5.10. Figure A.5 (a) shows the raw photoconductivity spectra for the 620-nm-thick InGaAs on PET sample with no strain. The oscillations are present in the real and imaginary photoconductivity with a period of roughly 0.6 THz.

The refractive index of PET at THz frequencies is approximately $n_{\text{PET}} = 1.6$ [227, 228]. Hence, a single pass of the THz radiation through the PET substrate is:

$$t_{\text{PET}} = \frac{d}{v} = \frac{150\,\mu\text{m}}{c/n_{\text{PET}}} \approx 0.8\,\text{ps}. \tag{A.20}$$

The round-trip time is twice as long, corresponding to a period of $\approx 0.63\,\text{THz}$. This aligns closely with the frequency of the observed oscillations, which are attributed to Fabry-Pérot reflections within the thin PET substrate. The timing of these reflections is too short to time-window out, thus they must be accounted for during the fitting process.

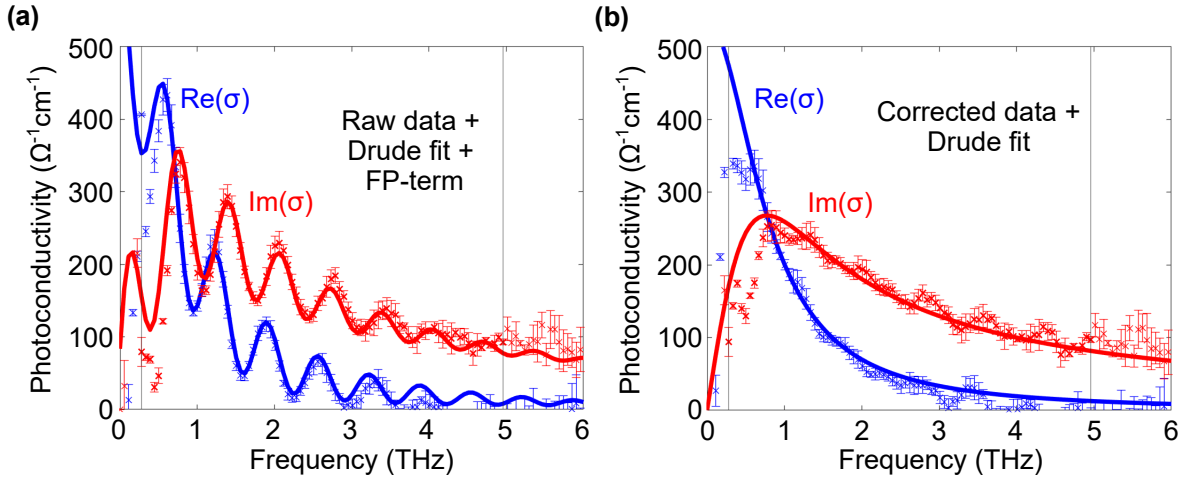

Figure A.5: Oscillations in the THz photoconductivity spectra for the 620-nm-thick InGaAs on PET sample with no applied strain. (a) Raw photoconductivity with a fit to the Drude model plus a correction factor to account for Fabry-Pérot interference. (b) Photoconductivity with the Fabry-Pérot term subtracted from the raw data. The Drude model fit is shown as a solid line.

Bending the sample could potentially alter the effective thickness of the PET that the THz beam probes, thus changing the frequency of the oscillations in the photoconductivity spectra. To investigate this, the spectra were Fourier transformed to identify the frequency of the oscillations in each measurement. To isolate the oscillations in the Fourier transform, the raw data was detrended by subtracting a cubic fit to remove the background Drude-like photoconductivity.

Figure A.6 shows the Fourier transform of the detrended spectra as a function of time delay. A clear, stationary peak is observed at 1.58 ps for all bending radii, indicating that the oscillation frequency remains constant within the resolution of the spectrometer. While the frequency was treated as a free parameter during the final Drude fitting to ensure maximum accuracy for individual scans, this analysis confirms that no systematic shift in etalon periodicity occurred due to the applied strain.

The data is thus fitted with a Drude model plus an oscillatory term to account for the Fabry-Pérot interference; this is the fit shown in Figure A.5 (a). Subtracting the correction term leaves the photoconductivity shown in Figure A.5 (b), which fits

reasonably well to the Drude model. Note that the extracted parameters from the Drude model fits have increased error compared to spectra measured for other samples in this thesis, owing to the oscillations in the raw photoconductivity.

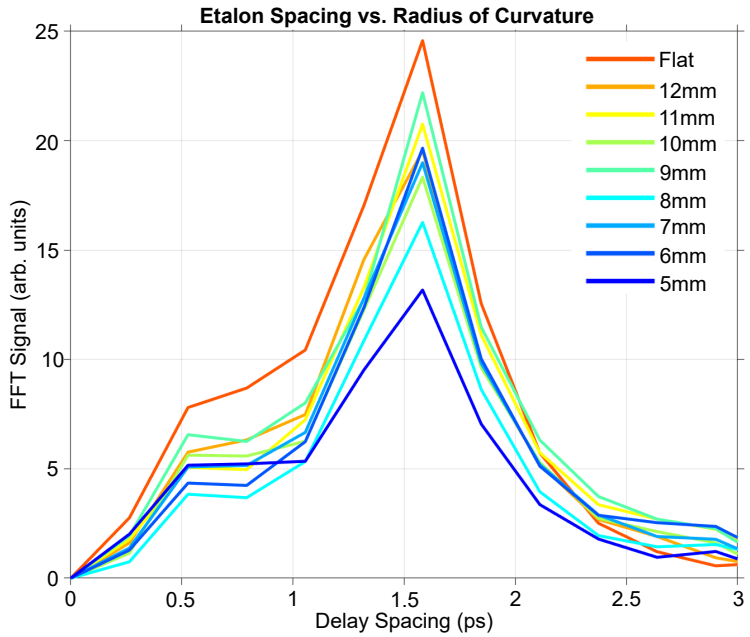

Figure A.6: Fourier transforms of the detrended photoconductivity for various bending radii. There is a clear peak for all data near 1.58 ps, which confirms that the etalon periodicity remains stable as the bending radius changes.

References

[1] Leitenstorfer, A.; Moskalenko, A. S.; Kampfrath, T.; Kono, J.; Castro-Camus, E.; Peng, K.; Qureshi, N.; Turchinovich, D.; Tanaka, K.; Markelz, A. G.; Havenith, M.; Hough, C.; Joyce, H. J.; Padilla, W. J.; Zhou, B.; Kim, K. Y.; Zhang, X. C.; Jepsen, P. U.; Dhillon, S.; Vitiello, M.; Linfield, E.; Davies, A. G.; Hoffmann, M. C.; Lewis, R.; Tonouchi, M. *et al.* 'The 2023 terahertz science and technology roadmap'. *J. Phys. D: Appl. Phys.*, 22 2023, **56**.

[2] Smith, P. R.; Auston, D. H. and Nuss, M. C. 'Subpicosecond photoconducting dipole antennas'. *IEEE J. Quantum Electron.*, 2 1988, **24**.

[3] Fattinger, C. and Grischkowsky, D. 'Terahertz beams'. *Appl. Phys. Lett.*, 6 1989, **54**, 490–492.

[4] Isgandarov, E.; Ropagnol, X.; Singh, M. and Ozaki, T. 'Intense terahertz generation from photoconductive antennas'. *Front. Optoelectron.*, 1 2021, **14**, 64–93.

[5] Burford, N. M. and El-Shenawee, M. O. 'Review of terahertz photoconductive antenna technology'. *Opt. Eng.*, 1 2017, **56**, 010901.

[6] Fülöp, J. A.; Pálfalvi, L.; Almási, G. and Hebling, J. 'Design of high-energy terahertz sources based on optical rectification'. *Opt. Express*, 2010, **18**.

[7] Seifert, T; Jaiswal, S; Martens, U; Hannegan, J; Braun, L; Maldonado, P; Freimuth, F; Kronenberg, A; Henrizi, J; Radu, I; Beaurepaire, E; Mokrousov, Y; Oppeneer, P. M.; Jourdan, M; Jakob, G; Turchinovich, D; Hayden, L. M.; Wolf, M; Münzenberg, M; Kläui, M and Kampfrath, T. 'Efficient metallic spintronic emitters of ultrabroadband terahertz radiation'. *Nat. Photonics*, 2016, **10**.

[8] Papaioannou, E. T. and Beigang, R. 'THz spintronic emitters: A review on achievements and future challenges'. *Nanophotonics*, 2 2021, **10**, 1243–1257.

[9] Wu, Q.; Hewitt, T. D. and Zhang, X. C. 'Two-dimensional electro-optic imaging of THz beams'. *Appl. Phys. Lett.*, 8 1996, **69**, 1026–1028.

[10] Casalbuoni, S.; Schlarb, H.; Schmidt, B.; Schmüser, P.; Steffen, B. and Winter, A. 'Numerical studies on the electro-optic detection of femtosecond electron bunches'. *Phys. Rev. Spec. Top. Accel. Beams*, 7 2008, **11**.

[11] Joyce, H. J.; Boland, J. L.; Davies, C. L.; Baig, S. A. and Johnston, M. B. 'A review of the electrical properties of semiconductor nanowires: Insights gained from terahertz conductivity spectroscopy'. *Semicond. Sci. Technol.*, 10 2016, **31**.

[12] Ulbricht, R.; Hendry, E.; Shan, J.; Heinz, T. F. and Bonn, M. 'Carrier dynamics in semiconductors studied with time-resolved terahertz spectroscopy'. *Rev. Mod. Phys.*, 2 2011, **83**, 543–586.

[13] Beard, M. C.; Turner, G. M. and Schmuttenmaer, C. A. 'Terahertz spectroscopy'. *J. Phys. Chem. B*, 29 2002, **106**, 7146–7159.

[14] Koch, M.; Mittleman, D. M.; Ornik, J. and Castro-Camus, E. 'Terahertz time-domain spectroscopy'. *Nat. Rev. Methods Primers*, 1 2023, **3**.

[15] Lloyd-Hughes, J. and Jeon, T. I. 'A review of the terahertz conductivity of bulk and nano-materials'. *J. Infrared Millim. Terahertz Waves*, 9 2012, **33**, 871–925.

[16] Vij, J. K.; Simpson, D. R. and Panarina, O. E. 'Far infrared spectroscopy of water at different temperatures: GHz to THz dielectric spectroscopy of water'. *J. Mol. Liq.*, 3 2004, **112**, 125–135.

[17] Jepsen, P. U.; Cooke, D. G. and Koch, M. 'Terahertz spectroscopy and imaging - Modern techniques and applications'. *Laser Photonics Rev.*, 1 2011, **5**, 124–166.

[18] Ulatowski, A. M.; Herz, L. M. and Johnston, M. B. 'Terahertz conductivity analysis for highly doped thin-film semiconductors'. *J. Infrared Millim. Terahertz Waves*, 12 2020, **41**, 1431–1449.

[19] Hempel, H.; Savenjie, T. J.; Stolterfoht, M.; Neu, J.; Failla, M.; Paingad, V. C.; Kužel, P.; Heilweil, E. J.; Spies, J. A.; Schleuning, M.; Zhao, J.; Friedrich, D.; Schwarzburg, K.; Siebbeles, L. D.; Dörflinger, P.; Dyakonov, V.; Katoh, R.; Hong, M. J.; Labram, J. G.; Monti, M.; Butler-Caddle, E.; Lloyd-Hughes, J.; Taheri, M. M.; Baxter, J. B.; Magnanelli, T. J. *et al.* 'Predicting solar cell performance from terahertz and microwave spectroscopy'. *Adv. Energy Mater.*, 13 2022, **12**.

[20] Wehrenfennig, C.; Liu, M.; Snaith, H. J.; Johnston, M. B. and Herz, L. M. 'Charge-carrier dynamics in vapour-deposited films of the organolead halide perovskite $CH_3NH_3PbI_{3-x}Cl_x$'. *Energy Environ. Sci.*, 7 2014, **7**, 2269–2275.

[21] Xia, C. Q. 'Terahertz spectroscopy of charge-carrier transport in metal-halide perovskites and narrow-gap semiconductors'. DPhil thesis. University of Oxford, 2020.

[22] Auston, D. H. 'Picosecond optoelectronic switching and gating in silicon'. *Appl. Phys. Lett.*, 3 1975, **26**, 101–103.

[23] Auston, D. H. 'Subpicosecond electro-optic shock waves'. *Appl. Phys. Lett.*, 8 1983, **43**, 713–715.

[24] Auston, D. H.; Cheung, K. P. and Smith, P. R. 'Picosecond photoconducting Hertzian dipoles'. *Appl. Phys. Lett.*, 3 1984, **45**, 284–286.

[25] Auston, D. H.; Cheung, K. P.; Valdmanis, J. A. and Kleinman, D. A. 'Cherenkov radiation from femtosecond optical pulses in electro-optic media'. *Phys. Rev. Lett.*, 1984, **53**.

[26] Lewis, R. A. 'A review of terahertz sources'. *J. Phys. D: Appl. Phys.*, 37 2014, **47**.

[27] Gallerano, G. P. and Biedron, S. 'Overview of terahertz radiation sources'. *Proceedings of the 2004 FEL Conference*. 2004, 216–221.

[28] Fattinger, C. and Grischkowsky, D. 'Point source THz optics'. *Appl. Phys. Lett.*, 16 1988, **53**.

[29] Jepsen, P. U.; Jacobsen, R. H. and Keiding, S. R. 'Generation and detection of terahertz pulses from biased semiconductor antennas'. *J. Opt. Soc. Am. B*, 11 1996, **13**, 2424.

[30] Jackson, J. D. *Classical Electrodynamics*. John Wiley & Sons, 1998.

[31] Freeman, J. R.; Beere, H. E. and Ritchie, D. A. 'Generation and Detection of Terahertz Radiation'. *THz Spectroscopy and Imaging*. Ed. by Peiponen, K.-E.; Zeitler, A. and Kuwata-Gonokami, M. Vol. 171. Springer Series in Optical Sciences. Berlin, Heidelberg: Springer, 2013, 4–6.

[32] Gupta, S.; Frankel, M. Y.; Valdmanis, J. A.; Whitaker, J. F.; Mourou, G. A.; Smith, F. W. and Calawa, A. R. 'Subpicosecond carrier lifetime in GaAs grown by molecular beam epitaxy at low temperatures'. *Appl. Phys. Lett.*, 25 1991, **59**, 3276–3278.

[33] Tani, M.; Matsuura, S.; Sakai, K. and Nakashima, S.-I. 'Emission characteristics of photoconductive antennas based on low-temperature-grown GaAs and semi-insulating GaAs'. *Appl. Opt.*, 1997, **36**.

[34] Hou, L.; Shi, W. and Chen, S. 'Noise analysis and optimization of terahertz photoconductive emitters'. *IEEE J. Sel. Top. Quantum Electron.*, 1 2013, **19**, 108–112.

[35] Chen, C.; Wu, R.; Qin, F.; Sun, Y. and Liu, W. 'Materials for 1550 nm-pumped THz photoconductive emitters'. *Semicond. Sci. Technol.*, 6 2025, **40**.

[36] Kohlhaas, R. B.; Breuer, S.; Liebermeister, L.; Nellen, S.; Deumer, M.; Schell, M.; Semtsiv, M. P.; Masselink, W. T. and Globisch, B. '637 µW emitted terahertz power from photoconductive antennas based on rhodium doped InGaAs'. *Appl. Phys. Lett.*, 13 2020, **117**.

[37] Winnerl, S; Zimmermann, B; Peter, F; Schneider, H and Helm, M. 'Terahertz Bessel-Gauss beams of radial and azimuthal polarization from microstructured photoconductive antennas'. *Opt. Express*, 2009, **7**, 77–87.

[38] Winnerl, S.; Hubrich, R.; Mittendorff, M.; Schneider, H. and Helm, M. 'Universal phase relation between longitudinal and transverse fields observed in focused terahertz beams'. *New J. Phys.*, 2012, **14**.

[39] Lu, P. K.; Jiang, X.; Zhao, Y.; Turan, D. and Jarrahi, M. 'Bias-free terahertz generation from a silicon-compatible photoconductive emitter operating at telecommunication wavelengths'. *Appl. Phys. Lett.*, 26 2022, **120**.

[40] Kampfrath, T; Battiato, M; Maldonado, P; Eilers, G; Nötzold, J; Radu, I; Freimuth, F; Mokrousov, Y; Blügel, S; Wolf, M; Oppeneer, P. M. and Münzenberg, M. 'Terahertz spin current pulses controlled by magnetic heterostructures'. *Nat. Nanotechnol.*, 2013, **8**.

[41] Wu, W.; Ameyaw, C. Y.; Doty, M. F. and Jungfleisch, M. B. 'Principles of spintronic THz emitters'. *J. Appl. Phys.*, 2021, **130**.

[42] Walowski, J. and Münzenberg, M. 'Perspective: Ultrafast magnetism and THz spintronics'. *J. Appl. Phys.*, 14 2016, **120**.

[43] Bull, C.; Hewett, S. M.; Ji, R.; Lin, C. H.; Thomson, T.; Graham, D. M. and Nutter, P. W. 'Spintronic terahertz emitters: Status and prospects from a materials perspective'. *APL Mater.*, 9 2021, **9**.

[44] Wu, Y.; Elyasi, M.; Qiu, X.; Chen, M.; Liu, Y.; Ke, L. and Yang, H. 'High-performance THz emitters based on ferromagnetic/nonmagnetic heterostructures'. *Adv. Mater.*, 4 2017, **29**.

[45] Hoffmann, A. 'Spin hall effects in metals'. *IEEE Trans. Magn.*, 10 2013, **49**, 5172–5193.

[46] Zhang, S.; Jin, Z.; Zhu, Z.; Zhu, W.; Zhang, Z.; Ma, G. and Yao, J. 'Bursts of efficient terahertz radiation with saturation effect from metal-based ferromagnetic heterostructures'. *J. Phys. D: Appl. Phys.*, 2018, **51**.

[47] Torosyan, G.; Keller, S.; Scheuer, L.; Beigang, R. and Papaioannou, E. T. 'Optimized spintronic terahertz emitters based on epitaxial grown Fe/Pt layer structures'. *Sci. Rep.*, 1 2018, **8**.

[48] Seifert, T; Jaiswal, S; Sajadi, M; Jakob, G; Winnerl, S; Wolf, M; Kläui, M and Kampfrath, T. 'Ultrabroadband single-cycle terahertz pulses with peak fields of 300 kV cm-1 from a metallic spintronic emitter'. *Appl. Phys. Lett.*, 2017, **110**.

[49] Feng, Z.; Yu, R.; Zhou, Y.; Lu, H.; Tan, W.; Deng, H.; Liu, Q.; Zhai, Z.; Zhu, L.; Cai, J.; Miao, B. and Ding, H. 'Highly efficient spintronic terahertz emitter enabled by metal–dielectric photonic crystal'. *Adv. Opt. Mater.*, 23 2018, **6**.

[50] Herapath, R. I.; Hornett, S. M.; Seifert, T. S.; Jakob, G.; Kläui, M.; Bertolotti, J.; Kampfrath, T. and Hendry, E. 'Impact of pump wavelength on terahertz emission of a cavity-enhanced spintronic trilayer'. *Appl. Phys. Lett.*, 4 2019, **114**.

[51] Rouzegar, R.; Chekhov, A. L.; Behovits, Y.; Serrano, B. R.; Syskaki, M. A.; Lambert, C. H.; Engel, D.; Martens, U.; Münzenberg, M.; Wolf, M.; Jakob, G.; Kläui, M.; Seifert, T. S. and Kampfrath, T. 'Broadband spintronic terahertz source with peak electric fields exceeding 1.5 MV/cm'. *Phys. Rev. Appl.*, 3 2023, **19**.

[52] Wagner, F. M.; Melnikas, S.; Cramer, J.; Damry, D. A.; Xia, C. Q.; Peng, K.; Jakob, G.; Kläui, M.; Kičas, S. and Johnston, M. B. 'Optimised spintronic emitters of terahertz radiation for time-domain spectroscopy'. *J. Infrared Millim. Terahertz Waves*, 1-2 2023, **44**, 52–65.

[53] Lewis, R. A. 'A review of terahertz detectors'. *J. Phys. D: Appl. Phys.*, 43 2019, **52**.

[54] Castro-Camus, E. and Alfaro, M. 'Photoconductive devices for terahertz pulsed spectroscopy: a review'. *Photonics Res.*, 3 2016, **4**, A36.

[55] Globisch, B.; Dietz, R. J.; Kohlhaas, R. B.; Göbel, T.; Schell, M.; Alcer, D.; Semtsiv, M. and Masselink, W. T. 'Iron doped InGaAs: Competitive THz emitters and detectors fabricated from the same photoconductor'. *J. Appl. Phys.*, 5 2017, **121**.

[56] Kohlhaas, R. B.; Liebermeister, L.; Breuer, S.; Amberg, M.; Felipe, D. de; Nellen, S.; Schell, M. and Globisch, B. 'Fiber coupled transceiver with 6.5 thz bandwidth for terahertz time-domain spectroscopy in reflection geometry'. *Sensors*, 9 2020, **20**.

[57] Peng, K.; Parkinson, P.; Fu, L.; Gao, Q.; Jiang, N.; Guo, Y. N.; Wang, F.; Joyce, H. J.; Boland, J. L.; Tan, H. H.; Jagadish, C. and Johnston, M. B. 'Single nanowire photoconductive terahertz detectors'. *Nano Lett.*, 1 2015, **15**, 206–210.

[58] Peng, K.; Parkinson, P.; Boland, J. L.; Gao, Q.; Wenas, Y. C.; Davies, C. L.; Li, Z.; Fu, L.; Johnston, M. B.; Tan, H. H. and Jagadish, C. 'Broadband phase-sensitive single InP nanowire photoconductive terahertz detectors'. *Nano Lett.*, 8 2016, **16**, 4925–4931.

[59] Peng, K.; Parkinson, P.; Gao, Q.; Boland, J. L.; Li, Z.; Wang, F.; Mokkapati, S.; Fu, L.; Johnston, M. B.; Tan, H. H. and Jagadish, C. 'Single n^+-i-n^+ InP nanowires for highly sensitive terahertz detection'. *Nanotechnology*, 12 2017, **28**.

[60] Peng, K.; Morgan, N. P.; Wagner, F. M.; Siday, T.; Xia, C. Q.; Dede, D.; Boureau, V.; Piazza, V.; Morral, A. F. i and Johnston, M. B. 'Direct and integrating sampling in terahertz receivers from wafer-scalable InAs nanowires'. *Nat. Commun.*, 1 2024, **15**.

[61] Joyce, H. J.; Gao, Q.; Tan, H. H.; Jagadish, C.; Kim, Y.; Zou, J.; Smith, L. M.; Jackson, H. E.; Yarrison-Rice, J. M.; Parkinson, P. and Johnston, M. B. 'III–V semiconductor nanowires for optoelectronic device applications'. *Prog. Quantum Electron.*, 2-3 2011, **35**, 23–75.

[62] Joyce, H. J.; Docherty, C. J.; Gao, Q.; Tan, H. H.; Jagadish, C.; Lloyd-Hughes, J.; Herz, L. M. and Johnston, M. B. 'Electronic properties of GaAs, InAs and InP nanowires studied by terahertz spectroscopy'. *Nanotechnology*, 21 2013, **24**.

[63] Johnston, M. B. and Joyce, H. J. 'Polarization anisotropy in nanowires: Fundamental concepts and progress towards terahertz-band polarization devices'. *Prog. Quantum Electron.*, 2022, **85**.

[64] Peng, K.; Jevtics, D.; Zhang, F.; Sterzl, S.; Damry, D. A.; Rothmann, M. U.; Guilhabert, B.; Strain, M. J.; Tan, H. H.; Herz, L. M.; Fu, L.; Dawson, M. D.; Hurtado, A.; Jagadish, C. and Johnston, M. B. 'Three-dimensional cross-nanowire networks recover full terahertz state'. *Science*, 2020, **368**, 510–513.

[65] Castro-Camus, E.; Fu, L.; Lloyd-Hughes, J.; Tan, H. H.; Jagadish, C. and Johnston, M. B. 'Photoconductive response correction for detectors of terahertz radiation'. *J. Appl. Phys.*, 5 2008, **104**.

[66] Wu, Q. and Zhang, X. C. 'Free-space electro-optic sampling of terahertz beams'. *Appl. Phys. Lett.*, 1995, **67**, 3523.

[67] Tomasino, A.; Parisi, A.; Stivala, S.; Livreri, P.; Cino, A. C.; Busacca, A. C.; Peccianti, M. and Morandotti, R. 'Wideband THz time domain spectroscopy based on optical rectification and electro-optic sampling'. *Sci. Rep.*, 2013, **3**.

[68] Sanjuan, F.; Gaborit, G. and Coutaz, J.-L. 'Full electro-optic terahertz time-domain spectrometer for polarimetric studies'. *Appl. Opt.*, 21 2018, **57**, 6055.

[69] Valk, N. C. J. V. D.; Marel, W. A. M. V. D. and Planken, P. C. M. 'Terahertz polarization imaging'. *Opt. Lett.*, 20 2005, **30**, 2802.

[70] Kittel, C. *Introduction to Solid State Physics*. Wiley, 2005.

[71] Davies, C. L.; Patel, J. B.; Xia, C. Q.; Herz, L. M. and Johnston, M. B. 'Temperature-dependent refractive index of quartz at terahertz frequencies'. *J. Infrared Millim. Terahertz Waves*, 12 2018, **39**, 1236–1248.

[72] Nienhuys, H.-K. and Sundström, V. 'Intrinsic complications in the analysis of optical-pump, terahertz probe experiments'. *Phys. Rev. B*, 2005, **71**.

[73] Kužel, P. and Němec, H. 'Terahertz spectroscopy of nanomaterials: a close look at charge-carrier transport'. *Adv. Opt. Mater.*, 3 2020, **8**.

[74] Boland, J. L.; Casadei, A.; Tütüncüoglu, G.; Matteini, F.; Davies, C. L.; Jabeen, F.; Joyce, H. J.; Herz, L. M.; Morral, A. F. i and Johnston, M. B. 'Increased photoconductivity lifetime in GaAs nanowires by controlled n-type and p-type doping'. *ACS Nano*, 4 2016, **10**, 4219–4227.

[75] Boland, J. L.; Amaduzzi, F.; Sterzl, S.; Potts, H.; Herz, L. M.; Fontcuberta, A.; Morral, I and Johnston, M. B. 'High electron mobility and insights into temperature-dependent scattering mechanisms in InAsSb nanowires'. *Nano Lett.*, 2018, **18**.

[76] Garnett, J. M. 'VII. Colours in metal glasses, in metallic films, and in metallic solutions.—II'. *Philosophical Transactions of the Royal Society of London. Series A, Containing Papers of a Mathematical or Physical Character*, 1906, **205**, 237–288.

[77] Bruggeman, D. 'Berechnung verschiedener physikalischer Konstanten von heterogenen Substanzen. II. Dielektrizitätskonstanten und Leitfähigkeiten von Vielkristallen der nichtregulären Systeme'. *Annalen der Physik*, 1936, **417**, 645–672.

[78] Wagner, F. M.; Haggren, T.; Bürger, J.-C.; Keat, T. J.; Peng, K.; Uswachoke, C.; Damry, D. A.; Kraus, H.; Joyce, H. J.; Tan, H. H.; Jagadish, C.; Siday, T. and Johnston, M. B. 'The influence of subwavelength geometry on extracting the electrical properties of semiconductors by terahertz spectroscopy'. *APL Photonics*, 2025, **10**.

[79] Duvillaret, L.; Garet, F. and Coutaz, J. L. 'A reliable method for extraction of material parameters in terahertz time-domain spectroscopy'. *IEEE J. Sel. Top. Quantum Electron.*, 3 1996, **2**, 739–745.

[80] Simon, S. H. *The Oxford Solid State Basics*. Oxford University Press, 2013.

[81] Nienhuys, H.-K. and Sundström, V. 'Influence of plasmons on terahertz conductivity measurements'. *Appl. Phys. Lett.*, 2005, **87**.

[82] Barnes, W. L. 'Particle plasmons: Why shape matters'. *Am. J. Phys.*, 2016, **84**.

[83] Cooke, D. G.; MacDonald, A. N.; Hryciw, A.; Wang, J.; Li, Q.; Meldrum, A. and Hegmann, F. A. 'Transient terahertz conductivity in photoexcited silicon nanocrystal films'. *Phys. Rev. B*, 19 2006, **73**.

[84] Cooke, D. G.; Meldrum, A. and Jepsen, P. U. 'Ultrabroadband terahertz conductivity of Si nanocrystal films'. *Appl. Phys. Lett.*, 21 2012, **101**.

[85] Parkinson, P.; Lloyd-Hughes, J.; Gao, Q.; Tan, H. H.; Jagadish, C.; Johnston, M. B. and Herz, L. M. 'Transient terahertz conductivity of GaAs nanowires'. *Nano Lett.*, 7 2007, **7**, 2162–2165.

[86] Parkinson, P.; Joyce, H. J.; Gao, Q.; Tan, H. H.; Zhang, X.; Zou, J.; Jagadish, C.; Herz, L. M. and Johnston, M. B. 'Carrier lifetime and mobility enhancement in nearly defect-free core-shell nanowires measured using time-resolved terahertz spectroscopy'. *Nano Lett.*, 9 2009, **9**, 3349–3353.

[87] Zhang, Q.; Haroz, E. H.; Jin, Z.; Ren, L.; Wang, X.; Arvidson, R. S.; Luttge, A. and Kono, J. 'Plasmonic nature of the terahertz conductivity peak in single-wall carbon nanotubes'. *Nano Lett.*, 2013, **13**.

[88] Baxter, J. B. and Schmuttenmaer, C. A. 'Conductivity of ZnO nanowires, nanoparticles, and thin films using time-resolved terahertz spectroscopy'. *J. Phys. Chem. B*, 50 2006, **110**, 25229–25239.

[89] Smith, N. V. 'Classical generalization of the Drude formula for the optical conductivity'. *Phys. Rev. B*, 15 2001, **64**.

[90] Cocker, T. L.; Baillie, D.; Buruma, M.; Titova, L. V.; Sydora, R. D.; Marsiglio, F. and Hegmann, F. A. 'Microscopic origin of the Drude-Smith model'. *Phys. Rev. B*, 2017, **96**.

[91] Paries, F.; Selz, F.; Santos, C. N.; Lampin, J.-F.; Koleják, P.; Lezier, G.; Troadec, D.; Tiercelin, N.; Vanwolleghem, M.; Addda, A.; Kampfrath, T.; Seifert, T. S.; Freymann, G. von and Molter, D. 'Optical damage thresholds of single-mode fiber-tip spintronic terahertz emitters'. *Opt. Express*, 14 2024, **32**, 24826.

[92] Papaioannou, E. T.; Torosyan, G.; Keller, S.; Scheuer, L.; Battiato, M.; Mag-Usara, V. K.; L'Huillier, J.; Tani, M. and Beigang, R. 'Efficient terahertz generation using Fe/Pt spintronic emitters pumped at different wavelengths'. *IEEE Trans. Magn.*, 11 2018, **54**.

[93] Burghartz, S. and Schulz, B. 'Thermophysical properties of sapphire, AlN and MgAl,O, down to 70 K'. *J. Nucl. Mater.*, 1994, **212**, 1065–1068.

[94] Özlem, D. and Durusoy, H. Z. 'Design and preparation of antireflection and reflection optical coatings'. *Turk. J. Phys.*, 2 2004, **28**.

[95] Meixuan, L.; Lianhe, D.; Lei, Z.; Boqi, W. and Jun, M. 'Design and fabrication of visible and infrared laser HR coating'. *76th International Symposium on Advanced Optical Manufacturing and Testing Technologies: Advanced Optical Manufacturing Technologies*. SPIE, 2014.

[96] Malitson, I. H. 'Interspecimen comparison of the refractive index of fused silica'. *J. Opt. Soc. Am.*, 1965, **55**.

[97] Gallais, L. and Commandré, M. 'Laser-induced damage thresholds of bulk and coating optical materials at 1030 nm, 500 fs'. *Appl. Opt.*, 4 2014, **53**, A186.

[98] Harris, D. C.; Johnson, L. F.; Cambrea, L.; Baldwin, L.; Baronowski, M.; Zelmon, D. E.; Poston, W. B.; Kunkel, J. D.; Parish, M.; Pascucci, M. R.; Gannon, J. J. and Wen, T.-C. 'Refractive index of infrared-transparent polycrystalline alumina'. *Opt. Eng.*, 7 2017, **56**, 077103.

[99] Leitenstorfer, A.; Hunsche, S.; Shah, J.; Nuss, M. C. and Knox, W. H. 'Detectors and sources for ultrabroadband electro-optic sampling: Experiment and theory'. *Appl. Phys. Lett.*, 11 1999, **74**, 1516–1518.

[100] Vugmeyster, I. D.; Whitaker, J. F. and Merlin, R. 'GaP based terahertz time-domain spectrometer optimized for the 5–8 THz range'. *Appl. Phys. Lett.*, 18 2012, **101**.

[101] Zheng, X.; McLaughlin, C. V.; Cunningham, P. and Hayden, L. M. 'Organic broadband terahertz sources and sensors'. *J. Nanoelectron. Optoe.*, 1 2007, **2**, 58–76.

[102] Bright, T. J.; Watjen, J. I.; Zhang, Z. M.; Muratore, C.; Voevodin, A. A.; Koukis, D. I.; Tanner, D. B. and Arenas, D. J. 'Infrared optical properties of amorphous and nanocrystalline Ta_2O_5 thin films'. *J. Appl. Phys.*, 8 2013, **114**.

[103] Rasekh, P.; Saliminabi, M.; Yildirim, M.; Boyd, R. W.; Ménard, J.-M. and Dolgaleva, K. 'Propagation of broadband THz pulses: effects of dispersion, diffraction and time-varying nonlinear refraction'. *Opt. Express*, 3 2020, **28**, 3237.

[104] Grischkowsky, D; Keiding, S.; Exter, M. V. and Fattinger, C. 'Far-infrared time-domain spectroscopy with terahertz beams of dielectrics and semiconductors'. *J. Opt. Soc. Am. B*, 10 1990, **7**.

[105] Strzalkowski, I.; Joshi, S. and Crowell, C. R. 'Dielectric constant and its temperature dependence for GaAs, CdTe, and ZnSe'. *Appl. Phys. Lett.*, 6 1976, **28**, 350–352.

[106] Lax, M. and Hurstein, E. 'Infrared lattice absorption in ionic and homopolar crystals*'. *Phys. Rev.*, 1955, **97**.

[107] Stolen, R. H. 'Far-infrared absorption in high resistivity GaAs'. *Appl. Phys. Lett.*, 2 1969, **15**, 74–75.

[108] Lockwood, D. J.; Yu, G. and Rowell, N. L. 'Optical phonon frequencies and damping in AlAs, GaP, GaAs, InP, InAs and InSb studied by oblique incidence infrared spectroscopy'. *Solid State Commun.*, 7 2005, **136**, 404–409.

[109] Blakemore, J. S. 'Semiconducting and other major properties of gallium arsenide'. *J. Appl. Phys.*, 10 1982, **53**.

[110] Beard, M. C.; Turner, G. M. and Schmuttenmaer, C. A. 'Transient photoconductivity in GaAs as measured by time-resolved terahertz spectroscopy'. *Phys. Rev. B*, 23 2000, **62**, 15764–15777.

[111] Boland, J. L.; Tütüncüoglu, G.; Gong, J. Q.; Conesa-Boj, S.; Davies, C. L.; Herz, L. M.; Morral, A. F. and Johnston, M. B. 'Towards higher electron mobility in modulation doped GaAs/AlGaAs core shell nanowires'. *Nanoscale*, 23 2017, **9**, 7839–7846.

[112] Ponseca, C. S.; Němec, H.; Wallentin, J.; Anttu, N.; Beech, J. P.; Iqbal, A.; Borgström, M.; Pistol, M. E.; Samuelson, L. and Yartsev, A. 'Bulk-like transverse electron mobility in an array of heavily n -doped InP nanowires probed by terahertz spectroscopy'. *Phys. Rev. B*, 8 2014, **90**.

[113] Gu, J.; Singh, R.; Liu, X.; Zhang, X.; Ma, Y.; Zhang, S.; Maier, S. A.; Tian, Z.; Azad, A. K.; Chen, H. T.; Taylor, A. J.; Han, J. and Zhang, W. 'Active control of electromagnetically induced transparency analogue in terahertz metamaterials'. *Nat. Commun.*, 2012, **3**.

[114] Shaltout, A. M.; Shalaev, V. M. and Brongersma, M. L. 'Spatiotemporal light control with active metasurfaces'. *Science*, 2019, **364**.

[115] Shcherbakov, M. R.; Liu, S.; Zubyuk, V. V.; Vaskin, A.; Vabishchevich, P. P.; Keeler, G.; Pertsch, T.; Dolgova, T. V.; Staude, I.; Brener, I. and Fedyanin, A. A. 'Ultrafast all-optical tuning of direct-gap semiconductor metasurfaces'. *Nat. Commun.*, 1 2017, **8**.

[116] Padilla, W. J.; Taylor, A. J.; Highstrete, C.; Lee, M. and Averitt, R. D. 'Dynamical electric and magnetic metamaterial response at terahertz frequencies'. *Phys. Rev. Lett.*, 2006, **96**.

[117] Fakharuddin, A.; Gangishetty, M. K.; Abdi-Jalebi, M.; Chin, S. H.; Mohd Yusoff, A. R. bin; Congreve, D. N.; Tress, W.; Deschler, F.; Vasilopoulou, M. and Bolink, H. J. 'Perovskite light-emitting diodes'. *Nat. Electron.*, 4 2022, **5**, 203–216.

[118] Johnston, M. B. and Herz, L. M. 'Hybrid perovskites for photovoltaics: charge-carrier recombination, diffusion, and radiative efficiencies'. *Acc. Chem. Res.*, 1 2016, **49**, 146–154.

[119] Kim, H. D.; Ohkita, H.; Benten, H. and Ito, S. 'Photovoltaic performance of perovskite solar cells with different grain sizes'. *Adv. Mater.*, 5 2016, **28**, 917–922.

[120] Green, R. *Hall effect measurements in materials characterization*. Tech. rep. Keithley Instruments Inc., 2011.

[121] Popovic, R. S. 'Hall-effect devices'. *Sensors and Actuators*, 1989, **17**.

[122] Storm, K.; Halvardsson, F.; Heurlin, M.; Lindgren, D.; Gustafsson, A.; Wu, P. M.; Monemar, B. and Samuelson, L. 'Spatially resolved Hall effect measurement in a single semiconductor nanowire'. *Nat. Nanotechnol.*, 11 2012, **7**, 718–722.

[123] Braslau, N. 'Contact and metallization problems in GaAs integrated circuits'. *J. Vac. Sci. Technol. A*, 6 1986, **4**, 3085–3090.

[124] Lee, H. S.; Cole, M. W.; Lareau, R. T.; Schauer, S. N.; Fox, D. C.; Eckart, D. W.; Moerkirk, R. P.; Chang, W. H.; Jones, K. A.; Elagoz, S; Vavra, W and Clarke, R. 'The microstructure and electrical properties of nonalloyed epitaxial Au-Ge ohmic contacts to n-GaAs'. *J. Appl. Phys.*, 1992, **72**.

[125] Dayeh, S. A.; Soci, C.; Yu, P. K. L.; Yu, E. T. and Wang, D. 'Transport properties of InAs nanowire field effect transistors: The effects of surface states'. *J. Vac. Sci. Technol. B*, 4 2007, **25**, 1432–1436.

[126] Baig, N.; Kammakakam, I.; Falath, W. and Kammakakam, I. 'Nanomaterials: A review of synthesis methods, properties, recent progress, and challenges'. *Mater. Adv.*, 6 2021, **2**, 1821–1871.

[127] Turner, G. M.; Beard, M. C. and Schmuttenmaer, C. A. 'Carrier localization and cooling in dye-sensitized nanocrystalline titanium dioxide'. *J. Phys. Chem. B*, 45 2002, **106**, 11716–11719.

[128] Beard, M. C.; Turner, G. M.; Murphy, J. E.; Micic, O. I.; Hanna, M. C.; Nozik, A. J. and Schmuttenmaer, C. A. 'Electronic coupling in InP nanoparticle arrays'. *Nano Lett.*, 12 2003, **3**, 1695–1699.

[129] Pushkarev, V.; Němec, H.; Paingad, V. C.; Maňák, J.; Jurka, V.; Novák, V.; Ostatnický, T. and Kužel, P. 'Charge transport in single-crystalline GaAs nanobars: impact of band bending revealed by terahertz spectroscopy'. *Adv. Funct. Mater.*, 5 2022, **32**.

[130] Exter, M. V. and Grischkowsky, D. 'Optical and electronic properties of doped silicon from 0.1 to 2 THz'. *Appl. Phys. Lett.*, 17 1990, **56**, 1694–1696.

[131] Kužel, P. and Němec, H. 'Terahertz conductivity in nanoscaled systems: Effective medium theory aspects'. *J. Phys. D: Appl. Phys.*, 37 2014, **47**.

[132] Koblmüller, G. and Abstreiter, G. 'Growth and properties of InGaAs nanowires on silicon'. *Phys. Status Solidi - Rapid Res. Lett.*, 1 2014, **8**, 11–30.

[133] Yi, S. S.; Girolami, G.; Amano, J.; Islam, M. S.; Sharma, S.; Kamins, T. I. and Kimukin, I. 'InP nanobridges epitaxially formed between two vertical Si surfaces by metal-catalyzed chemical vapor deposition'. *Appl. Phys. Lett.*, 13 2006, **89**.

[134] Dayeh, S. A.; Aplin, D. P.; Zhou, X.; Yu, P. K.; Yu, E. T. and Wang, D. 'High electron mobility InAs nanowire field-effect transistors'. *Small*, 2 2007, **3**, 326–332.

[135] Tomioka, K.; Motohisa, J.; Hara, S.; Hiruma, K. and Fukui, T. 'GaAs/AlGaAs core multishell nanowire-based light-emitting diodes on Si'. *Nano Lett.*, 5 2010, **10**, 1639–1644.

[136] Wallentin, J.; Anttu, N.; Asoli, D.; Huffman, M.; Aberg, I.; Magnusson, M. H.; Siefer, G.; Fuss-Kailuweit, P.; Dimroth, F.; Witzigmann, B.; Xu, H. Q.; Samuelson, L.; Deppert, K. and Borgstrom, M. T. 'InP nanowire array solar cells achieving 13.8% efficiency by exceeding the ray optics limit'. *Science*, 6123 2013, **339**, 1054–1057.

[137] Ramgir, N. S.; Yang, Y. and Zacharias, M. 'Nanowire-based sensors'. *Small*, 16 2010, **6**, 1705–1722.

[138] Azimi, Z.; Gopakumar, A.; Ameruddin, A. S.; Li, L.; Truong, T.; Nguyen, H. T.; Tan, H. H.; Jagadish, C. and Wong-Leung, J. 'Tuning the crystal structure and optical properties of selective area grown InGaAs nanowires'. *Nano Res.*, 4 2022, **15**, 3695–3703.

[139] Mikkelsen, A. and Lundgren, E. 'Surface science of free standing semiconductor nanowires'. *Surf. Sci.*, 2013, **607**, 97–105.

[140] Mattila, M.; Hakkarainen, T.; Mulot, M. and Lipsanen, H. 'Crystal-structure-dependent photoluminescence from InP nanowires'. *Nanotechnology*, 6 2006, **17**, 1580–1583.

[141] Joyce, H. J.; Wong-Leung, J.; Gao, Q.; Tan, H. H. and Jagadish, C. 'Phase perfection in zinc blende and wurtzite III- V nanowires using basic growth parameters'. *Nano Lett.*, 3 2010, **10**, 908–915.

[142] Hobbs, R. G.; Petkov, N. and Holmes, J. D. 'Semiconductor nanowire fabrication by bottom-up and top-down paradigms'. *Chem. Mater.*, 11 2012, **24**, 1975–1991.

[143] Lu, W. and Lieber, C. M. 'Nanoelectronics from the bottom up'. *Nat. Mater.*, 2007, **6**.

[144] Wagner, R. S. and Ellis, W. C. 'Vapor-liquid-solid mechanism of single crystal growth'. *Appl. Phys. Lett.*, 5 1964, **4**, 89–90.

[145] Wu, Y. and Yang, P. 'Direct observation of vapor-liquid-solid nanowire growth'. *J. Am. Chem. Soc.*, 13 2001, **123**, 3165–3166.

[146] Samuelson, L.; Thelander, C.; Björk, M. T.; Borgström, M.; Deppert, K.; Dick, K. A.; Hansen, A. E.; Mårtensson, T.; Panev, N.; Persson, A. I.; Seifert, W.; Skold, N.; Larsson, M. W. and Wallenberg, L. R. 'Semiconductor nanowires for 0D and 1D physics and applications'. *Phys. E: Low-Dimens. Syst. Nanostruct.*, 2-3 SPEC.ISS. 2004, **25**, 313–318.

[147] Agarwal, R. and Lieber, C. M. 'Semiconductor nanowires: Optics and optoelectronics'. *Appl. Phys. A: Mater. Sci.Process.*, 3 2006, **85**, 209–215.

[148] Gudiksen, M. S.; Wang, J. and Lieber, C. M. 'Size-dependent photoluminescence from single indium phosphide nanowires'. *J. Phys. Chem. B*, 16 2002, **106**, 4036–4039.

[149] Jiang, N.; Parkinson, P.; Gao, Q.; Breuer, S.; Tan, H. H.; Wong-Leung, J. and Jagadish, C. 'Long minority carrier lifetime in Au-catalyzed GaAs/Al xGa 1-xAs core-shell nanowires'. *Appl. Phys. Lett.*, 2 2012, **101**.

[150] Jiang, N.; Gao, Q.; Parkinson, P.; Wong-Leung, J.; Mokkapati, S.; Breuer, S.; Tan, H. H.; Zheng, C. L.; Etheridge, J. and Jagadish, C. 'Enhanced minority carrier lifetimes in GaAs/AlGaAs core-shell nanowires through shell growth optimization'. *Nano Lett.*, 11 2013, **13**, 5135–5140.

[151] Joyce, H. J.; Parkinson, P.; Jiang, N.; Docherty, C. J.; Gao, Q.; Tan, H. H.; Jagadish, C.; Herz, L. M. and Johnston, M. B. 'Electron mobilities approaching bulk limits in "surface-free" GaAs nanowires'. *Nano Lett.*, 10 2014, **14**, 5989–5994.

[152] Baig, S. A.; Boland, J. L.; Damry, D. A.; Tan, H. H.; Jagadish, C.; Joyce, H. J. and Johnston, M. B. 'An ultrafast switchable terahertz polarization modulator based on III–V semiconductor nanowires'. *Nano Lett.*, 4 2017, **17**, 2603–2610.

[153] Joyce, H. J.; Baig, S. A.; Parkinson, P.; Davies, C. L.; Boland, J. L.; Tan, H. H.; Jagadish, C.; Herz, L. M. and Johnston, M. B. 'The influence of surfaces on the transient terahertz conductivity and electron mobility of GaAs nanowires'. *J. Phys. D: Appl. Phys.*, 22 2017, **50**.

[154] Boland, J. L.; Conesa-Boj, S.; Parkinson, P.; Tütüncüoglu, G.; Matteini, F.; Rüffer, D.; Casadei, A.; Amaduzzi, F.; Jabeen, F.; Davies, C. L.; Joyce, H. J.; Herz, L. M.; Morral, A. F. I. and Johnston, M. B. 'Modulation doping of GaAs/AlGaAs core-shell nanowires with effective defect passivation and high electron mobility'. *Nano Lett.*, 2 2015, **15**, 1336–1342.

[155] Balaghi, L.; Shan, S.; Fotev, I.; Moebus, F.; Rana, R.; Venanzi, T.; Hübner, R.; Mikolajick, T.; Schneider, H.; Helm, M.; Pashkin, A. and Dimakis, E. 'High electron mobility in strained GaAs nanowires'. *Nat. Commun.*, 1 2021, **12**.

[156] Schindelin, J.; Arganda-Carreras, I.; Frise, E.; Kaynig, V.; Longair, M.; Pietzsch, T.; Preibisch, S.; Rueden, C.; Saalfeld, S.; Schmid, B.; Tinevez, J.-Y.; White, D. J.; Hartenstein, V.; Eliceiri, K.; Tomancak, P. and Cardona, A. 'Fiji: an open-source platform for biological-image analysis'. *Nat. Methods*, 2012, **9**, 676–682.

[157] Chou, L. W.; Shin, N.; Sivaram, S. V. and Filler, M. A. 'Tunable mid-infrared localized surface plasmon resonances in silicon nanowires'. *J. Am. Chem. Soc.*, 39 2012, **134**, 16155–16158.

[158] Madelung, O., ed. *Semiconductors – Basic Data*. Springer, 1996.

[159] Imoto, N.; Kawana, A.; Machida, S. and Tsuchiya, H. 'Characteristics of dispersion free single-mode fiber in the 1.5um wavelength region'. *IEEE J. Quantum Electron.*, 1980, **10**.

[160] Eng, P. C.; Song, S. and Ping, B. 'State-of-the-art photodetectors for optoelectronic integration at telecommunication wavelength'. *Nanophotonics*, 1 2015, **4**, 277–302.

[161] Liu, H.; Wang, J.; Guo, D.; Shen, K.; Chen, B. and Wu, J. 'Design and fabrication of high performance InGaAs near infrared photodetector'. *Nanomaterials*, 21 2023, **13**.

[162] Birch, M.; Soon, J.; Travouillon, T.; Mendel, T.; Taylor, B. and Tiong, B. C. K. 'InGaAs focal plane array for transient astronomy in the NIR'. *J. Astron. Telesc. Instrum. Syst.*, 01 2022, **8**.

[163] Ajayan, J. and Nirmal, D. 'A review of InP/InAlAs/InGaAs based transistors for high frequency applications'. *Superlattices Microstruct.*, 2015, **86**, 1–19.

[164] Yu, C.; Xu, Q. and Zhang, J. 'Recent advances in InGaAs/InP single-photon detectors'. *Meas. Sci. Technol.*, 12 2024, **35**.

[165] Abraham, P; Monteil, Y; Sacilotti, M; Benyattou, T; Garcia, M. A.; Moneger, S; Tabata, A; Landers, R; Morais, J and Pitaval, M. 'Optical studies of InP/InAlAs/InP interface recombinations'. *Appl. Surf. Sci.*, 1993, **65**, 777–783.

[166] Hooper, I. R.; Grant, N. E.; Barr, L. E.; Hornett, S. M.; Murphy, J. D. and Hendry, E. 'High efficiency photomodulators for millimeter wave and THz radiation'. *Sci. Rep.*, 1 2019, **9**.

[167] Hooper, I. R.; Khorani, E.; Romain, X.; Barr, L. E.; Niewelt, T.; Saxena, S.; Wratten, A.; Grant, N. E.; Murphy, J. D. and Hendry, E. 'Engineering the carrier lifetime and switching speed in Si-based mm-wave photomodulators'. *J. Appl. Phys.*, 23 2022, **132**.

[168] Zhang, J.; Itzler, M. A.; Zbinden, H. and Pan, J. W. 'Advances in InGaAs/InP single-photon detector systems for quantum communication'. *Light: Sci. Appl.*, 2015, **4**.

[169] Massicotte, M; Schmidt, P; Vialla, F; Schädler, K. G.; Reserbat-Plantey, A; Watanabe, K; Taniguchi, T; Tielrooij, K. J. and Koppens, F. H. L. 'Picosecond photoresponse in van der Waals heterostructures'. *Nat. Nanotechnol.*, 2016, **11**.

[170] Horvath, R; Roux, J.-F.; Coutaz, J.-L.; Poette, J.; Cabon, B and Graham, C. 'Ultrafast InGaAs photoswitch for RF signal processing'. *IEEE International Conference on Optical Network Design and Modeling*. 2017.

[171] Bacon, D. R.; Madéo, J. and Dani, K. M. 'Photoconductive emitters for pulsed terahertz generation'. *J. Opt.*, 6 2021, **23**.

[172] Adachi, S. 'Physical Properties of III–V Semiconductor Compounds: InP, InAs, GaAs, GaP, InGaAs, and InGaAsP'. New York: John Wiley & Sons, 1992, 86–96.

[173] Liu, Y.; Jin, X.; Jung, H.; Lee, S.; Harun, F.; Ng, J. S.; Krishna, S. and David, J. P. 'Electroabsorption in InGaAs and GaAsSb p-i-n photodiodes'. *Appl. Phys. Lett.*, 22 2024, **125**.

[174] Pearsall, T. P. and Hirtz, J. P. 'The carrier mobilities in $Ga_{0.47}In_{0.53}As$ grown by organo-metallic CVD and liquid-phase epitaxy'. *J. Cryst. Growth*, 1981, **54**, 127–131.

[175] Gupta, S; Whitaker, J. F.; Williamson, S. L.; Mourou, G. A.; Lester, L; Hwang, K. C.; Ho, P; Mazurowski, J and Ballingall, J. M. 'High-speed photodetector applications of GaAs and $In_xGa_{1-x}As$/GaAs grown by low-temperature molecular beam epitaxy'. *J. Electron. Mater.*, 12 1993, **22**.

[176] Mangeney, J; Joulaud, L; Decobert, J; Lourtioz, J.-M.; Perrossier, J.; Cabaret, S and Crozat, P. 'Electrical properties of 1.55 μm sensitive ion-irradiated InGaAs with subpicosecond carrier lifetime'. *Electron. Lett.*, 2003, **39**, 681–682.

[177] Ospald, F.; Maryenko, D.; Klitzing, K. V.; Driscoll, D. C.; Hanson, M. P.; Lu, H.; Gossard, A. C. and Smet, J. H. '1.55 µm ultrafast photoconductive switches based on ErAs:InGaAs'. *Appl. Phys. Lett.*, 13 2008, **92**.

[178] Driscoll, D. C.; Hanson, M. P.; Gossard, A. C. and Brown, E. R. 'Ultrafast photoresponse at 1.55 µm in InGaAs with embedded semimetallic ErAs nanoparticles'. *Appl. Phys. Lett.*, 5 2005, **86**, 1–3.

[179] Shockley, W and Read, W. T. J. 'Statistics of the recombinations of holes and electrons'. *Phys. Rev.*, 1952, **87**.

[180] Gupta, S.; Whitaker, J. F. and Mourou, G. A. 'Ultrafast carrier dynamics in III–V semiconductors grown by molecular-beam epitaxy at very low substrate temperatures'. *IEEE J. Quantum Electron.*, 1992, **28**.

[181] Melloch, M. R.; Woodall, J. M.; Harmon, E. S.; Otsuka, N; Pollak, F. H.; Nolte, D. D.; Feenstra, R. M. and Lutz, M. A. 'Low-temperature grown III–V materials'. *Annu. Rev. Mater. Sci.*, 1995, **25**.

[182] Smith, F. W.; Calawa, A. R.; Chen, C.-L.; Manfra, M. J. and Mahoney, L. J. 'New MBE buffer used to eliminate backgating in GaAs MESFET's'. *IEEE Electron Device Lett.*, 2 1988, **9**, 77.

[183] Künzel, H.; Böttcher, J.; Gibis, R. and Urmann, G. 'Material properties of $Ga_{0.47}In_{0.53}As$ grown on InP by low-temperature molecular beam epitaxy'. *Appl. Phys. Lett.*, 11 1992, **61**, 1347–1349.

[184] Globisch, B.; Dietz, R. J.; Nellen, S.; Göbel, T. and Schell, M. 'Terahertz detectors from Be-doped low-temperature grown InGaAs/InAlAs: Interplay of annealing and terahertz performance'. *AIP Advances*, 12 2016, **6**.

[185] Tousley, B. C.; Mehta, S. M.; Lobad, A. I.; Rodney, P. J.; Fauchet, P. M. and Cooke, P. 'Femtosecond optical response of low temperature grown $In_{0.53}Ga_{0.47}As$'. *J. Electron. Mater.*, 12 1993, **22**.

[186] B., S. 'All-fiber terahertz time-domain spectrometer at 1.5um'. *Opt. Express*, 2008, **16**, 337.

[187] Metzger, R. A.; Brown, A. S.; McCray, L. G. and Henige, J. A. 'Structural and electrical properties of low temperature GaInAs'. *J. Vac. Sci. Technol. B*, 3 1993, **11**, 798–801.

[188] Grandidier, B.; Chen, H.; Feenstra, R. M.; McInturtf, D. T.; Juodawlkis, P. W. and Ralph, S. E. 'Scanning tunneling microscopy and spectroscopy of arsenic antisites in low temperature grown InGaAs'. *Appl. Phys. Lett.*, 10 1999, **74**, 1439–1441.

[189] Kuenzel, H; Biermann, K; Nickel, D and Elsaesser, T. 'Low-temperature MBE growth and characteristics of InP-based AlInAs/GaInAs MQW structures'. *J. Cryst. Growth*, 2001, **227**, 284–288.

[190] Takazato, A.; Kamakura, M.; Matsui, T.; Kitagawa, J. and Kadoya, Y. 'Detection of terahertz waves using low-temperature-grown InGaAs with 1.56 µm pulse excitation'. *Appl. Phys. Lett.*, 10 2007, **90**.

[191] Takahashi, R.; Kawamura, Y. and Iwamura, H. 'Ultrafast 1.55 µm all-optical switching using low-temperature-grown multiple quantum wells'. *Appl. Phys. Lett.*, 2 1996, **68**, 153–155.

[192] Globisch, B.; Dietz, R. J.; Stanze, D.; Göbel, T. and Schell, M. 'Carrier dynamics in Beryllium doped low-temperature-grown InGaAs/InAlAs'. *Appl. Phys. Lett.*, 17 2014, **104**.

[193] Dietz, R. J. B.; Gerhard, M.; Stanze, D.; Koch, M.; Sartorius, B.; Schell, M.; Ketchen, M. B.; Grischkowsky, D; Chen, T. C.; Chi, C.-C; Duling, I. N.; Halas, N. J.; Halbout, J.-M; Kash, J. A. and Li, G. P. 'THz generation at 1.55 µm excitation: six-fold increase in THz conversion efficiency by separated photoconductive and trapping regions'. *Opt. Express*, 1 2011, **5**, 124–166.

[194] Ponomarev, D. S.; Khabibullin, R. A.; Klochkov, A. N.; Yachmenev, A. E.; Bugaev, A. S.; Khusyainov, D. I.; Buriakov, A. M.; Bilyk, V. P. and Mishina, E. D. 'Ultrafast dynamics of photoexcited charge carriers in $In_{0.53}Ga_{0.47}As/In_{0.52}Al_{0.48}As$ superlattices under femtosecond laser excitation'. *Semiconductors*, 7 2018, **52**, 864–869.

[195] Ponomarev, D. S.; Gorodetsky, A.; Yachmenev, A. E.; Pushkarev, S. S.; Khabibullin, R. A.; Grekhov, M. M.; Zaytsev, K. I.; Khusyainov, D. I.; Buryakov, A. M. and Mishina, E. D. 'Enhanced terahertz emission from strain-induced InGaAs/InAlAs superlattices'. *J. Appl. Phys.*, 15 2019, **125**.

[196] Dietz, R. J.; Globisch, B.; Gerhard, M.; Velauthapillai, A.; Stanze, D.; Roehle, H.; Koch, M.; Göbel, T. and Schell, M. '64 µw pulsed terahertz emission from growth optimized InGaAs/InAlAs heterostructures with separated photoconductive and trapping regions'. *Appl. Phys. Lett.*, 6 2013, **103**.

[197] Roehle, H; Dietz, R. J. B.; Hensel, H. J.; Böttcher, J; Künzel, H; Stanze, D; Schell, M and Sartorius, B. 'Next generation 1.5 µm terahertz antennas: mesa-structuring of InGaAs/InAlAs photoconductive layers'. *Opt. Express*, 2010, **18**.

[198] Clawson, A. R.; Mullin, D. P.; Elder, D. I. and Wieder, H.-I. 'Semi-insulating $In_{0.53}Ga_{0.47}As$ by Fe doping'. *J. Cryst. Growth*, 1 1983, **64**.

[199] Tell, B.; Koren, U. and Miller, B. I. 'Metalorganic vapor-phase-epitaxial growth of Fe-doped $In_{0.53}Ga_{0.47}As$'. *J. Appl. Phys.*, 3 1987, **61**, 1172–1175.

[200] Guillot, G; Bremond, G; Benyattou, T; Ducroquet, F; Wirth, B; Colombet, M; Louati, A and Bencherifa, A. 'Identification of the Fe acceptor level in $Ga_{0.47}In_{0.53}As$'. *Semicond. Sci. Technol.*, 1990, **5**, 391–394.

[201] Srocka, B; Schener, H and Bimberg, D. 'Fe^{2+}-Fe^{3+} level as a recombination center in $In_{0.53}Ga_{0.47}As$'. *Phys. Rev. B*, 1994, **49**.

[202] Carmody, C.; Tan, H. H.; Jagadish, C.; Gaarder, A. and Marcinkevičius, S. 'Ion-implanted $In_{0.53}Ga_{0.47}As$ for ultrafast optoelectronic applications'. *Appl. Phys. Lett.*, 22 2003, **82**, 3913–3915.

[203] Suzuki, M. and Tonouchi, M. 'Fe-implanted InGaAs photoconductive terahertz detectors triggered by 1.56 µm femtosecond optical pulses'. *Appl. Phys. Lett.*, 16 2005, **86**, 1–3.

[204] Kohlhaas, R. B.; Globisch, B.; Nellen, S.; Liebermeister, L.; Schell, M.; Richter, P.; Koch, M.; Semtsiv, M. P. and Masselink, W. T. 'Rhodium doped InGaAs: A superior ultrafast photoconductor'. *Appl. Phys. Lett.*, 10 2018, **112**.

[205] Kohlhaas, R. B.; Breuer, S.; Nellen, S.; Liebermeister, L.; Schell, M.; Semtsiv, M. P.; Masselink, W. T. and Globisch, B. 'Photoconductive terahertz detectors with 105 dB peak dynamic range made of rhodium doped InGaAs'. *Appl. Phys. Lett.*, 22 2019, **114**.

[206] Kotera, N; Arimoto, H; Miura, N; Shibata, K; Ueki, Y; Tanaka, K; Nakamura, H; Mishima, T; Aiki, K and Washima, M. 'Electron effective mass and nonparabolicity in InGaAs/InAlAs quantum wells lattice-matched to InP'. *Physica E*, 2001, **11**, 219–223.

[207] Riffe, D. M. 'Temperature dependence of silicon carrier effective masses with application to femtosecond reflectivity measurements'. *J. Opt. Soc. Am. B*, 2002, **19**.

[208] Whalley, L. D.; Frost, J. M.; Morgan, B. J. and Walsh, A. 'Impact of non-parabolic electronic band structure on the optical and transport properties of photovoltaic materials'. *Phys. Rev. B*, 2019, **99**.

[209] Sun, Y.; Thompson, S. E. and Nishida, T. 'Physics of strain effects in semiconductors and metal-oxide-semiconductor field-effect transistors'. *J. Appl. Phys.*, 10 2007, **101**.

[210] Chu, M.; Sun, Y.; Aghoram, U. and Thompson, S. E. 'Strain: A solution for higher carrier mobility in nanoscale mosfets'. *Annu. Rev. Mater. Res.*, 2009, **39**, 203–229.

[211] Steppke, A.; Zhao, L.; Barber, M. E.; Scaffidi, T.; Jerzembeck, F.; Rosner, H.; Gibbs, A. S.; Maeno, Y.; Simon, S. H.; Mackenzie, A. P. and Hicks, C. W. 'Strong peak in T_c of Sr_2RuO_4 under uniaxial pressure'. *Science*, 2017, **355**.

[212] Pilon, F. T. A.; Lyasota, A.; Niquet, Y. M.; Reboud, V.; Calvo, V.; Pauc, N.; Widiez, J.; Bonzon, C.; Hartmann, J. M.; Chelnokov, A.; Faist, J. and Sigg, H. 'Lasing in strained germanium microbridges'. *Nat. Commun.*, 1 2019, **10**.

[213] Kuo, C. P.; Vong, S. K.; Cohen, R. M. and Stringfellow, G. B. 'Effect of mismatch strain on band gap in III–V semiconductors'. *J. Appl. Phys.*, 12 1985, **57**, 5428–5432.

[214] Shi, J.; Wichmann, N.; Roelens, Y. and Bollaert, S. 'Electrical characterization of $In_{0.53}Ga_{0.47}As/In_{0.52}Al_{0.48}As$ high electron mobility transistors on plastic flexible substrate under mechanical bending conditions'. *Appl. Phys. Lett.*, 24 2013, **102**.

[215] Phoenix Technologies International LLC. *Polyethylene Terephthalate: Key Properties*. Accessed: 2025-09-10. Available at: https://www.phoenixtechnologies.net/media/371/PET%20Properties%202008.pdf.

[216] Ioffe Institute. *Mechanical properties, elastic constants, lattice vibrations of Gallium Indium Arsenide (GaInAs)*. Accessed: 2025-09-10. Available at: https://www.ioffe.ru/SVA/NSM/Semicond/GaInAs/mechanic.html.

[217] Ugural, A. C. and Fenster, S. K. 'Bending of Beams'. *Advanced Mechanics of Materials and Applied Elasticity*. 6th ed. Pearson, 2020. Chap. 5, 242–314.

[218] Cullity, B. D. and Stock, S. R. 'Elements of X-Ray Diffraction'. *Elements of X-Ray Diffraction*. 3rd ed. Harlow, UK: Pearson Education Limited, 2014. Chap. 4, 125–170.

[219] Vurgaftman, I.; Meyer, J. R. and Ram-Mohan, L. R. 'Band parameters for III–V compound semiconductors and their alloys'. *J. Appl. Phys.*, 11 2001, **89**, 5815–5875.

[220] Haussühl, S. *Physical Properties of Crystals: An Introduction*. Wiley-VCH, 2007.

[221] Stetsiv, Y. A.; Yatsyshyn, M. M.; Nykypanchuk, D.; Korniy, S. A.; Saldan, I.; Reshetnyak, O. V. and Bednarchuk, T. J. 'Characterization of polyaniline thin films prepared on polyethylene terephthalate substrate'. *Polym. Bull.*, 11 2021, **78**, 6251–6265.

[222] Kuruppu, M. D. and Chong, K. P. 'Fracture toughness testing of brittle materials using semi-circular bend (SCB) specimen'. *Engineering Fracture Mechanics*, 2012, **91**, 133–150.

[223] Leterrier, Y; Boogh, L; Andersons, J and Månson, J.-A. 'Adhesion of silicon oxide layers on poly (ethylene terephthalate). I: Effect of substrate properties on coating's fragmentation process'. *Journal of Polymer Science Part B: Polymer Physics*, 1997, **35**, 1449–1461.

[224] Ranka, A.; Layek, M.; Kochiyama, S.; López-Pernia, C.; Chandler, A. M.; Kocoj, C. A.; Magliano, E.; Di Carlo, A.; Brunetti, F.; Guo, P. *et al.* 'Cracking in polymer substrates for flexible electronic devices and its mitigation'. *npj Flexible Electronics*, 2025, **9**, 92.

[225] Shenoy, V.; Schwartzman, A. and Freund, L. 'Crack patterns in brittle thin films'. *International journal of fracture*, 2001, **109**, 29–45.

[226] Martin, P.; Skouri, E. M.; Chusseau, L.; Alibert, C. and Bissessur, H. 'Accurate refractive index measurements of doped and undoped InP by a grating coupling technique'. *Appl. Phys. Lett.*, 1995, **67**, 881.

[227] Jin, Y.-S.; Kim, G.-J. and Jeon, S.-G. 'Terahertz dielectric properties of polymers'. *J. Korean Phys. Soc.*, 2 2006, **49**, 513–517.

[228] Kim, S. I.; Park, D. W.; Kim, H. S. and Kim, H. S. 'In-situ non-contact monitoring algorithm for PET crystallinity and moisture content using Terahertz time-domain spectroscopy'. *Polym. Test.*, 2023, **124**.